Crystal-Bound Ligands in Nanocrystal Synthesis

By

Michael Turo

Dissertation
Submitted to the Faculty of the
Graduate School of Vanderbilt University
in partial fulfillment of the requirements
for the degree of

DOCTOR OF PHILOSOPHY
in

Chemistry
May, 2017
Nashville, Tennessee

Approved:

Janet E. Macdonald, Ph.D.
Eva M. Harth, Ph.D.
Bridget R. Rogers, Ph.D.
Sandra J. Rosenthal, Ph.D.

Dedicate to

My family and friends who have always believed in me

ACKNOWLEDGEMENTS

First of all I have to thank Professor Janet Macdonald. It truly was a privilege to work in the Macdonald Lab and I am grateful for all of the support in helping me develop as a chemist and as a professional. Janet's enthusiasm and passion was and will remain an inspiration to me. I also would like to thank Dr. Eva Harth, Dr. Bridget Rogers, and Dr. Sandra Rosenthal for all of their support and guidance on my dissertation committee.

I would like to thank Dr. David Prendergast, for letting me work in his group at the Molecular Foundry for 10 months, and for all his advice and insight on the computational modeling. Additionally, my computation work in Berkeley would not have gone far without the help of Dr. Liwen (Sabrina) Wan and Sebastaain Huber, along with all the other members of the Prendergast group. Additionally, I received a lot of experimental support though out my time in graduate school, for which I am very grateful. At Vanderbilt, Dr. Don Stec with NMR, Dr. Bridget Rogers and Dr. Ben Schmidt with XPS, Dr. James McBride with TEM, and Dr. Xiao Shen with computational modeling. At the University of Toronto, Dr. Edward Sargent and Dr. Geoffrey McDowell with TGA-MS.

I have been very fortunate to work with such amazing people in the Macdonald Lab, an I have enjoyed the time I spent with all of them both in and out of lab. I want to thank Shane Finn for being with me from the start; I can't imagine what grad school would be like with him. I really appreciated all of the discussion and help from everyone and lab on my work, in particular Andrew La Croix and Alice Leach for their years of critical discussion that has enriched my project. I want to thank Evan Robinson for picking up some of my projects and doing a great job with them. I especially want to thank Dr. Emil Hernandez-Pagan, for everything he did establishing the culture of the lab and teaching me how to survive graduate school.

I would like to thank the funding sources for my work: Vanderbilt Department of Chemistry, Vanderbilt Institute of Nanoscale Science and Engineering, the NSF (NSF-1253105 and NSF EPS-1004083), the Mitchum E. Warren Fellowship, the DOE-SCGSR Award (DE-AC05-06OR23100), the Molecular Foundry, and for computational resources HPCS at LBNL and NERSC.

Finally, I would like to thank my family and friends. I have meet so many great people in Nashville both inside and outside of the chemistry department, thank you all for keeping me grounded. To my brother, Matthew, you have always been such a great role model and I am really proud of all of your accomplishments, professionally and personally, with your career development and your amazing wife, Liz. To my parents, your love and support means the world to me, I have and always will cherished everything you do for me.

TABLE OF CONTENTS

Page

DEDICATION iii

ACKNOWLEDGEMENTS iv

LIST OF TABLES viii

LIST OF FIGURES ix

Chapter

I. INTRODUCTION 1

1.1 Introduction 1
1.2 Colloidal Synthesis of Quantum Dots 4
1.2.1 Classic Nucleation Theory 5
1.2.2 La Mer Model of Burst Nucleation 6
1.3 Surface Coordination of Ligands to Quantum Dots 8
1.3.1 The Importance of Ligands 8
1.3.2 Types of Surface Coordination 8
1.4 Techniques for the Surface Characterization of Quantum Dots 12
1.4.1 Nuclear Magnetic Resonance (NMR) 12
1.4.2 X-ray Photoelectron Spectroscopy (XPS) 14
1.4.3 Thermogravametric Mass Spectrometry (TGA-MS) 16
1.5 Scope of the Thesis 17

II. IDENTIFICATION AND FUNCTIONALIZATION OF CRYSTAL-BOUND LIGANDS 19

2.1 Introduction 19
2.2 Results and Discussion 21
2.2.1 Evidence for Crystal-Bound Thiols 21
2.2.2 Water Solubility of the Copper Sulfides with Crystal-Bound Ligands 32
2.3 Conclusion 41
2.4 Experimental Methods 43

III. DUAL-MODE SURFACE PASSIVATION 51

3.1 Introduction 51
3.2 Results and Discussion 53
3.3 Conclusion 67
3.4 Experimental Methods 68

IV. COMPUTATIONAL MODELING OF THE LIGAND COORDINATION ON CORE-SHELL QUANTUM DOTS 75

4.1 Introduction 75
4.2 Results and Discussion 77
4.2.1 Surface-bound models. 77
4.2.2 XAS for Ligand Binding Determination 85
4.3 Conclusion 95

V. HIERACRHICAL NANOSTRUCTURES FROM Cu_2S NANOCRYSTALS WITH CRYSTAL-BOUND LGIANDS 97

5.1 Introduction 97
5.2 Results and Discussion 99
5.2.1 Cu_2S-Ru Hybrid Nanocrystals 99
5.2.2 Cu_2S Nanorods by Oriented Attachment 107
5.3 Conclusion 109
5.4 Future Work 110
5.5 Experimental Methods 113

VI. CONCLUSION 115

6.1 Summary of Thesis 115
6.2 Conclusion and Perspective 117

Appendix

A. ADDITIONAL SURFACE CHARATERIZATION 119

B. ADDITIONAL COMPUTATIONAL MODELS 142

REFERENCES 148

LIST OF TABLES

Table Page

3.1: Experimental and computational red shifts 63

4.1: Computational determined binding energies of ligands to CdSe/ZnS.....81

LIST OF FIGURES

Figure Page

1.1: Quantum confinement....3

1.2: Precursor conversion to nanocrystals....4

1.3: Classic nucleation theory....6

1.4: La Mer model of nucleation and growth....7

1.5: Ligand coordination to quantum dots....9

1.6: Ligand exchange on quantum dots....11

1.7: 1H NMR of dodecanethiol capped CdSe@ZnS quantum dots....14

1.8: Cu 2p XPS of Cu_2S nanocrystals....16

2.1: Crystal-bound vs. surface bound....21

2.2: Synthesis of Cu_2S nanocrystals with crystal-bound and surface-bound thiols....23

2.3: IR spectrum of ligand exchange on Cu_2S with surface-bound ligands....24

2.4: XRD of Cu_2S nanocrystals....25

2.5: Surface characterization using ^1H NMR....26

2.6: S 2p XPS of Cu_2S nanocrystals with crystal-bound and surface-bound ligands....29

2.7: TGA of Cu_2S nanocrystals with crystal-bound and surface-bound ligands....30

2.8: Mass spec of removed organics from Cu_2S nanocrystals....31

2.9: Scheme for water soluble Cu_2S nanocrystals with crystal-bound ligands....33

2.10: Characterization of water soluble Cu_2S nanocrystals with crystal-bound ligands....34

2.11: SAED of Cu_2S nanocrystals before and after hydrolysis....35

2.12: Histogram of the size of the Cu_2S before and after hydrolysis....36

2.13: XRD of CuO precipitate 38

2.14: Characterization of water soluble $CuInS_2$ nanocrystals with crystal-bound ligands 39

2.15: SAED of $CuInS_2$ nanocrystals before and after hydrolysis 40

2.16: EDS of $CuInS_2$ nanocrystals before and after hydrolysis 41

3.1: Crystal-bound DDT capped CdSe@ZnS nanocrystals 54

3.2: Crystal-bound DDT capped CdSe@ZnS nanocrystals with extra ZnS shell....55

3.3: XPS of crystal-bound CdSe@ZnS with crystal-bound and surface-bound thiols 56

3.4: Surface characterization of CdSe@ZnS with crystal-bound DDT 57

3.5: Picture showing colloidal stability of CdSe@ZnS 58

3.6: CdSe@ZnS with crystal-bound D3MP....59

3.7: IR of CdSe@ZnS with crystal-bound D3MP before and after hydrolysis 60

3.8: Change in fluorescence with changing surface passivation....61

3.9: Lattice fringing for CdSe@ZnS nanocrystals....62

3.10: Computational models of dual-mode binding 63

3.11: Photocatalytic degradation of methylene blue....66

3.12: Absorbance spectra of methylene blue degradation 67

3.13: ^{1}H NMR of crystal-bound DDT on CdSe@ZnS 73

3.14: ^{1}H NMR of surface-bound DDT on CdSe@ZnS....74

4.1: Binding of neutral ligands to a nonpolar surface 76

4.2: Structural models of surface-bound bind modes 80

4.3: Structural modes of bridging ligands....83

4.4: Calculated densities of states for different surface passivations....84

4.5: Structural models for crystal-bound ligands....86

4.6: Simulated S K-edge XAS spectrum for bulk ZnS 87

4.7: Simulated S K-edge XAS spectra for 2ML structural models.....88

4.8: Simulated S K-edge XAS spectra for 2ML CdSe/ZnS with crystal-bound thiols.....89

4.9: Simulated S K-edge XAS spectra for 2ML CdSe/ZnS with L-type amines.....90

4.10: Simulated S K-edge XAS spectra for 2ML CdSe/ZnS with Z-type thiols 91

4.11: Simulated S K-edge XAS spectra for 1ML structural models.....92

4.12: Simulated S K-edge XAS spectra for 1ML CdSe/ZnS with crystal-bound thiols.....93

4.13: Simulated S K-edge XAS spectra for 1ML CdSe/ZnS with L-type amines.....94

4.14: Simulated S K-edge XAS spectra for 1ML CdSe/ZnS with Z-type thiols 95

5.1: Synthesis of Cu_2S-Ru nanocages with DDT capping ligands at 205°C 100

5.2: Synthesis of Cu_2S-Ru nanocages with D3MP capping ligands at 205°C.....101

5.3: DSC of Cu_2S with crystal-bound D3MP capping ligands 102

5.4: Synthesis of Cu_2S-Ru nanocages with D3MP capping ligands at 220°C.....103

5.5: Synthesis of Cu_2S-Ru nanocages not using a primary amine.....106

5.6: Synthesis of Cu_2S nanorods by oriented attachment 108

5.7: Proposed scheme for the total synthesis of water soluble Cu_2S-Ru nanocages.....112

5.8: Proposed scheme for the total synthesis of water soluble Cu_2S-Pt hybrids.....113

A.1: ^{1}H NMR of dodecanethiol 119

A.2: ^{1}H NMR of dodecyl-3-mercaptoproionate.....120

A.3: ^{1}H NMR of Cu_2S with crystal-bound dodecanethiol 121

A.4: ^{1}H NMR of Cu_2S with crystal-bound DDT + D3MP 0h 122

A.5: ^{1}H NMR of Cu_2S with crystal-bound DDT + D3MP 24h 123

A.6: ^{1}H NMR of Cu_2S with surface-bound dodecanethiol 124

A.7: ^{1}H NMR of Cu_2S with surface-bound DDT + D3MP 0h 125

A.8: ^{1}H NMR of Cu_2S with crystal-bound DDT + D3MP 24h 126

A.9: ^{1}H NMR of 1,1'-didodecyldisulfide 127

A.10: ^{1}H NMR of didodecyl 3,3'-disulfanediyldipropionate 128

A.11: ^{1}H NMR of dodecyl 3-(dodecul-disulfanyl)propanoate 129

A.12: ^{1}H NMR of DDT and D3MP after 24h 130

A.13: Cu 2p XPS of Cu_2S nanocrystals with crystal-bound DDT 131

A.14: Cu 2p XPS of Cu_2S nanocrystals with surface-bound DDT 131

A.15: TGA of Cu_2S with crystal-bound DDT with regions used for MS highlighted 132

A.16: Mass spec of region I of Cu_2S with crystal-bound dodecanethiol 132

A.17: Mass spec of region II of Cu_2S with crystal-bound dodecanethiol 133

A.18: Mass spec of region III of Cu_2S with crystal-bound dodecanethiol 133

A.19: Mass spec of region IV of Cu_2S with crystal-bound dodecanethiol 134

A.20: Mass spec of region V of Cu_2S with crystal-bound dodecanethiol 134

A.21: Mass spec of region VI of Cu_2S with crystal-bound dodecanethiol 135

A.22: TGA of Cu_2S with crystal-bound DDT with regions used for MS highlighted 135

A.23: Mass spec of region I of Cu_2S with surface-bound dodecanethiol 136

A.24: Mass spec of region II of Cu_2S with surface-bound dodecanethiol 136

A.25: Mass spec of region III of Cu_2S with surface-bound dodecanethiol 137

A.26: Mass spec of region IV of Cu_2S with surface-bound dodecanethiol 137

A.27: Mass spec of region V of Cu_2S with surface-bound dodecanethiol 138

A.28: Mass spec of region VI of Cu_2S with surface-bound dodecanethiol 138

A.29: Full absorbance of Cu_2S after hydrolysis 140

A.30: Full absorbance of $CuInS_2$ after hydrolysis 141

B.1: Structural model of CdSe/ZnS with surface-bound ligands view along the A axis.....143

B.2: Structural model of CdSe/ZnS with bridging ligands view along the A axis 144

B.3: Structural model of CdSe/ZnS with crystal-bound ligands view along the A axis.....145

B.4: Structural model of propylamine 145

B.5: Structural model of $Zn(propanethiolate)_2$ 146

B.6: Structural models of $Zn(propionate)_2$.....146

B.7: S K-edge XAS spectrum of $Zn(thiolate)_2$ 147

CHAPTER I

INTRODUCTION

1.1 Introduction

Man-made nanocrystals are not a new concept; they have been around for hundreds if not thousands of years ago providing stunning artifacts that exhibited new macroscale properties not observed by other materials. The craftsmen were unaware that nanoscale features were a controlling factor in the colors of some pottery glazes and glasses.[1, 2] For modern day chemists, nanomaterials occupy an interesting and exciting new realm in materials chemistry, controlling properties using size effects.[3] By changing the synthetic procedure and the presence of additives, the size, shape, and/or composition of the nanomaterial can be tuned and thus affect the observed properties.[3] By understanding of the nature of the observed properties and how to control them synthetically the development of new and interesting nanomaterials for advanced applications becomes possible.[1, 3] Using this approach, nanomaterials are commercially available in a number of products ranging from sunscreen to displays.[1] As the field continues to learn more about controlling the synthesis of nanomaterials, new applications will become available and impact society.

In the Macdonald Laboratory here at Vanderbilt University, we focus on the controlled synthesis of nanomaterials. Specifically we develop synthetic methodology to control on the crystal-structure,[4-6] the morphology, heterostructures,[7, 8] and the surface chemistry of nanomaterials.[9, 10] My work has focused on surface chemistry and in this dissertation I will present my work towards unraveling the complexity that exists at the surfaces of nanomaterials

and how by understanding the surface chemistry we can tune their design for targeted applications.

In particular, we are interested in colloidal inorganic semiconductor nanocrystals, a promising class of nanomaterial for many optical and electronic applications.[11] Semiconductor nanocrystals are also known as quantum dots (QDs) when they exhibit a unique size dependent property called quantum confinement (Figure 1.1). Quantum confinement allows for control over the energy of the band gap and the redox potentials of the valence and conduction band with size for a given material. The physical source of quantum confinement originates when a semiconductor is smaller than the Bohr Exciton radius of the materials.[12] The Bohr exciton radius is the equilibrium distance in a bulk material between a bound electron-hole pair.[13] The effect of quantum confinement is that as the size of the particle decreases the energy needed to excite the electron increases: band gap increases. Quantum confinement can be defined by the Brus equation(1.1):[14]

$$E_{ex} = \frac{\hbar^2 \pi^2}{2R^2}\left(\frac{1}{m_e} + \frac{1}{m_h}\right) - \frac{1.8e^2}{\varepsilon_2 R} + \frac{e^2}{R}\overline{\sum_{n=1}^{\infty} \alpha_n \left(\frac{S}{R}\right)^{2n}} \qquad (1.1)$$

Where E_{ex} is the change in energy of the band gap, R is the radius of the QD, m_e is the effective mass of the electron, m_h is the effective mass of the hole, $\hbar$ is the reduced Planck's constant, ε_2 is the dielectric constant of the material, α_n relates to the dielectric constant of the material and the surrounding environment, and S is the wavefunction of the 1S exciton. Overall, the equation defines three interactions: energy of localization, Columbic attraction, and energy of solvation. At smaller radii, the energy of localization term dominates the equation since it scales by R^{-2}.[14]

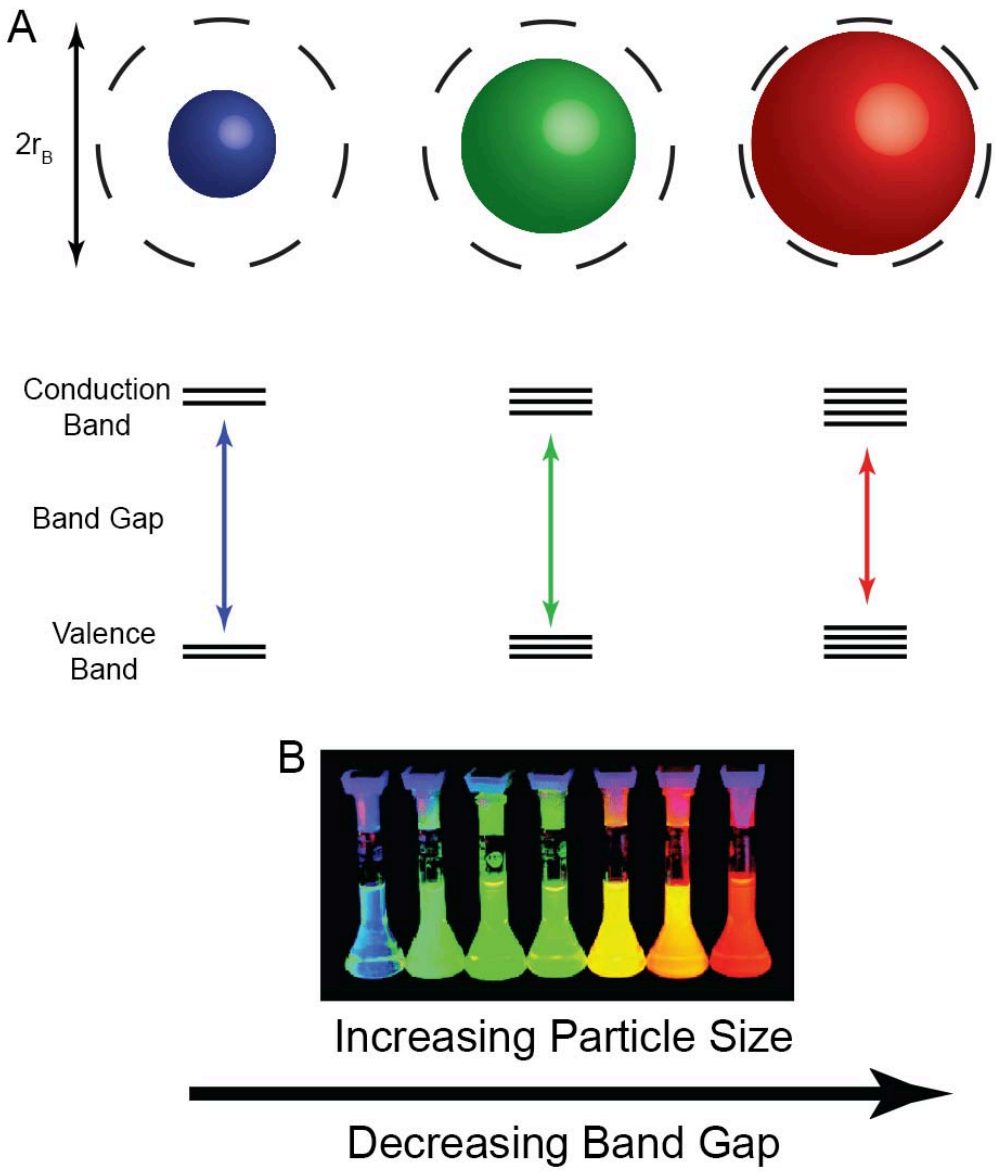

Figure 1.1: (A) Cartoon depiction of quantum confinement where decreasing sized particles result in a blue-shift in color resulting from the removal of orbitals at the edges of the valance and conduction bands, increasing the band gap. (B) Picture of CdSe@ZnS quantum dots with increasing CdSe core size from left to right. Picture adapted from ref. 11.

Quantum confinement can also be explained from a molecular orbital perspective. The binding of the atoms in a bulk material creates distinct bands of filled orbitals (valence band) and unfilled orbitals (conduction band) with a gap between the two bands (band gap). As atoms

are removed from a QD there is a depletion of states at the band edges, which will decrease the valence band edge and increase the conduction band edge, increasing the band gap.[12]

The size tunable band gaps using quantum confinement is just one factor contributing to the study of QDs. QDs also exhibit high molar absorptivities with broad absorption profiles and high fluorescence quantum yields with narrow line widths in comparison to molecular fluorophors. From a synthetic perspective, the solution chemistry used to make QDs allows for lower temperatures and avoids the use of expensive fabrication techniques, such as top down lithographic techniques that is also used to synthesize nanomaterials.[11] Additionally, these synthetic procedures leave the surfaces covered with organic surfactants that allow for the formation of stable colloidal solutions. Dispersions of QDs are required for biological labeling[15] and catalysis, and also are important for device fabrication allowing for low cost solution processing, such as roll-to-roll printing.[11] Currently, QDs are commercially used in biological labels and in displays such as TVs and tablets. With continued research, future applications of QDs advanced electronics such as solar cells and solid-state lights.

1.2 Colloidal Synthesis of Quantum Dots

In colloidal nanocrystal synthesis the conversion of initial inorganic precursors by a chemical process (such as decomposition, reduction, oxidation, sulfurization, etc.) is used to produce the solid nanocrystal.[16] Figure 1-3 shows the progression of precursor to nanocrystal through two distinct intermediates, monomers and nuclei.

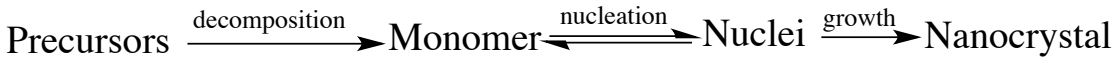

Figure 1.2. Chemical reactions leading from precursors to nanocrystals

There are three main components in the synthesis of nanocrystals: precursors, surfactants, and a solvent. The presence of the surfactants allow for the formation of nanocrystals. Surfactants bind to the surface decreasing the surface energy yielding the otherwise should be unstable nanocrystal.[17] In some cases the surfactant can play multiple roles in the synthesis, most commonly acting as the solvent.[18] However, there are even cases where the surfactant can act as a precursor,[19] and it is these reactions that have been the focus of my work.

Alkanethiols are common surfactants that can act as a sulfur precursor for the synthesis of metal sulfide nanocrystals. The use of alkanethiols has been used to make a wide range of metal sulfide nanocrystals, often yielding high quality monodisperse particles.[19-24] In my thesis I am going to focus on two cases, nanocrystals of Cu_2S and shells of ZnS.

In nanocrystal synthesis, the role of surfactants and use of different precursors can be explained by classic nucleation theory and the La Mer model of burst of nucleation.

1.2.1 Classic nucleation theory

When surfactants coordinate to the surface of a nanocrystal they become ligands, and the effects of the ligand binding can be attributed to classic nucleation theory. In short, there is a trade-off in the formation of materials between the presence of a new surface, which is unfavorable, and the favorable addition of volume to the particle.[16] The Gibbs free energy of the system can be defined assuming a spherical particle by the equation (1.2):[25]

$$\Delta G_n(r) = \frac{4}{3}\pi r^3 \Delta G_V + 4\pi r^2 \gamma \qquad (1.2)$$

Where γ is the surface energy, ΔG_V is free energy per unit volume, and r is the radius of the particle. The maximum of this equation is called the critical radius (r_c), which is the smallest

size of a stable nuclei, at smaller sizes the particles will dissolve back to monomers (Figure1.4).[25] As mentioned previously, the coordination of ligands will impact the surface energy of the resulting in a lowering of the γ term.[16] The critical radius can be described by the equation (1.3):[25]

$$r_c = \frac{2\gamma}{\Delta G_V} \qquad (1.3)$$

Therefore, by lowering the surface energy, more stable nuclei are formed allowing for nucleation and subsequent growth to nanocrystals.

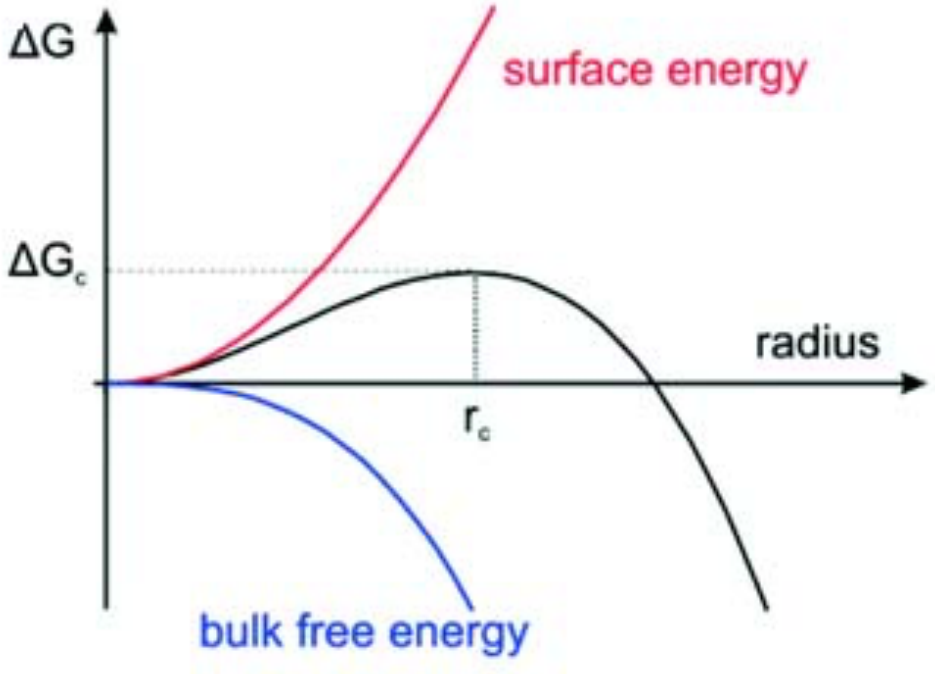

Figure 1.3: A plot of the free energy terms in nucleation theory. The blue plot is the free energy associated with the bulk, defined by the equation $\Delta G = \frac{4}{3}\pi r^3 \Delta G_V$. The red plot is the free energy associated with the surface, defined by the $\Delta G = 4\pi r^2 \gamma$. The black plot is the total free energy defined by the summation of the blue and red plots. Figure adapted from ref 25.

1.2.2 La Mer model of burst nucleation

The use of different precursors for nanocrystal synthesis can be understood by the La Mer model of burst nucleation.[26] Figure 1.4 is the plot of monomer concentration over time

during the La Mer model.[26] In Figure 1.4, during region I there is an increase in the concentration of monomers until reaching C_0, the minimum concentration needed for nucleation. In region II, nucleation occurs, upon reaching C_N, the critical concentration of nucleation.[26] At C_N the rate of nucleation causes the concentration of monomers to decrease and upon lowering past C_0 new nucleation is observed.[26] Region III is when nucleation stops and only growth is observed. Precursor choice plays a major role in tuning of the rates of nucleation and growth, which can influence the size, shape, and crystal-structure of resulting nanocrystals.[27, 28]

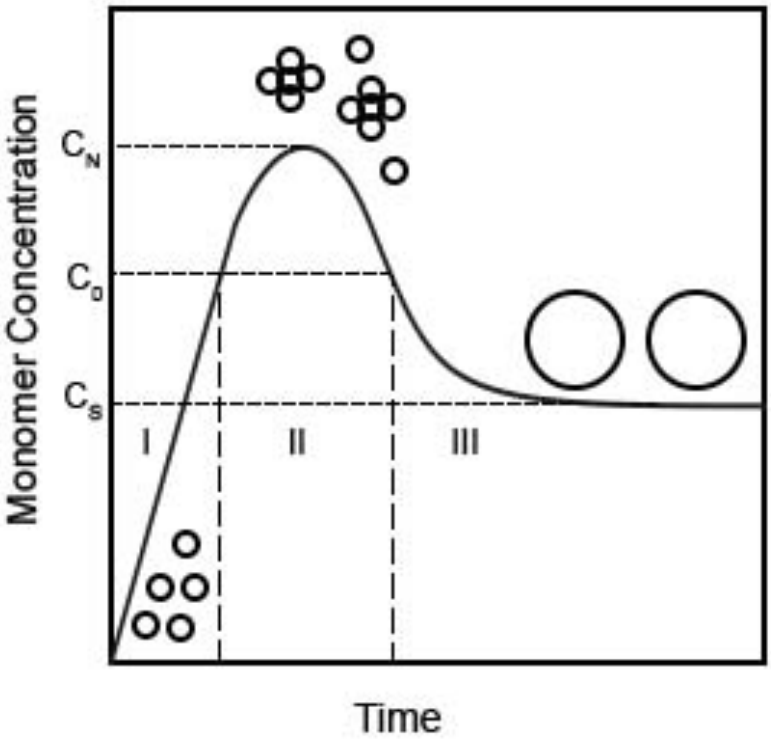

Figure 1.4: Plot of the change in monomer concentration with time during LaMer nucleation and growth.

Additionally, the La Mer model can be used to understand the mechanism for the size control of the Cu_2S nanocrystals using alkanethiols as the sulfur source. In the Cu_2S synthesis, nanocrystals around 12 nm are synthesized when only dodecanethiol is used as the sulfur

source, ligand, and solvent. Smaller particles are made by replacing some of the excess dodecanethiol acting as the solvent with dioctyl ether.[29] The new solvent changes the solubility of the monomers raising the concentration of supersaturation (C_s) leaving less free monomer for growth, resulting in smaller particles.

1.3 Surface Coordination of Ligands to Quantum Dots

1.3.1 The importance of ligands

As discussed in section 1.2, organic ligands play a significant role in the synthesis of QDs. After the synthesis of QDs, the surface is coated with a final layer of organic ligands, making the quantum dot a hybrid material consisting of an inorganic core and an organic shell.[18] In addition to the synthetic requirements, ligands also have a significant impact on the properties and solubility of the quantum dots.[30] Electronically, ligand coordination to the surface can passivate surface trap states decreasing the presence of mid-gap states improving fluorescence quantum yield.[30] Ligands can also be used to influence the electronic structure of the QD by electronically coupling to the orbitals in the valence or conduction band.[31]

1.3.2 Types of surface coordination

The most common organic ligands used in the synthesis of QDs are long-chain organics with a polar head group that coordinates to the surface. These ligands all render the QDs soluble in non-polar solvents and are insulating which inhibits charge transfer. Therefore the native ligand shell needs to be modified to provide functionality to the QDs; in the exchange processes of the ligands the coordination at the organic-inorganic interface plays a major role.

The classification of surface-bound ligand coordination on QDs is similar to Green's notation used in organometallic chemistry (Figure 1.5).[32-34] Ligands can coordinate as an anion to excess metal atoms on the surface to balance charge and terminate the lattice (X-type), such as oleic acid, dodecanethiol, or the phosphonic acids, or as a neutral dative bond (L-type, lewis basic), as in oleylamine, trioctylphosphine oxide, and trioctylphosphine.[33]

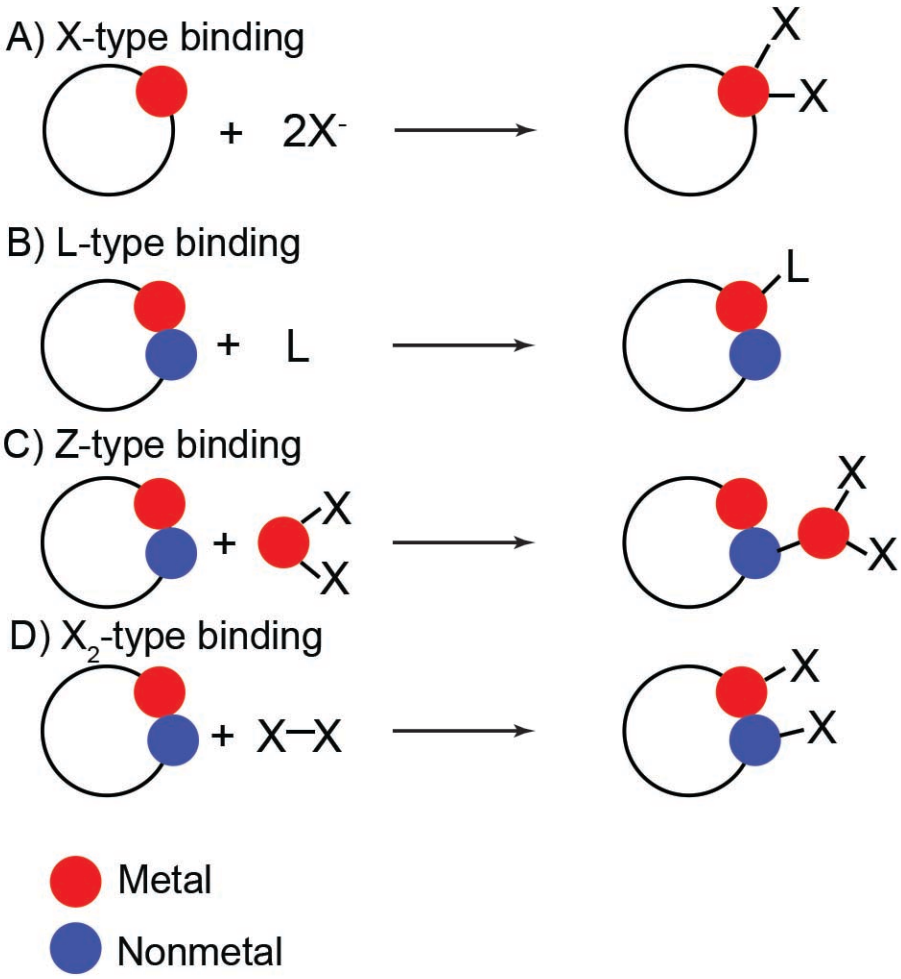

Figure 1.5: Schemes for the coordination of ligands to the surface of quantum dots. (A) X-type coordination where a negative charged species coordinates to a metal atom on the surface. (B) L-type coordination where a neutral compound binds through a dative bond to surface metal atom. (C) Z-type coordination where a metal complex binds to a surface nonmetal site. (D) X_2-type coordination where two X-type ligands one with a negative charge binds to a surface metal atom and one with a positive charge that binds to a surface nonmetal site.

An understanding of ligand exchange processes is often used to clarify the nature of ligand coordination (Figure 1.6). Since there is a charge difference between X-type and L-type ligands the observed displacement of formally X-type ligands by L-type ligands and vice versa has led to the notation of two additionally classes of surface-bound ligands, Z-type and X_2-type ligands.[32, 35] A Z-type is a neutral acceptor (Lewis acid) whereas the X_2-type ligand is a neutral species in solution that upon binding to the surface of the crystal dissociates into two ligands one that is positively charged and one that is negatively charged. Typical Z-type ligands observed in nanocrystals are metal complexes with additional X ligands, such as a cadmium oleate complex acting as the ligand where the Cd can accept electrons from surface anion sites.[32] The X_2-type coordination involves the disproportionation of the capping ligand into both positive and negative capping ligands; an example is the coordination of oleic acid to the surface of some metal oxides as an anionic oleate and a cationic hydrogen.[35] To date the X_2-type binding has only been observed on the surface of some metal oxides and inorganic perovskites.[35] The use of ligand classification can be a valuable tool for understanding the role ligands play on the surface, however the simplistic nature of the classification does not account for the complexity that can exist on a nanocrystal surface, such as different surface facets and edge sites.

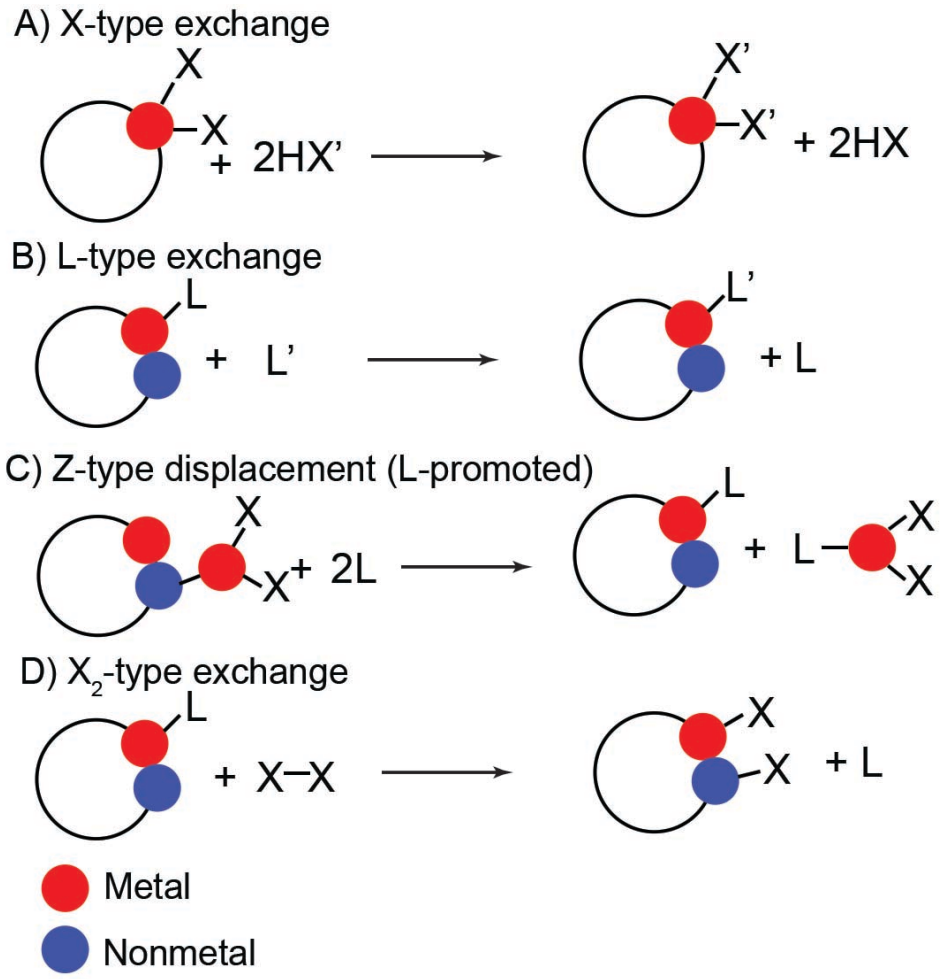

Figure 1.6: Schemes for ligand exchange on the surfaces of quantum dots. (A) The exchange of X-type ligands for a different X-type ligand. (B) The exchange of L-type ligands by a different L-type ligand. (C) The L-promoted displacement of Z-type ligands where an additional L-type ligand coordinates to the metal center of the Z-type ligand promoting displacement and allowing coordination of the L-type ligand. (D) X_2-type exchange where L-type ligands are replaced by the coordination of dissociation of a neutral species to positive and negative components on the surface.

Our group and others have noticed that when alkanethiols are used as the sulfur source in the synthesis of metal-sulfides the native capping ligands were resistant to exchange. Often these native thiol capping ligands would bind as the X-type thiolate to the surface. Thiolate coordination is often the strongest and commonly used for X-type exchange to yield water-soluble particles. However, even with native thiolate ligands, there should be an equilibrium

between bound and free ligands, and X-type exchange can be achieved using La Chateliers principles. Since this exchange was inhibited, I preformed the surface analysis to identify the nature of the capping ligand, which resulted in the discovery of a new ligand binding mode, crystal-bound ligands.

1.4 Techniques for the Surface Characterization of QDs

There are many techniques used to characterize the coordination of ligands to the surface of QDs. The techniques used in Chapters 2 and 3 will be presented and what they reveal about the surface chemistry will be discussed.

1.4.1 Nuclear Magnetic Resonance (NMR)

NMR is the workhorse instrument in chemistry for the identification of organic molecules; this remains true for the surface analysis of quantum dots.[36] NMR allows for the identification of different chemical environments by probing transitions between nuclear spin states in the presence of a magnetic field. NMR has several advantages in the surface analysis of nanocrystals:[36] It is a nondestructive technique that allows for in situ measurements, it can be quantitative with the addition of internal standards, and it can identify free and bound species. However, NMR is limited in the direct analysis of the surface coordination because dipolar effects of the metal atoms in the nanocrystal core along with the slow tumbling rate of the nanocrystal broaden out the resonances near the surface. Therefore, NMR is used as a means to gain a relative understanding of the nature of the organic ligands. This is done using a series of 1D and 2D NMR experiments.

In my work, I primarily used 1D NMR techniques for the analysis of the ligands, identifying ligand density and changes upon chemical perturbations. The quantification of density is one of the most common uses of NMR of QDs.[37] For this measurement, an internal standard is used to identify the concentration of bound ligands in a sample. By knowing the size and concentration of the nanocrystals, the ligand density can be determined.

By perturbing the NMR sample changes in the organic ligands can be observed. This takes advantage of NMR's ability to distinguish between free and bound species. I primarily have studied the surface chemistry of nanocrystals capped with dodecanethiol. For dodecanethiol capped QDs, the broadening of the resonances near the surface of the QD means that there are only two observed resonances for bound dodecanethiol at 0.88 ppm and 1.2 ppm corresponding respectively to the terminal CH_3- and the -CH_2- units of the organic chain (Figure 1.7).[9] In contrast, free dodecanethiol would have additional resonances at 2.5 ppm and 1.6 ppm. By adding an additional chemical to the NMR tube surface effects can be observed by the changing spectra. In Chapter 2, I added an additional thiol to the NMR tube and observed disulfide formation as a way to probe oxidative stability of the native thiol ligand coordination.[9] In another study presented in Chapter 3, when base was added to the samples the stability of ligands towards removal was determined.[10]

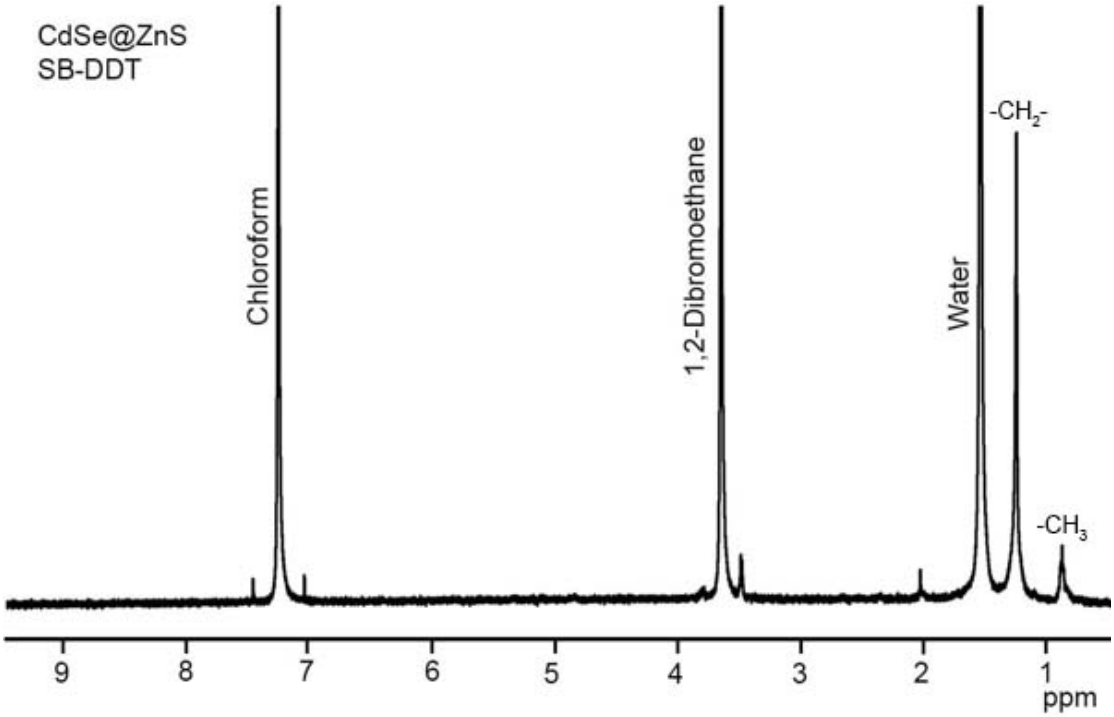

Figure 1.7: Example ^{1}H NMR of dodecanethiol capped CdSe@ZnS QDs in $CDCl_3$. 1,2-Dibromoethane is added as an internal standard. The peak at 0.88 ppm corresponds to the terminal -CH_3 resonance and the peak at 1.2 ppm corresponds to the -CH_2- resonances of the alkyl chain.

1.4.2 X-ray Photoelectron Spectroscopy (XPS)

XPS provides detailed information on the chemical nature of the elements present in a sample. This is aquired by measuring the kinetic energy (KE) of a photoexcited electron emitted from a core orbital upon irradiation of the sample with monochromic x-ray excitation.[38] The measured KE allows for the determination of the binding energy (BE) of the chemical species by the equation (1.4):

$$BE = h\nu - KE \quad (1.4)$$

Where $h\nu$ is the energy of the x-ray source. The BE of an electron is dependent on the specific element and oxidation state of that element, such that an increase in electron density on an atom will make it easier to remove an electron, decreasing the binding energy. Since the measured

species is an electron, XPS has limited penetration depth associated to the mean free path of the electron in sample. This makes XPS particularly sensitive to surface composition of around 10 nm.

Primarily, the high-resolution S2*p*-orbital spectra are used to identify the presence of surface-bound thiolates. Compared to the binding energy of the S2*p* orbital in the crystalline material the thiolate would have a higher binding energy since it is in a higher oxidation state with less electron density. In the XPS spectra of non *s*-orbitals each unique species will have two peaks resulting from spin-orbital coupling. The nature of the spin-orbital coupling originates from the coupling of the remaining unpaired electron to the angular momentum of its orbital. *S*-orbitals have a spherical orbital with no angular momentum; therefore there is no spin-orbital couple. For *p*- and *d*- orbitals, the total spin of the system can be determined by the equation (1.5):

$$j = l + s \quad (1.5)$$

Where j is the total spin, l is the *l*-quantum number representing the angular momentum of the orbital, and s is the spin of the electron. The spin of an electron is either +1/2 of -1/2 depending on the spin of the ejected electron, which is the nature of the two spin states. For *p*- and *d*-orbitals the l-quantum number is 1 or 2 respectively resulting in total spins of 1/2 and 3/2 for *p*-orbitals and 3/2 and 5/2 for *d*-orbitals. The ratio of the intensities of spin states is equal to 2j+1 of the spin-states, so for *p*-orbitals there is a 2:1 ratio for the 3/2 peak to the 1/2 peak and for the d-orbital there is a 3:2 ratio for the 5/2 peak and the 3/2 peak.

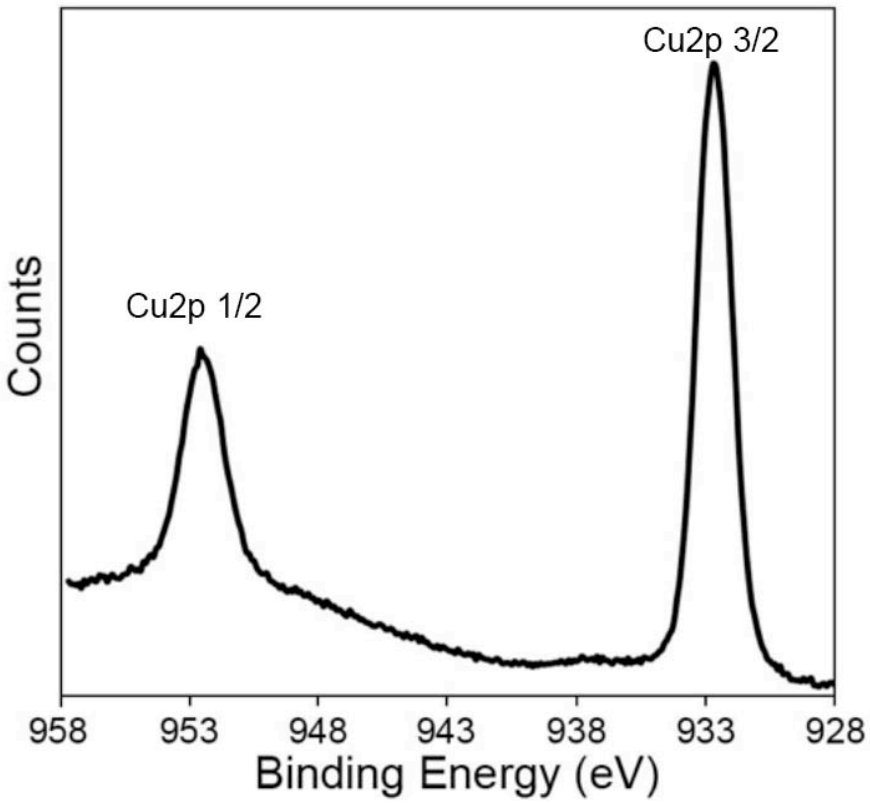

Figure 1.8: Sample high-resolution XPS spectra of the Cu 2p region of Cu_2S.

1.4.3 Thermogravametric Analysis-Mass Spectrometry (TGA-MS)

TGA-MS combines two lab instruments, a TGA and a gas chromatography mass spectrometer (GC-MS). In TGA, the change in mass of a sample is measured upon heating. In the context of QDs the mass loss is a result of the decomposition of the organic capping ligands.[37] The addition of the GC-MS to the set-up allows for the off gas to be directly analyzed. Identification of the decomposed organics can reveal details about the composition of the surface and the potential for surface catalyzed decomposition reactions.[9] Mass spectrometry works by ionizing a compound and measuring the mass to charge ratio. Hard ionization techniques such as electrospray ionization can lead to fragmentation that can allow for the chemical structure of the initial compound to be identified.

1.5 Scope of the thesis

Understanding the fundamental chemistry that governs nanocrystal surfaces is paramount for the development of advanced applications. Chapter 2 will address the surface characterization preformed leading to the identification crystal-bound ligands. Crystal-bound ligands are formed as a result of the use of thiols as the sulfur source in the synthesis of metal sulfides. This difference was determined by comparing the surface of Cu_2S nanocrystals synthesized with and without thiols. We became interested in understanding this surface chemistry because our laboratory and others have been unsuccessful in surface functionalization of these particles using ligand exchange. Chapter 2 will also contain our method of circumventing the need of ligand exchange for surface functionalization of these particles.

Chapter 3 extends the crystal-bound surface chemistry to the synthesis of ZnS shells on CdSe with crystal-bound thiols. During this study we observed unexpected changes in the optical properties of the QDs. Using our knowledge of the surface chemistry we were able to identify the origin of the change in properties and then take advantage of the effects to improve the photocatalytic activity of the QDs for the degradation of methylene blue.

In all of the previous work done on the surface analysis of QDs, including my own, the techniques used do not directly probe the ligand surface interface. Chapter 4 is on my work towards developing computational models to use X-ray Absorption Spectroscopy (XAS) as a means to directly probe this interface.

Chapter 5 will present my work toward using crystal-bound ligands to control growth and assembly of nanocrystal systems. Two unique reactions will be discussed: my attempt at the synthesis of water-soluble Cu_2S-Ru cage-hybrid nanocrystals and the ligand directed

oriented attachment of Cu_2S nanocrystals to nanorods. The ability to synthesis a wide range of shapes and heterostructures of nanocrystals increases the potential functionality of the nanocrystal.

Finally, Chapter 6 will be a conclusion and my outlook how my work relates to the greater context of my field.

CHAPTER II

IDENTIFICATION AND FUNCTIONALIZATION OF CRYSTAL-BOUND LIGANDS[I]

2.1 Introduction

In this chapter my work towards the identification and surface functionalization of Cu_2S nanocrystals will be discussed. There has been considerable interest in using semiconductor nanocrystals for biomedical,[15] electronic,[11] and alternative energy applications.[39] This interest stems from the optical properties, which can be tuned by particle size though quantum confinement and by adjusting the composition. Even a slight change of size, morphology or composition of nanocrystals has a considerable effect on the optical properties including the energies of the absorption onset, fluorescence emission,[17] and surface plasmons. Thus, syntheses to monodisperse, single crystalline nanocrystals are desired. While there are many ways to synthesize nanocrystals, solution-based colloidal synthesis often yields the highest quality, most monodisperse samples, with uniform properties.[17]

Typical solution syntheses of nanocrystals in organic solvents involve the chemical transformation of dissolved molecular inorganic reagents to solids. This is performed in the presence of ligands to coordinate to the nanocrystal surfaces. The ligands lower the surface energy and allow for the thermodynamically unfavorable nanocrystals to be kinetically trapped.[40] The ligands possess a long alkyl chain that provides solubility in the high boiling organic solvents required for the synthesis and a polar head group to bind to the surface.

[I] Part of this Chapter has been published previously in Turo, MJ and Macdonald, JE "Crystal Bound vs. Surface-Bound Thiols in Nanocrystal Synthesis" *ACS Nano*, **2014**, 8, 10205-10213.

Common head groups are phosphines, phosphine oxides, carboxylic acids, phosphonic acids, amines, or thiols.

Thiols are in a special category of ligands because they can concomitantly act as the sulfur source in syntheses of metal sulfide nanocrystals.[19-24, 29, 41-48] At high temperatures, thiols decompose on the metal centers to yield the metal sulfide and an alkene.[19] At the termination of the reaction, the particles are capped with a final layer of intact thiols.

The use of thiols as a sulfur source for nanocrystal synthesis has become increasingly common as the products are often of very high quality. For example, syntheses of monodisperse, single-crystalline, shape-controlled particles of copper sulfide[19, 20, 29, 41, 42, 49] and mixed copper sulfides[24, 43-46] use this technique. Thiols have also been employed as a sulfur source for shelling quantum dots of CdSe with ZnS and CdS to improve fluorescence yields and reduce blinking.[21-23, 48]

Several groups including the Macdonald laboratory have noted that copper sulfides prepared with thiol sulfur precursors are resistant to ligand exchange procedures for surface functionalization and to impart water solubility.[44, 50] The inert surfaces will preclude the use of these nanocrystals in most biomedical, sensor and photocatalytic applications. In quantum dot sensitized photovoltaic devices, these tightly bound thiols would need to be removed to improve inter-particle conductivity.[51]

Besides the empirical observation of poor ligand lability, here I present ^{1}H NMR, X-ray Photoelectron Spectroscopy (XPS) and ThermoGravimetric Analysis – Mass Spectrometry (TGA-MS) studies to provide evidence that when thiols are used as a sulfur source, the capping thiols are bound to the surface of the nanocrystals in a chemically different manner than typical ligand-surface interactions. When thiols only serve as ligands, they are bound to cations at low

coordination number surface sites which we describe as "surface-bound" (Figure 2-1).[32, 33] The capping thiols that result from reactions where they are also the sulfur source become the terminal layer of sulfurs of the crystal. These thiols are exceptionally strongly bound because they sit in in high coordination number sites. We call these "crystal-bound thiols" (Figure 2.1).

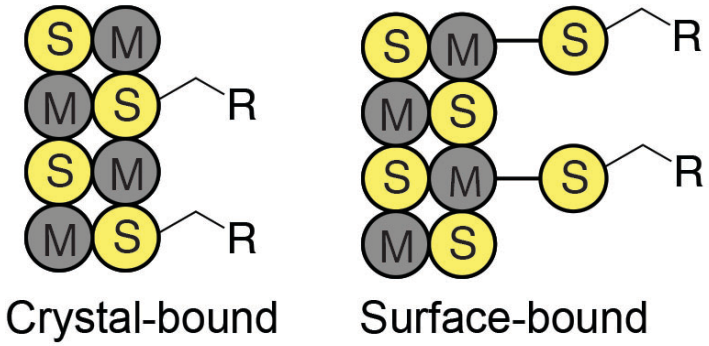

Figure 2.1: Two binding modes of thiol ligands on metal sulfide nanocrystals.

Furthermore, I present a simple and broadly applicable method to achieve water solubility of metal sulfide nanocrystals synthesized with thiol precursors. Dodecyl-3-mercaptopropanoate (D3MP), a long chain thiol with a mid-chain ester, was synthesized and used to replace 1-dodecenethiol as a ligand and sulfur source for representative syntheses of Cu_2S and $CuInS_2$ nanocrystals. The mid-chain ester can be readily cleaved to make otherwise immutably organic soluble particles transfer into water.

2.2 Results and Discussion

2.2.1 Evidence for crystal-bound thiols

To gather evidence for the chemical uniqueness of crystal-bound thiols, Cu_2S nanocrystals were prepared by two methods to give surfaces capped by crystal-bound and surface-bound thiols both with the chalcocite crystal structure. Cu_2S nanocrystals with crystal-

bound dodecanethiol (DDT) were prepared according to literature procedure by heating $Cu(acac)_2$ with dodecanethiol at 200°C in dioctyl ether (DOE) solvent.[19, 29] The single crystalline particles were 6.9 ± 0.5 nm (n=188). Cu_2S nanocrystals with surface-bound thiols were prepared by a modified literature procedure[52] whereby $Cu(acac)_2$ was allowed to react with sulfur powder at 200°C in oleylamine (OLAM) and oleic acid (OA) to give 6.8 ± 1.1 nm (n=169) nanocrystals. After the reaction, the particles underwent a ligand exchange with DDT (Figure 2.2). The ligand exchange to DDT capping ligands was confirmed by IR spectroscopy, which showed the disappearance of the carbonyl stretch of oleic acid (Figure 2.3). Powder XRD shows that both the crystal-bound DDT sample and the surface-bound DDT sample are both chalcocite (Figure 2.4)

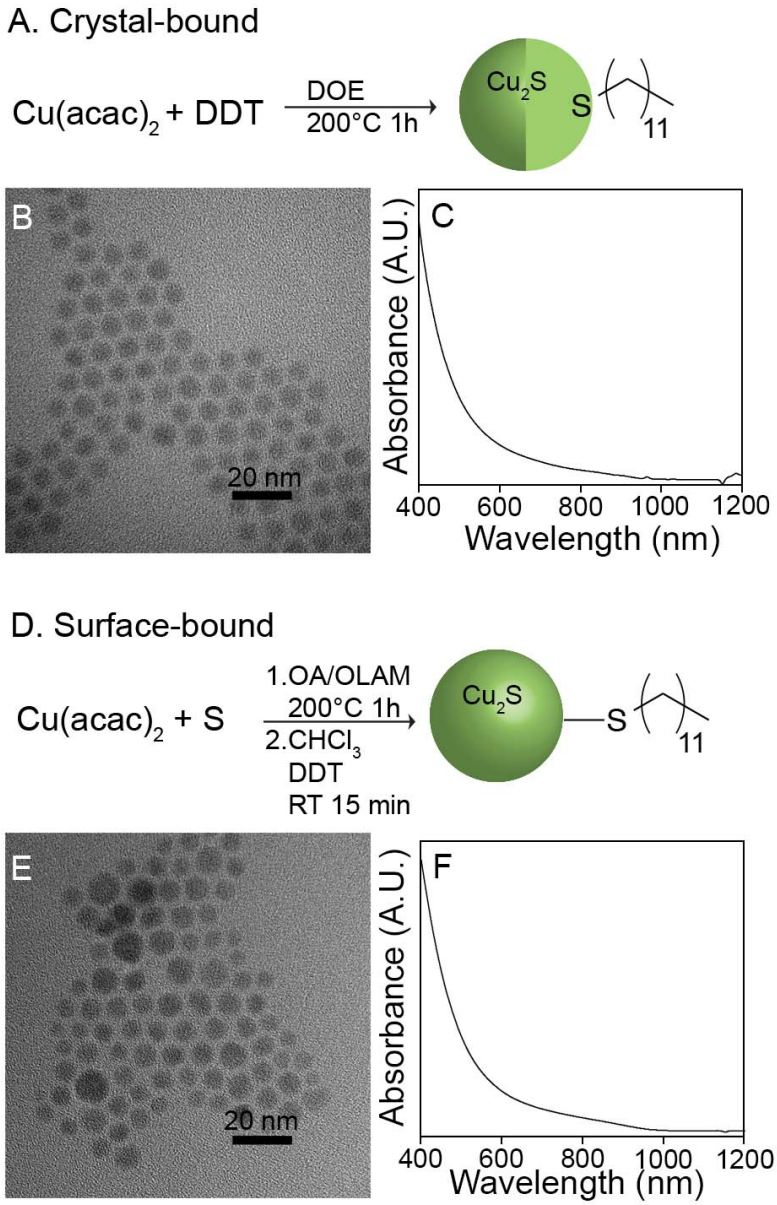

Figure 2.2: (A) Synthesis of Cu_2S nanocrystals with crystal-bound dodecanethiol capping ligands. (B) TEM of Cu_2S nanocrystals with crystal-bound ligands, d = 6.9 ± 0.5 nm n = 188. (C) Absorbance spectrum of Cu_2S nanocrystals with crystal-bound ligands. (D) Synthesis of Cu_2S nanocrystals with surface-bound dodecanethiol. (E) TEM of Cu_2S nanocrystals with surface-bound ligands, d = 6.8 ± 1.1 nm, n = 169. (F) Absorbance spectrum of $Cu_{2-x}S$ nanocrystals with surface-bound ligands.

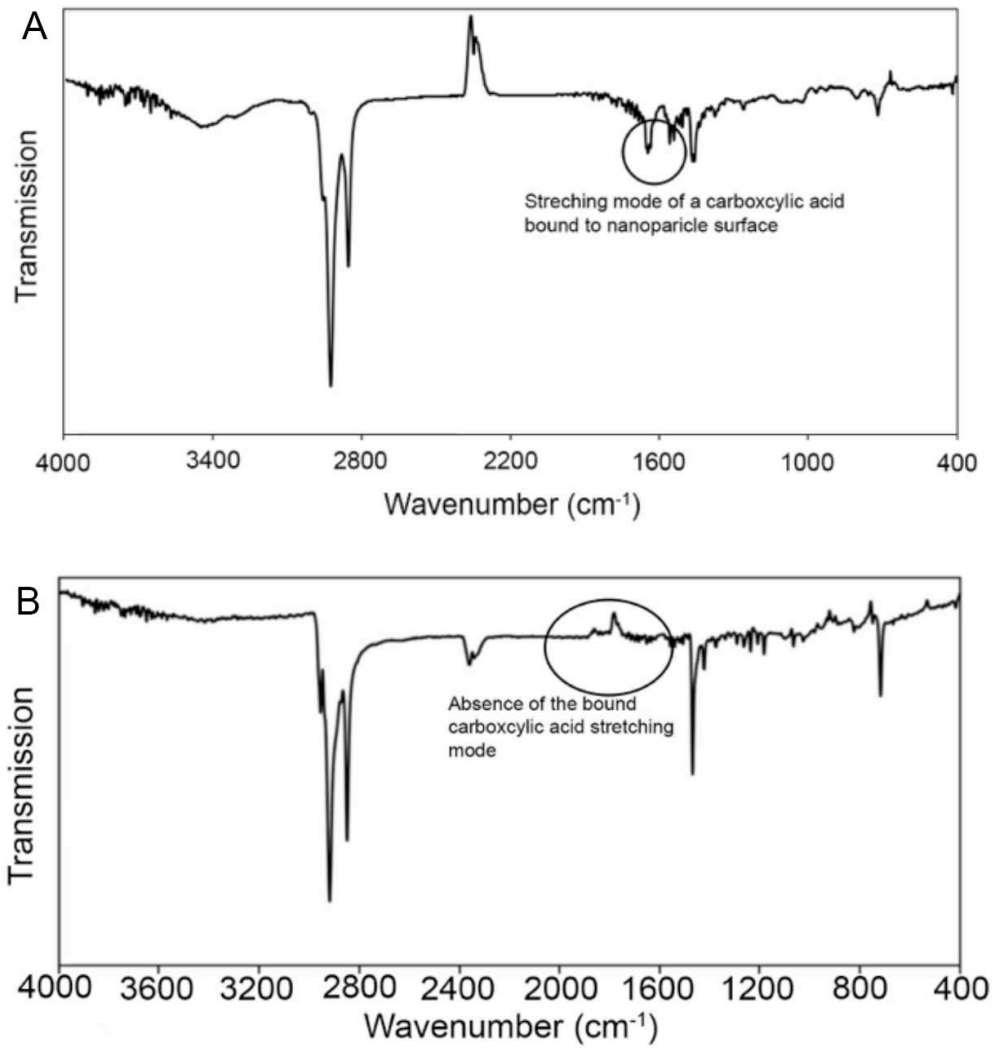

Figure 2.3: IR of Cu_2S nanocrystal with native oleic acid before (A) and after (B) ligand exchange showing the removal of the native oleic acid capping ligands and the replacement by dodecanethiol.

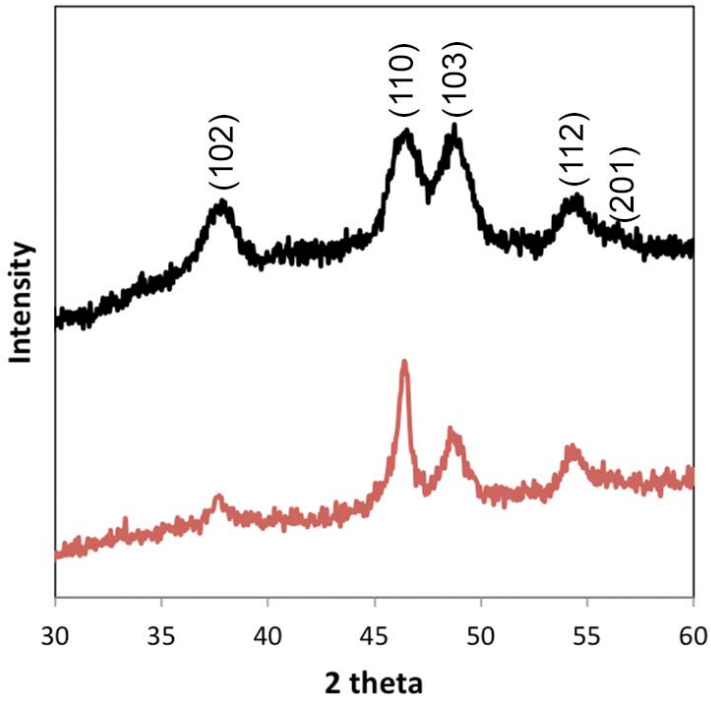

Figure 2.4: X-Ray diffraction pattern of Cu_2S nanocrystals with crystal-bound dodecanethiol (black) and surface-bound dodecanethiol (red). Both diffraction patterns are indexed to chalcocite Cu_2S, JCPDS 26-1116.

NMR is a powerful technique for the determination of the interactions between ligands and nanocrystal surfaces.[32, 36, 53-55] Changes in the NMR spectrum resulting from perturbations allow for the dynamic interactions between the ligands and the nanocrystal to be observed. The initial NMR studies on crystal-bound ligands followed previous reported methods employing these 2D NMR techniques. Unfortunately, the protons near the particle surface are often not observed by ^{1}H NMR due to dipolar effects of the metal atoms and the slow tumbling rate of the nanocrystal.[36] To accurately identify the exchange using there needs to be a clear resonance that distinguishes between free and ligands. Often this is accomplished using a ligand with a suitable mid-chain NMR signal such as the double bond of oleic acid or oleylamine. [32, 36, 53-55] Untimely, our 2D experiments were unsuccessful because DDT does not have such

unsaturation. Instead I examined the hetero-exchange between the native DDT on the particle surface to D3MP, which has distinctive ^{1}H NMR signals (Figure 2.5) as compared to DDT.

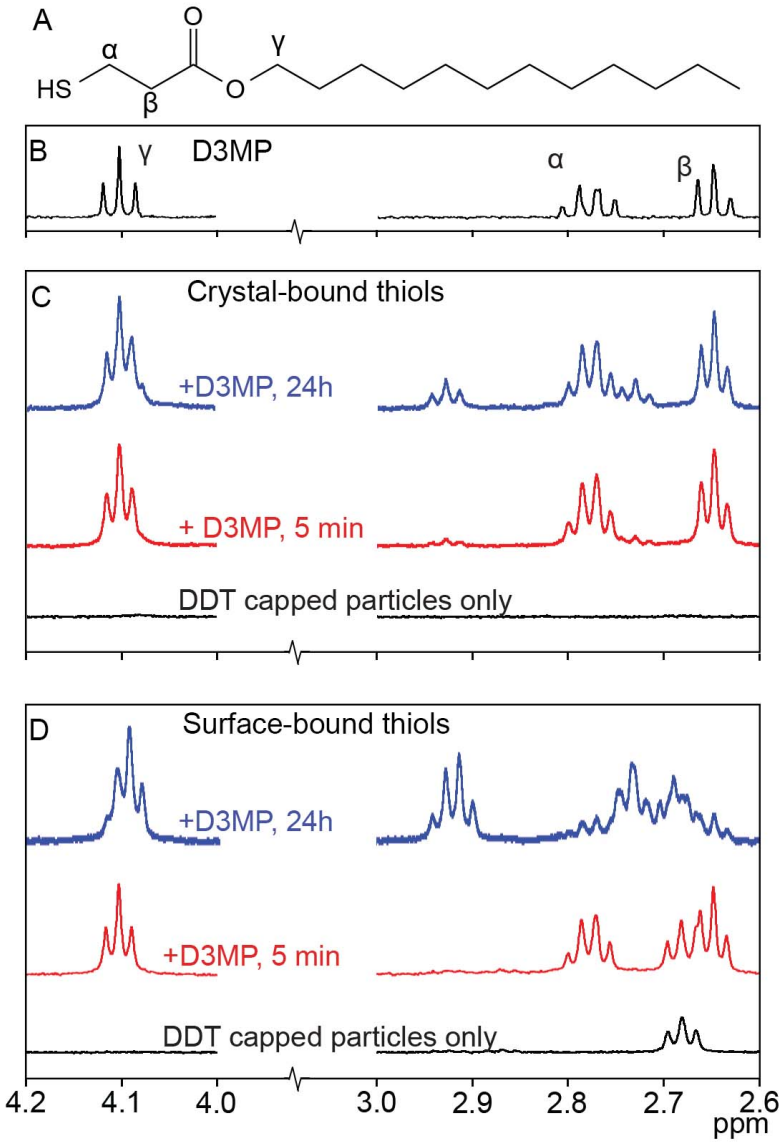

Figure 2.5: (A) Structure of D3MP. (B) Partial ^{1}H NMR spectrum of D3MP. (C) ^{1}H NMR spectra for Cu_2S nanocrystals with crystal-bound dodecanethiol (black), 5 min after the addition of 2 molar equiv. of D3MP (red) and at 24 h after addition (blue). (D) ^{1}H NMR spectra for Cu_2S nanocrystals with surface-bound dodecanethiol (black), 5 min after the addition of 2 molar equiv. of D3MP (red) and at 24 h after addition (blue).

^{1}H NMR of the thiol and sulfur derived nanocrystals are shown in part in Figure 2-5 and in full in Appendix A. In the regions reported in Figure 2-5 A, there are no peaks that can be

assigned to DDT; however, a small amount of 1,1-didodecyldisulfide[56] (Appendix A) was observed in the surface-bound sample. Disulfide formation on nanocrystal surfaces has been observed previously for thiol capped semiconductor nanocrystals[57, 58] and has limited the stability of the particles in solution.[57]

To the NMR tubes containing the DDT capped nanocrystals, 2 molar equivalents of D3MP as compared to the DDT capping ligands were added. In both the crystal-bound and surface-bound samples (Figure 2.5), the addition of the new ligand caused the expected appearance of signals from D3MP: a triplet at 4.10 ppm, a quartet at 2.77 ppm, and a triplet 2.65 ppm, labeled γ, α, and β respectively.

After 24h in the ^{1}HNMR solution in the presence of D3MP and exposure to ambient light and atmosphere, the crystal-bound thiols on Cu_2S showed much greater chemical stability than surface-bound thiols. For crystal-bound thiol samples small peaks at 2.92 and 2.73 ppm as well as a small shoulder on the peak at 4.10 ppm were observed which can be assigned to the formation of didodecyl 3,3'-disulfanediyldipropionate, the disulfide of two D3MP molecules (Appendix A). The disulfide formation is known to be surface mediated.[58] This suggests that there are a small number of exposed coordination sites when crystal-bound ligands are expected. There is however no evidence that the exposed surface is a result of the native ligands dissociating from the nanocrystal surface.

In contrast to nanocrystals with crystal-bound thiols, there was evidence of mobility of the native ligands on nanocrystals with surface-bound thiols after 24h in the ^{1}HNMR solution in the presence of D3MP and exposure to ambient light. The ^{1}H NMR showed a decrease in the concentration of free D3MP resulting from a high rate of formation of disulfides. Disulfides form more readily because of the dynamic nature of the native capping thiols. In addition to

didodecyl 3,3'-disulfanediyldipropionate, there were also peaks at 2.7-2.75 ppm and offset but overlapping peaks at 2.91 ppm and at 4.10 ppm which we assign to two additional disulfides, 1,1-didodecyldisulfide and the mixed disulfide, dodecyl 3-(dodecyldisulfanyl)propanoate (Appendix A). The disulfides which contain DDT units are a direct result of the removal of the native DDT bound to the nanocrystal surface. These DDT containing disulfides are not observed in the crystal-bound case because the native ligands are non-labile. The disulfides present in this NMR experiment were also synthesized by standard organic syntheses to obtain control for the NMR spectra (Appendix A).

The sum of the ^{1}H NMR study shows that, when thiols are used as the sulfur source in the synthesis of Cu_2S, the resulting capping thiols have significantly different surface chemistry than if the thiol is simply exchanged onto the surface. While surface-bound thiols are labile and prone to oxidative disulfide formation, crystal-bound thiols are non-labile and resistant to oxidation.

X-ray Photoelectron Spectroscopy (XPS) was employed to further identify differences in the surface chemistries between crystal-bound and surface-bound thiol ligands. The S2*p* region of Cu_2S with crystal-bound DDT (Figure 2.6A) was compared to that of Cu_2S with surface-bound DDT (Figure 2.6B). Efforts were made to minimize the exposure of the samples to air prior to analysis to prevent oxidation of the copper sulfide,[59] and ^{1}H NMR showed that no free thiol was present.

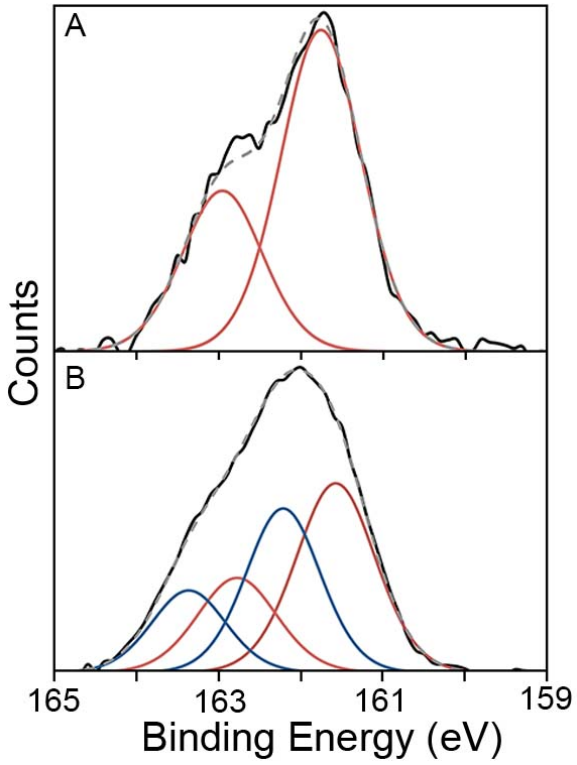

Figure 2.6: S2p XPS spectra of Cu_2S nanocrystals with (A) crystal-bound DDT capping ligands and (B) surface-bound DDT capping ligands.

For the nanocrystals with crystal-bound DDT, the peak in the XPS S2*p* region was best fit by one set of spin-orbital coupled peaks at 161.8 eV and 163.0 eV, and was assigned the S in the Cu_2S crystal lattice.[59] Nanocrystals with surface-bound DDT were best fit by two sets of spin orbital couples. The lower energy set is at 161.6 eV and 162.8 eV and arises from the sulfur in the Cu_2S crystal lattice. A second set with a higher binding energy was fitted at 162.2 eV and 163.4 eV and can be attributed to thiolate bound to the surface of Cu_2S.[60] The absence of the peaks for thiolate binding to the surface of Cu_2S in the crystal-bound sample is indicative that the thiol capping ligands are not simply bound to individual surface Cu, but rather bound into higher coordination sites within the crystal lattice.

TGA-MS also points to very different surface chemistries between crystal-bound and surface-bound thiols (Figure 2.7, 2.8, and Appendix A). For both Cu_2S nanocrystals with surface-bound and crystal-bound thiols, there is a large mass loss between 200°C and 300°C. Mass spectrometry of the species emanated is dominated by 1-dodecene which can be formed from alkyl-migration and β-hydride elimination of the thiols on the surface.[61] Above 300°C Cu_2S nanocrystals with crystal-bound ligands shows almost no mass loss, whereas almost 20% of the mass lost for Cu_2S nanocrystals with surface-bound ligands occurs at these higher temperatures. Above 300°C, the ion in the mass-spectrometry has a m/z consistent with S_2, disulfide, the most abundant ion seen in mass spectrometry of gas phase sulfur from the decomposition of metal sulfides.[62, 63]

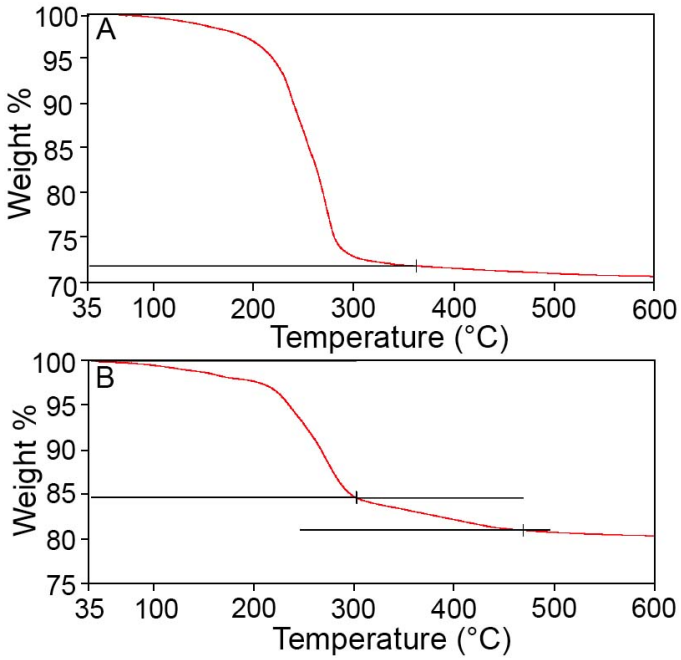

Figure 2.7: (A) TGA of Cu_2S nanocrystals with crystal-bound dodecanethiol. (B) TGA of Cu_2S nanocrystals with surface-bound dodecanethiol. MS traces of the emanated species are included in Appendix.

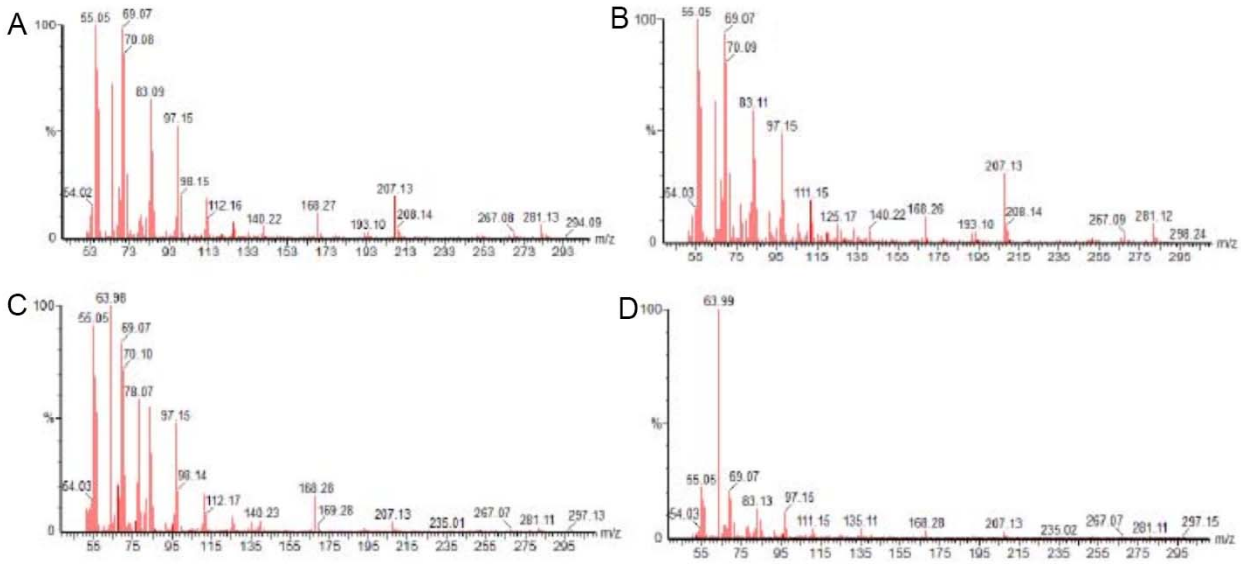

Figure 2.8: representative mass spectra of the TGA-MS data shown in figure 2-7. (A) crystal-bound DDT bellow 300°C, (B) crystal-bound DDT above 300°C, (C) surface-bound DDT below 300°C, and (D) surface-bound DDT above 300°C

After β-hydride elimination of dodecene, the remaining S on the Cu_2S surface is different for crystal-bound *vs.* surface-bound thiols. Surface-bound thiols will leave sulfur in in low coordination sites, which is removed at higher temperatures. Crystal-bound thiols leave sulfurs in high-coordination sites, which prevents further mass loss of the sulfur.

Using NMR, XPS, and TGA-MS, I was able to experimentally show there is a fundamentally different surface chemistry when thiols are used as the sulfur source compared to ligand exchange. It is worth noting that all of the techniques used either require the removal of the organic ligand from the surface (NMR and TGA-MS) or does not provide detailed structural analysis (XPS). Chapter 4 will address my attempts to establish more advanced techniques to more directly probe the organic-inorganic interface.

2.2.2 Water solubility of the copper sulfides with crystal-bound ligands

Since the robust binding mode of crystal-bound thiols make the particles immune to ligand exchange at moderate temperatures, an alternative method is needed to impart chemical modification to the nanocrystal surface to allow water solubility. At the same time, a methodology was desired that would not greatly alter the established syntheses of the high quality particles yielded when a long chain thiol was the sulfur source. Initial studies involved the use of 11-mercaptoundecanoic acid (MUA) and MPA as the sulfur source; however, this led to lower quality particles and higher decomposition temperatures. Recently, work by Tao *et al.* has shown that Cu-MUA complexes decompose at higher temperatures than Cu-DDT complexes in solid-state decomposition reactions.[64] The higher temperature can be attributed to the acid group coordinating to the surface of other Cu-thiol clusters, preventing decomposition and nucleation. To avoid additional coordination from the acid group or hydrogen bonding effects of the ligand, we chose to modify the ligand alkyl chain by adding a mid-chain ester. By using D3MP the ester group will provided protected chemical functionality. Purified D3MP was synthesized in multi-gram scale by using a Fischer esterification from inexpensive reagents, 3-mercaptopropanoic acid (MPA) and 1-dodecanol (Figure 2.9).[65]

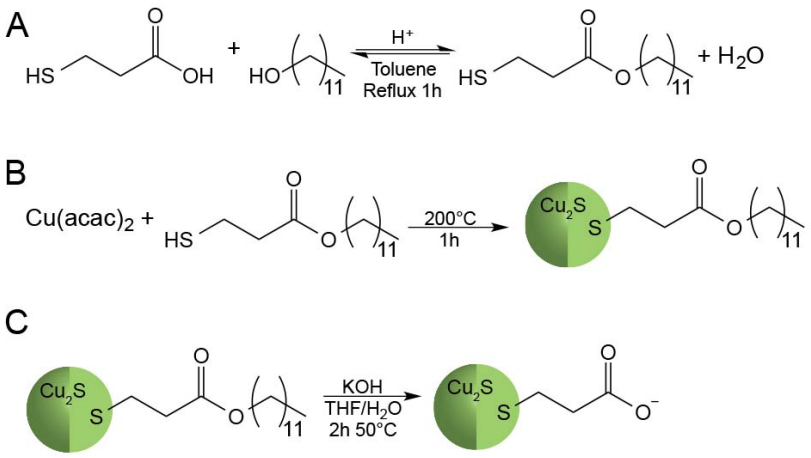

Figure 2.9: (A) The synthesis of dodecyl-3-mercaptopropanoate from 3-mercaptopropionic acid and 1-dodecanol. (B) The synthesis of Cu_2S using D3MP as the sulfur source. (C) Base catalyzed hydrolysis of the D3MP capped particles.

D3MP was used instead of DDT in the synthesis of Cu_2S nanocrystals. The transmission electron microscopy (TEM) image (Figure 2.10) shows the resulting 11.9 ± 0.9 nm (n = 222) Cu_2S particles packed into a superlattice, indicating highly monodisperse particles.[17, 41] The phase was confirmed to be chalcocite Cu_2S by Selected Area Electron Diffraction (SAED) (Figure 2.11).

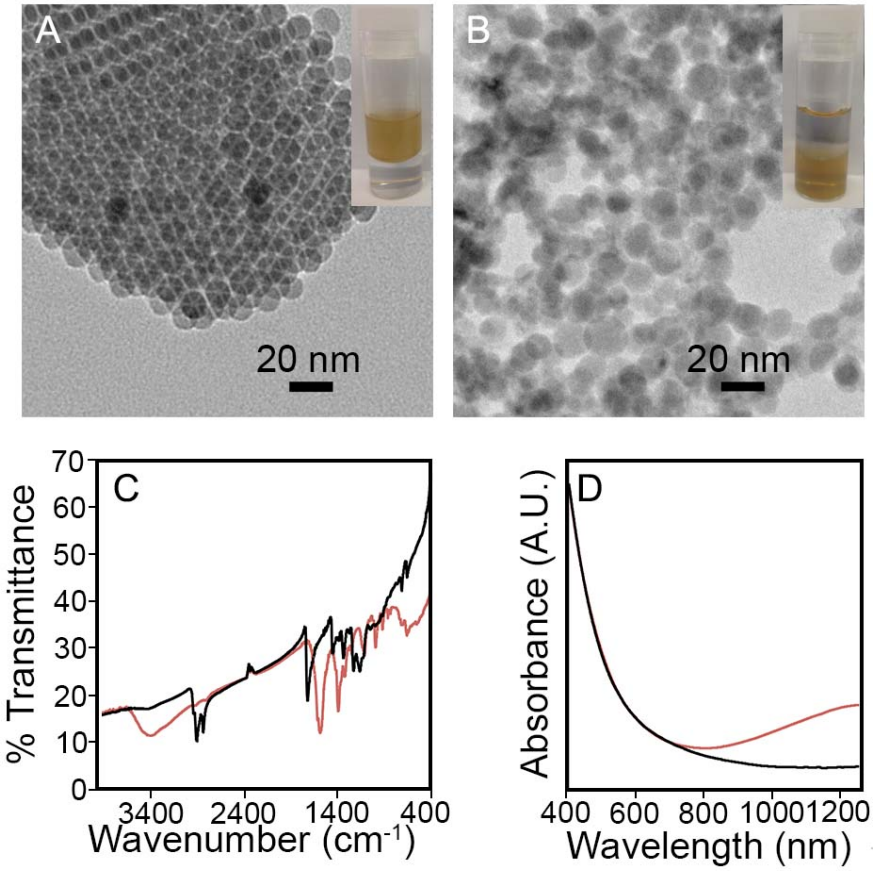

Figure 2.10: (A) TEM of Cu_2S synthesized using D3MP as the sulfur source, 11.9 ± 0.9 nm n = 222. Inset is a photograph of the particles dissolved in hexanes phase above a water layer. (B) Particles after hydrolysis of the ligand, 13.0 ± 2.0 nm n = 237. Insert is a photograph of the particles dissolved in water below a layer of hexanes. (C) Infrared spectrum of Cu_2S before (black) and after (red) hydrolysis (D) Normalized absorbance spectra of Cu_2S before the hydrolysis dispersed in hexanes (black) and after the hydrolysis dispersed in water (red).

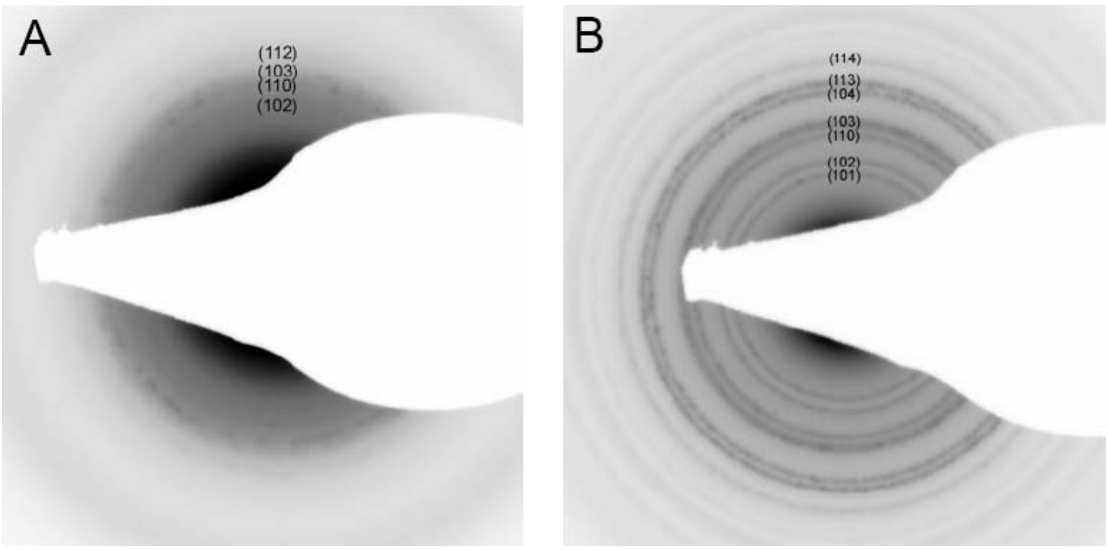

Figure 2.11: Selected area electron diffraction of Cu_2S with crystal-bound D3MP, before (A) and after (B) hydrolysis. The SAED pattern for Cu_2S before hydrolysis is indexed to chalcocite Cu_2S, JCPDS 26-1116. The SAED pattern for Cu_2S after hydrolysis is indexed to Djurleite $Cu_{1.96}S$, JCPDS 29-0578

In a post-synthesis step, a base hydrolysis cleaved the mid-chain ester to leave the surfaces capped with a corona of carboxylates, rendering the particles water-soluble (Figure 2.9). TEM revealed that the hydrolysis did not significantly change the size of the particles (Figure 2.12). Infrared spectroscopy confirmed the cleavage of the ligand (Figure 2.10C) from the D3MP ester to a deprotonated MPA carboxylate, as the ester carbonyl stretching mode at 1737 cm^{-1} was replaced with two modes at 1606 cm^{-1} and 1402 cm^{-1} representing the symmetric and asymmetric stretches of a carboxylate. In addition, the C-H stretching mode between 3000-2800 cm^{-1} decreases in intensity from the loss of the long alkyl chain.

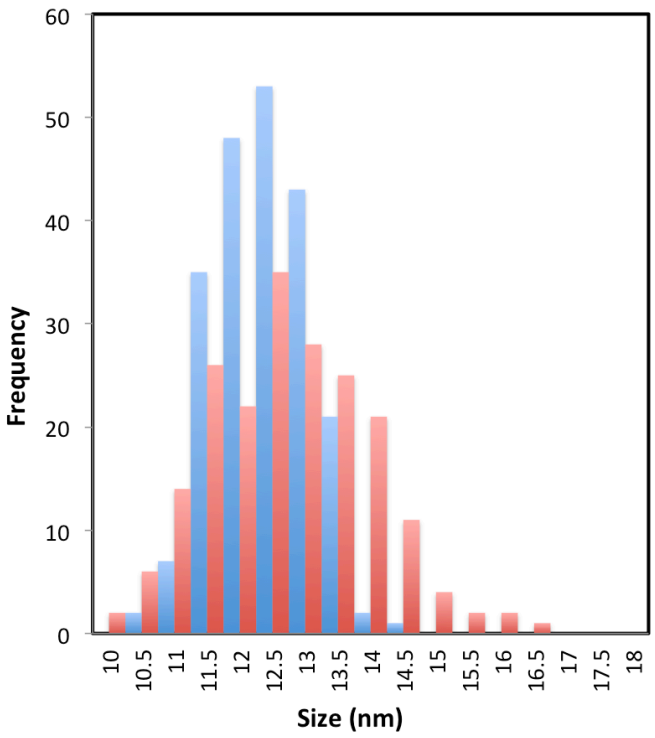

Figure 2.12: Histogram of the sizes Cu_2S nanocrystals after hydrolysis as measured by TEM. Blue is before hydrolysis and red is after hydrolysis.

The hydrolysis resulted in a change in the optical properties of the Cu_2S. While the initial synthesis gave an absorbance spectrum consistent with Cu_2S, a broad surface plasmon resonance in the near infrared region of the absorbance spectrum developed (Figure 2-9) during the hydrolysis that is indicative of substoichiometric $Cu_{2-x}S$.[66] SAED was consistent with the substoichemetric Djurleite crystalline phase which is closely related to chalcocite (Figure 2-11). The free carrier density was determined by dissolving the water-soluble particles in anhydrous THF and collecting a spectrum into the near-IR. The larger solvent window of THF was needed in order to observe the peak of the plasmon (Appendix A).[67] Using Drude's relationship between the bulk plasmon frequency and the carrier density, N_h, the carrier density was determined to be 3.56×10^{20} cm^{-3}, which corresponds to a stoichiometry of $Cu_{1.98}S$ (Appendix A).

The leaching of the Cu^{2+} cations into solution is not unprecedented for crystal-bound ligands on Cu_2S nanocrystals. Previous work has shown that when dodecanethiol was used as the sulfur source in the synthesis of Cu_2S, cation exchange reactions to CdS or PbS are possible.[68] As crystal-bound thiols are part of the anion sublattice of the Cu_2S, the cations still have access to the solution. The combination of robust ligand binding with open surface cation sites on particles with crystal-bound thiols may have important implications for the development of stable nanocrystal catalysts.

During the hydrolysis, an additional insoluble black precipitate often formed. The precipitate was determined to be a CuO impurity by XRD (Figure 2.13). It has been shown previously that Cu^{2+} ions leached from the oxidation of Cu_2S in the presence of a base and a surfactant can form CuO.[69, 70] The dodecanol liberated during the ester hydrolysis is capable of performing this function. However, the Cu_2S is only a small source of the copper ions that form CuO as there was a negligible size change after the hydrolysis and a minimal change in stoichiometry from Cu_2S to $Cu_{1.98}S$. Therefore, we attribute the formation of the CuO from the presence of a copper impurity remaining from the synthesis that is especially difficult to remove from the nanocrystals when the nanocrystals are capped with D3MP.

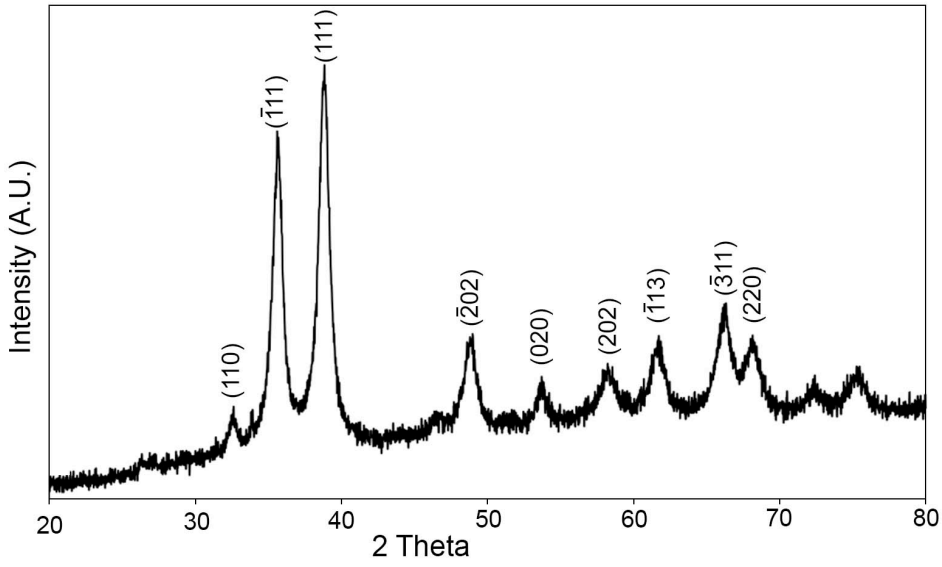

Figure 2.13: Powder X-ray diffraction of insoluble CuO precipitate, JCPDS: 05-661.

Cu_2S is the parent structure to a large family of mixed cation copper sulfides including copper indium sulfide, copper gallium sulfide, copper indium gallium sulfide, and copper zinc tin sulfide.[71] The wide range of compositions of the mixed copper sulfides allow for tunable optical and electronic properties and have been extensively researched for energy related applications. Nanocrystals of these materials, like those of Cu_2S, can be synthesized using thiols as a sulfur source to obtain high quality products.[24, 45-47] To demonstrate the broader applicability of our approach towards preparing water-soluble nanocrystals with crystal-bound thiols, $CuInS_2$ was synthesized[24] using D3MP. Copper and indium salts were heated in neat D3MP (Figure 2.14) resulting in 2.41 ± 0.29 nm (n = 132) nanocrystals. The phase was confirmed to be chalcopyrite $CuInS_2$ by SAED and the stoichiometry $Cu_{1.2}In_{1.2}S_2$ by Energy Dispersive Spectroscopy (EDS). The nanocrystals were subjected to the same hydrolysis procedure as the Cu_2S to give water soluble $CuInS_2$ (Figure 8B). SAED confirmed the phase remained chalcopyrite $CuInS_2$ (Figure 2-15) and the size was not significantly altered (2.34 ± 0.27 nm, n = 140). As in Cu_2S, the phase transfer caused the formation of a surface plasmon

resonance in the absorbance spectrum of the $CuInS_2$ (Figure 2.14) which is known to be accompanied by a blue shift in the band gap which is also observed.[72] The carrier density was calculated to be 1.44×10^{-21} cm^{-1}, the final stoichiometry was determined by quantitative EDS to be $Cu_{0.77}In_{0.90}S_{2.00}$ (Figure 2.15) and the phase confirmed by SAED to remain chalcopyrite $CuInS_2$ (Figure 2.16). Currently, we are developing milder hydrolysis procedures to aid in the phase transfer of these highly sensitive materials without the changes in stoichiometry and optical properties.

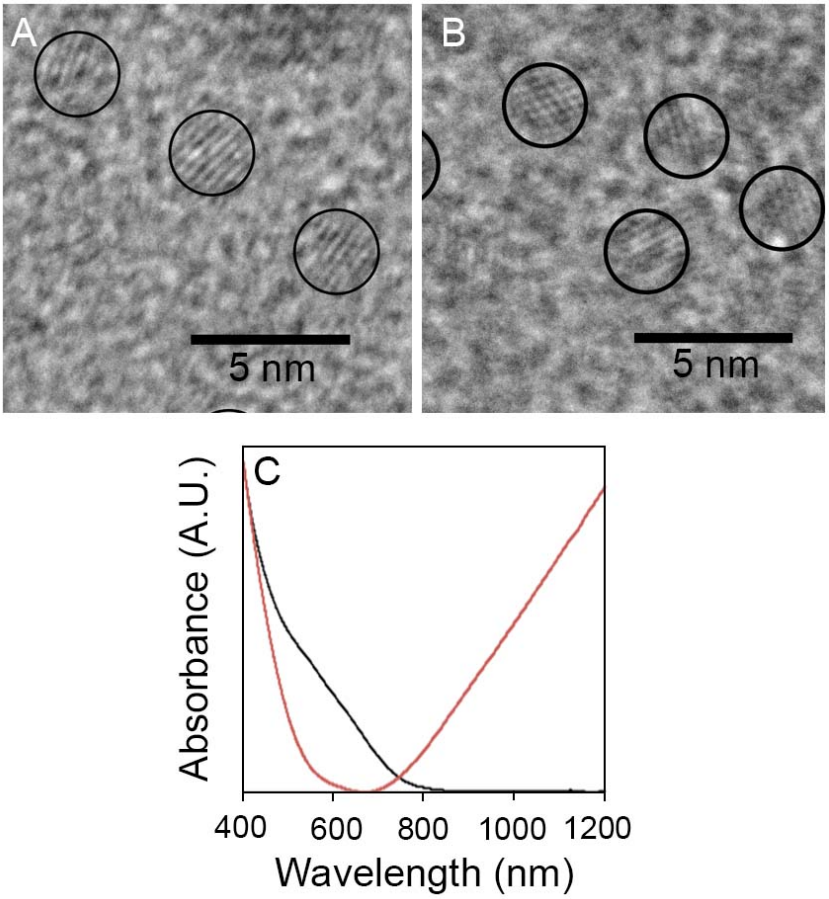

Figure 2.14: (A) TEM images of $CuInS_2$ synthesized using D3MP as the sulfur source, 2.41 ± 0.29 nm, n = 132, (B) and after ester hydrolysis, 2.34 ± 0.27 nm, n = 140. (C) The normalized absorbance spectra of $CuInS_2$ before the hydrolysis dispersed in hexanes (black) and after the hydrolysis dispersed in water (red).

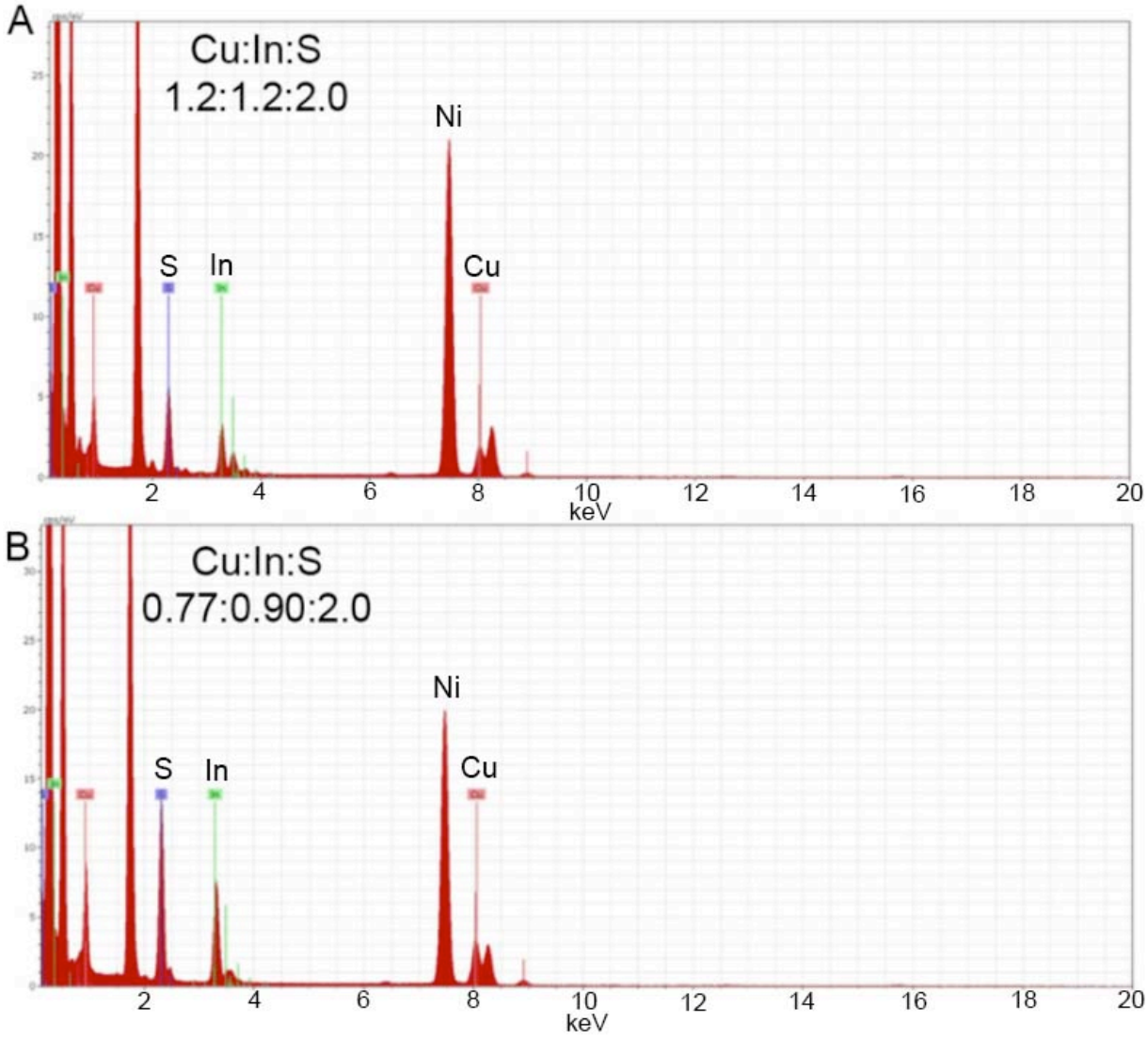

Figure 2.15: The EDS of $CuInS_2$ before (A) and after (B) hydrolysis. The peak labels are red for Cu, green for In, and blue for S. Impurities in the spectra are from the Ni TEM grid. The quantification of the Cu:In:S ratio for each spectrum is reported.

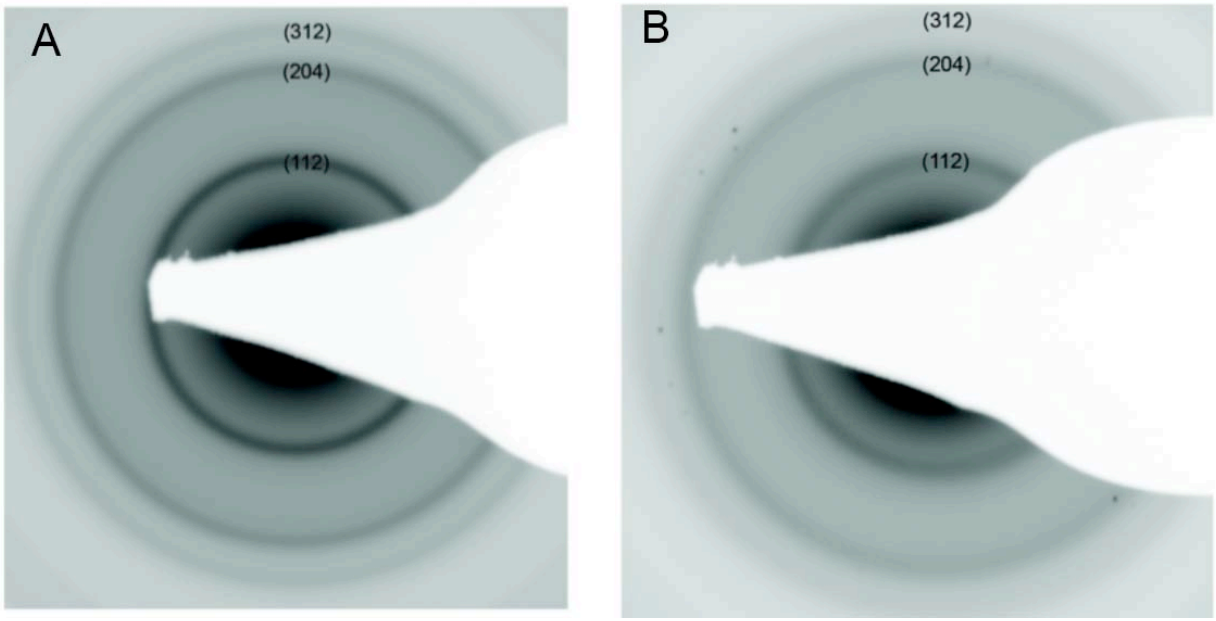

Figure 2.16: The SAED of $CuInS_2$ with crystal-bound D3MP before (A) and after (B) hydrolysis. Both diffraction patterns are indexed to chalcopyrite $CuInS_2$, JCPDS 27-159.

This was the first report of using a simple hydrolysis procedure to phase transfer nanocrystals and is now being adopted by others. For example, Wu *et al*. utilized a similar procedure to synthesize water soluble copper zinc tin sulfide nanocrystals for solar cells, utilizing octyl-2-mercaptoacetate followed by a hydrolysis procedure to remove the majority of the organic ligands.[73]

2.3 Conclusion

Previous attempts at rendering nanocrystals prepared with thiols as the sulfur precursors water-soluble through ligand exchange were often ineffective. ^{1}H NMR, XPS and TGA reveal the surface chemistry is different between "surface-bound" ligands and "crystal-bound" ligands produced when thiols are used as sulfur sources. We explain the inert surfaces and more tightly

bound ligands as a result of the sulfur atom of the thiol capping ligands occupying higher coordination sites in the crystal lattice.

Previously, Wang *et al.* hinted at the possibility of high coordination number binding of thiols in a figure in their report of a similar synthesis of Cu_2S, but did not fully characterize or discuss this assignment.[74] Additionally, researchers at Samsung used language suggesting the presence of crystal-bound binding mode in a 2008 patent on using thiols as the sulfur source of QDs.[75] However, they did not fully characterize or describe the surface. I believe this is the first thorough characterization of the unique crystal-bound binding mode this synthetic route affords. Our description of this high coordination number binding mode of thiols on a nanocrystal surface is reminiscent of the "stapling" that has unambiguously been identified on thiolated gold clusters by X-ray crystal structure analysis.[76] In the staples, Au atoms are removed from the Au cluster surface to so that the thiolates have a gold coordination number of two. The decomposition of thiols on metal atoms to give metal sulfide nanocrystals has been well established for Cu,[77] Pd,[78] and Ni[79] and it is possible that high coordination number binding of thiols also occurs in these cases.

To allow these high quality particles with crystal-bound thiols to be rendered water-soluble, a new, easily synthesized ligand, dodecyl-3-mercaptopropanoate, can be used as a replacement for alkane thiols in the synthesis of copper(I) sulfide and copper indium sulfide. The ester functionality was hydrolyzed, yielding nanocrystals with a corona of carboxylic acids, which makes them soluble in water. The ester also provides a chemical handle for further surface functionalization, for example, amide coupling which is a current topic of interest in our laboratory.[80]

2.4 Experimental Methods

Materials: Sulfur (reagent grade), 1-dodecanol (98%), 3-mercaptopropanoic acid (MPA, >99%), oleylamine (70%), oleic acid (90%), dodecanethiol (DDT, 97%), and dioctyl ether (99%) were obtained from Sigma Aldrich. Copper(II) acetylacetonate (97%) was obtained from Strem Chemicals. Indium(III) acetate (99%) was obtained from Alfa Aesar. All chemical were used as obtained without further purification. Standard air-free Schlenk techniques were used throughout with N_2 used as the inert gas. The glovebox used was also filled with N_2.

Copper (I) sulfide nanocrystals with crystal-bound ligands: Cu_2S was prepared following a modified literature procedure.[19] In a typical synthesis, $Cu(acac)_2$ (87.2 mg, 0.333 mmol) was dissolved in 2 mL of dodecanethiol and 8 mL of dioctylether and placed under vacuum for 1h. The solution was heated to 200°C under nitrogen. At 125°C, the solution turned a transparent yellow color and as the solution heated further it became orange, signifying the formation of the Cu-thiol complex. At 200°C the solution turned black, indicative of particle formation. The solution was reacted for 60 min at 200°C, then allowed to cool to room temperature under nitrogen. The reaction flask was then brought into a glovebox. The particles were isolated by the addition of ethanol followed by centrifugation. The supernatant was removed and the particles were suspended in chloroform and precipitated with ethanol 3×. The final product was stored in a glovebox to prevent oxidation to a substoichiometric copper sulfide.

Copper (I) sulfide with surface-bound ligands: Cu_2S was prepared following a modified literature procedure.[52] In a typical synthesis $Cu(acac)_2$ (261 mg, 1.00 mmol) was dissolved in 10 mL of oleylamine and 5 mL of oleic acid and placed under vacuum for 1h. The solution was the heated to 200°C under nitrogen. At 200°C, sulfur (16.0 mg 0.500 mmol) dissolved in 1 mL

of oleylamine was quickly injected. The reaction was allowed to proceed for 30 min. The solution was cooled to room temperature and brought into a glovebox. The resulting product was isolated by the addition of ethanol followed by centrifugation. The particles were then washed using chloroform and ethanol 3×. The final product was stored in a glovebox to prevent oxidation to a substoichiometric copper sulfide.

Ligand exchange of the native acid and amine ligands to surface-bound thiols: Cu_2S with surface-bound ligands was dissolved in a minimum amount of chloroform. To 1 mL of the saturated solution of Cu_2S nanocrystals, 0.5 mL of dodecanethiol was added. The solution was stirred at room temperature for 15 min in a glovebox. The particles were isolated by the addition of ethanol followed by centrifugation. The supernatant was removed and the particles were suspended in chloroform and precipitated with ethanol 2×. The final product was stored in a glovebox to prevent oxidation to a substoichiometric copper sulfide.

^1H NMR: ^{1}H NMR of the nanoparticle solutions were acquired using a 11.7 T magnet equipped with a Bruker DRX console operating at 500.13 MHz. Chemical shifts were referenced internally to $CDCl_3$ (7.26 ppm) which also served as the ^{2}H lock solvent, and a delay time of 2 sec was used. For the dynamic studies 1,2-dibromoethane was used as an internal standard for determination of the concentration of ligands present as part of the nanocrystal solution. The concentration was determined by comparing the integrations of the 1,2-dibromoethane peak at 3.65 ppm and the terminal -CH_3 group of the ligand at 0.88 ppm. The concentration of ligands in solution was around 1 mM. A solution of D3MP in $CDCl_3$ was then added to the NMR tube such that the molar amount of free ligand was equal to twice that of the bound ligand. The sample was then left for 24 hours in ambient light.

X-ray photoelectron spectroscopy (XPS): The samples were prepared in a glovebox and ^{1}H NMR in $CDCl_3$ confirmed there were ligands attached to the nanocrystals and that there were no residual free ligands present. The nanocrystals were then drop cast from a suspension in $CHCl_3$ onto a silicon wafer. XPS was performed using a Physical Electronics (PHI) VersaProbe 5000. The data were collected using Al K_α X-rays (1486 eV), a take-off angle of 45°, and a spot size of 100 μm. Peaks were fitted using CasaXPS software, calibrated to the lowest energy C 1s peak at 284.8 eV. In the S 2p spectra, the separation of the spin orbit couple was set to 1.15 eV and the peak areas fixed to a ratio of 2:1. The FWHM were constrained such that the spin orbit couples had matching FWHM but were otherwise allowed to fit freely. The FWHM were between 0.99 and 1.19 eV.

Thermogravametric analysis-mass spectrometry (TGA-MS): ^{1}H NMR in $CDCl_3$ of the nanocrystals confirmed there were ligands attached to the nanocrystals and that there was no residual free ligands present. Analysis was performed on a Perkin Elmer TL-2000 hyphenated TGA-GC-MS thermal analysis system. The GC column was a PerkinElmer Elite-5 (5% Diphenyl) Dimethylpolysiloxane Series Capillary Column with 0.25 mm inner diameter. Helium is used as the carrier gas at flow rate of 1mL/min. Samples were thermalyzed using a Perkin Elmer Pyris 1 TGA system. Sampling of the TGA oven atmosphere was controlled by a pneumatic Swafer(TM) valve system within the Clarus 680 GC instrument and the evolved gases were transported through a deactivated silica capillary to the head of the GC column. The capillary transport lined was heated isothermally at 200°C for the duration of the experiment. Samples were loaded onto the GC column at regular intervals during the thermolysis. The evolved gases were generated, separated and analyzed using MS under the following conditions: Splitless injected of gases onto the GC column was done at 200°C as

drawn from the TGA. GC oven temperature was keep isothermal at 250°C for the duration of the run. Total ion count was recorded by the Clarus SQ 8C MS for the range of 50 < m/z < 300. The TGA was run using ~10-20 mg of sample in Pt pans. The TGA oven was purged with Helium at a rate of 100 mL/min during the run. TGA samples were held isothermally for 4 minutes at 50°C and ramped at 10°C/min until 900°C.

Dodecyl 3-mercaptopropanoate (D3MP):

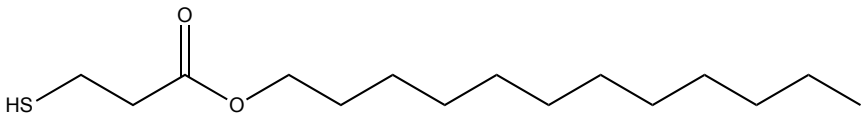

Dodecyl 3-mercaptoproponate was prepared by a modified literature procedure.[65] In a typical synthesis, 1-dodecanol (22.0 g, 0.120 mol, 1.33 equiv.) and 3-mercaptopropionic acid (7.50 mL 0.0900 mol, 1.00 equiv.) were dissolved in 15 mL of toluene with 4 drops of concentrated H_2SO_4. The flask was fitted with a Dean-Stark trap filled with a saturated aqueous KCl. The reagents were heated to reflux for 1 h. The resulting product was washed 2× with 20 mL of brine followed by 20 mL of DI water. The organic layer was dried over $MgSO_4$, and the product purified by vacuum distillation (140°C at 400 mtorr). Yield 14 g (59%). δ_H (400 MHz, $CDCl_3$) 4.10 (t, *J* = 6.72 Hz 2H, -CO_2CH_2-), 2.77 (q, *J* = 8.4 Hz, 2H, -CH_2SH), 2.65 (t, *J* = 6.9 Hz, 2H, -CH_2CO_2-), 1.63 (m, 3H, -$CO_2CH_2CH_2$-, -*SH*), 1.35-1.23 (m, 18H, -CH_2- x9), 0.88 (t, *J* = 7 Hz, 3H, -CH_3). This reaction is now carried out in the Macdonald Laboratory on 750 ml scale.

Copper (I) sulfide nanocrystals with crystal-bound D3MP: Cu_2S was prepared following a similar procedure to the Cu_2S with crystal-bound ligands used previously. In a typical

synthesis, $Cu(acac)_2$ (87.2 mg, 0.333 mmol) was dissolved in 5 mL of D3MP and placed under vacuum for 1 h. The solution was heated to 200°C under nitrogen. At 125°C, the solution turned a transparent yellow color and as the solution heated further it became orange, signifying the formation of the Cu-thiol complex. At 200°C the solution turned black, indicative of particle formation. The solution was reacted for 60 min at 200°C, then was allowed to cool to room temperature under nitrogen. The flask was brought into a glove box where it was filled with 2-propanol. The particles were left to settle out of solution for 16 h. The 2-propanol was then removed leaving a black solid. The particles were washed 2× with 2-propanol then 2× with chloroform in a glove box allowing for each precipitation step to be at least 16 h. The resulting solid was then stored in a glove box as a suspension in $CHCl_3$.

Copper indium sulfide nanocrystals: $CuInS_2$ was prepared following a modified literature procedure.[24] In a typical synthesis, $Cu(acac)_2$ (265.0 mg, 1 mmol) and $In(acac)_3$ (292.0 mg, 1 mmol) were combined in 5.00 mL of D3MP. The reaction was placed under vacuum for 1 h, then heated to 100°C under nitrogen for 10 min to fully dissolve all the precursors. Upon heating to 230°C, the solution changed from a transparent yellow to orange and finally black at 230°C. The temperature was maintained for 1 h. The particles were isolated by adding 2-propanol followed by centrifugation. The supernatant was removed and the resulting solid was suspended in hexanes and precipitated with 2-propanol 2×.

Hydrolysis of D3MP-capped Cu_2S and $CuInS_2$: Dried Cu_2S or $CuInS_2$ was obtained by removing the solvent under vacuum. The particles were then dissolved in a minimal amount of THF, typically 1-2 mL was needed. To the THF/Cu_2S solution, an aqueous 0.1 M KOH solution was added in an amount equal to half the volume of THF used. The solution was stirred in a 50°C water bath for 2 h. The particles were isolated by centrifuging the solution for

5 min at 4400 rpm. The precipitate was washed with ethanol and centrifuged for 5 min at 4400 rpm 2×. The particles were then dispersed in water. The final aqueous solution was then centrifuged for 1 min at 1000 rpm. The precipitate was discarded and the supernatant collected.

Synthesis of 1,1-didodecyldisulfide:

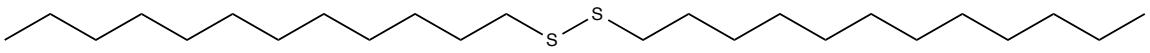

Dodecanethiol (139 µL, 0.582 mmol) was dissolved in dichloromethane (10 mL) with iodine (0.155g, 0.61 mmol, 1.05 equiv.) and triethylamine (120 µL, 0.873 mmol, 1.5 equiv.). The solution was stirred for 2h at room temperature, after which it was diluted with 15 mL of ethyl acetate. The organic layer was washed with water (15 mL) and sat. $Na_2S_2O_8$ (1 mL). The organic layer was collected and the aqueous layer was extracted with ethyl acetate (15 mL). The organic layers were combined and washed with sat. $Na_2S_2O_8$ (3×15 mL), brine (2 × 15 mL), and dried over $MgSO_4$. The solvent was removed *in vacuo* to afford a brown solid. ^{1}H NMR (400 MHz, $CDCl_3$) δ 2.68 (t, *J* = 7.4 Hz, 4H, -C*H*$_2$-S-S-C*H*$_2$-), 1.67 (quint, *J* = 7.28 Hz, 4H, -C*H*$_2$-CH_2-S- ×2), 1.38 (m, 4H, -*CH*$_2$-CH_2CH_2-*S*- ×2), 1.33-1.22 (m, 32H, -CH_2- x16), 0.88 (t, *J* = 7 Hz, 6H, -CH_3 ×2).

Synthesis of didodecyl 3,3'-disulfanediyldipropionate:

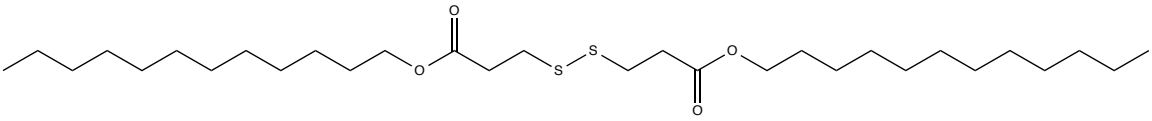

Dodecyl-3-mercaptopropionate (171 µL, 0.582 mmol) was dissolved in dichloromethane (10 mL) with iodine (0.155g, 0.61 mmol, 1.05 equiv.) and triethylamine (120 µL, 0.873 mmol, 1.5 equiv.). The solution was stirred for 2h at room temperature, after which it was diluted with 15 mL of ethyl acetate. The organic layer was washed with water (15 mL) and sat. $Na_2S_2O_8$ (1 mL). The organic layer was collected and the aqueous layer was extracted with ethyl acetate (15 mL). The organic layers were combined and washed with sat. $Na_2S_2O_8$ (3 × 15 mL), brine (2 × 15 mL), and dried over $MgSO_4$. The solvent was removed *in vacuo* and left to dry overnight to afford a crude brown solid. The product was carried on without further purification. ^{1}H NMR (400 MHz, $CDCl_3$) δ 4.09 (t, *J* = 6.6 Hz 4H, -CO_2CH_2- ×2), 2.92 (t, *J* = 7.0 Hz, 4H, -CH_2-S-S ×2), 2.72 (t, *J* = 7.1 Hz, 4H, -CH_2CO_2- ×2), 1.62 (m, 4H, -$CO_2CH_2CH_2$- ×2), 1.46-1.21 (m, 36H, -CH_2- ×18), 0.88 (t, *J* = 6.8 Hz, 6H, -CH_3 ×2).

Synthesis of dodecyl 3-(dodecyldisulfanyl)propanoate:

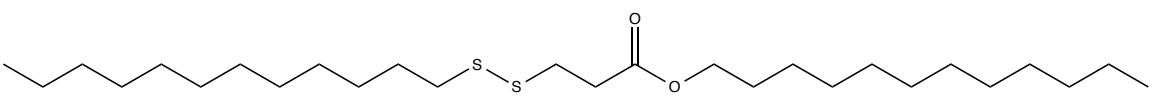

Dodecyl-3-mercaptopropionate (171 μL, 0.582 mmol.) and dodecanethiol (139 μL , 0.582 mmol) was dissolved in dichloromethane (20 mL) with iodine (0.310g, 1.22 mmol, 2.1 equiv.) and triethylamine (240. μL, 1.75 mmol, 3.0 equiv.). The reaction was stirred for 2h at room temperature, after which it was diluted with 15 mL of ethyl acetate. The organic layer was washed with water (15 mL) and sat. $Na_2S_2O_8$ (1 mL). The organic layer was collected and the aqueous layer was extracted with ethyl acetate (15 mL). The organic layers were combined and washed with sat. $Na_2S_2O_8$ (3×15 mL), brine (2 ×15 mL), and dried over $MgSO_4$. Product was concentrated *in vacuo* to give a brown solid. The product was then purified by flash chromatography (column: 1.5 cm x 11 cm, eluent: 100 mL of 1% EtOAc/hexanes, followed by 100 mL of 5 % EtOAc/hexanes) yielding a clear oil. ^{1}H NMR (400 MHz, $CDCl_3$) δ 4.09 (t, J = 6.6 Hz 2H, -CO_2CH_2-), 2.92 (t, J = 7.0 Hz, 2H, -CO_2CH_2-CH_2-S-S), 2.72 (t, J = 7.0 Hz, 2H, -CH_2-S-S), 2.69 (t, J = 7.1 Hz, 4H, -CH_2CO_2-), 1.62 (t, J=6.6 Hz, 2H, -$CO_2CH_2CH_2$-), 1.46-1.21 (m, 36H, -CH_2- ×18), 0.88 (t, J = 6.8 Hz, 6H, -CH_3 ×2).

Additional instrumentation: Transmission electron microscopy images were acquired using a Philips CM 20 or a FEI Techni Osiris operating at 200 keV. Absorbance spectra were obtained using a Jasco V-670 UV-Vis-NIR spectrophotometer. A 400 MHz NMR equipted with a Bruker AV-400 console was also used to acquire ^{1}H NMR spectrum of the organic molecules. Infrared spectroscopy was obtained using a Bruker Tensor FTIR, samples were pressed into a KBr pellet for analysis.

CHAPTER III

DUAL-MODE SURFACE PASSIVATION[II]

3.1 Introduction

In this chapter, I present a new path to control quantum dot (QD) surface chemistry that can lead to a better understanding of nanoscale interfaces and the development of improved photocatalysts. Control of the synthetic methodology leads to QDs that are concomitantly ligated by crystal-bound organics at the surface anion sites and small X-type ligands on the surface cation sites.

QDs are a hybrid material consisting of an inorganic semiconductor core and capping ligands.[18] The capping ligands are vital to the colloidal stability of the QDs, and the interface between the semiconductor core and the ligands has a significant effect on the opto-electronic properties of the QDs through the passivation or creation of surface trap states. Understanding and controlling the interface between the capping ligands and the core facilitates the targeted implementation of QDs in catalytic, biomedical, and electronic applications.[33]

The colloidal methods used to synthesize the QDs are typically performed in organic solvents yielding a layer of native capping ligands with polar head groups and long alkyl chains. These long-chain ligands coordinate to the particle surfaces, decreasing the surface energy of the QD during synthesis, and allowing for control of size, crystalline structure, shape, and colloidal stability.[40, 81] Typically, organic capping ligands passivate the surface atoms by

[II] Part of this chapter has been published previously in Turo, MJ *et al*. "Dual-Mode Crystal-Bound and X-Type Passivation of Quantum Dots" *ChemComm*, **2016**, 52, 12214-12217. Computational work in this chapter was performed by Dr. Xiao Shen.

coordination through either a dative bond (L-type) or an anionic ligand (X-type) to surface metal cations.[30, 33, 82] The long alkyl chains of the organic capping ligands prevent solubility of the particles in polar media and are insulating to charge transfer. This ligand corona needs to be removed, exchanged, or modified for applications in photovoltaics, photocatalysis, and biological systems to impart solubility in different media, improve charge transfer, or allow for functionalization.

Recently, I characterized a novel binding mode for organic capping ligands on QDs that we termed crystal-bound ligands (see Chapter 2), where the thiol ligands occupy a high number coordination sites.[9] This results in increased ligand stability, manifesting as resistance to ligand exchange and photoxidation,[57] and is therefore a promising new ligand type for many applications such as catalysis and biological tags.

Crystal-bound ligands inherently passivate the surface sulfur sites with alkyl groups. Passivation of anion sites has been studied previously with cationic organometallic complexes such as cadmium oleate. The anionic organic tail is lost to maintain charge balance when small, X-type, anionic ligands are introduced to passivate the surface metal sites of the quantum dot.[83] In contrast, passivation of the anion sites with crystal-bound ligands should allow for simultaneous passivation of the surface metal sites with small X-type anionic ligands[84] without the removal of the alkyl chains, but has yet to be experimentally demonstrated. Similarly, metal chalcogenide-thiol clusters show bridging thiols,[85] which are reminiscent of the high coordination number of the crystal-bound binding mode. Due to the shape of the clusters, exposed cations only occur at the apices and can be passivated by other ligands. In quasi-spherical QD, we expect a greater diversity in surfaces and a much greater mixture of cation and anion exposure.

It is not known how this dual-mode passivation, and in particular, the crystal-bound component operates to modify the opto-electronic properties of QDs. In this chapter, I demonstrate the role that the X-type passivation of QDs in this dual-mode passivation can play on the optical properties. Furthermore, I show the potential for improving the catalytic function of QDs through this controlled dual-mode coordination by comparing them to QDs with a similar surface-bound capping mode in a model photocatalytic reaction.

3.2 Results and discussion

Crystal-bound ligands occur on QDs when a primary thiol is used as the sulfur source in the synthesis of a metal sulfide. The metal-thiolate complex decomposes producing the nanocrystal.[19] At lower temperatures, the final layer of organics is not thermally cleaved.[21] Previously, we demonstrated crystal-bound ligands on Cu_2S and $CuInS_2$ nanocrystals.[9] Here we extended this work to the synthesis of a ZnS shell around CdSe with crystal-bound ligands. CdSe seeds were synthesized following a literature procedure.[86] The ZnS shell with crystal-bound dodecanethiol (DDT) was then synthesized using zinc acetate and dodecanethiol in trioctylamine and oleic acid, in the presence of the CdSe cores. The shelling procedure increased the size of the QDs from 3.0 ± 0.2 nm n = 150 to 3.8 ± 0.3 nm n = 129 indicating the growth of the shell. When the same reaction was run in the absence of zinc acetate the CdSe cores ripened to 3.2 ± 0.5 nm n = 137; this is evidence that the growth seen from shelling procedure is from shell growth and not ripening (Figure 3.1). Interestingly, the CdSe@ZnS QDs were not fluorescent; I attribute this to incomplete shelling of the nanocrystal and the presence of thiols, which quench the fluorescence of CdSe cores.

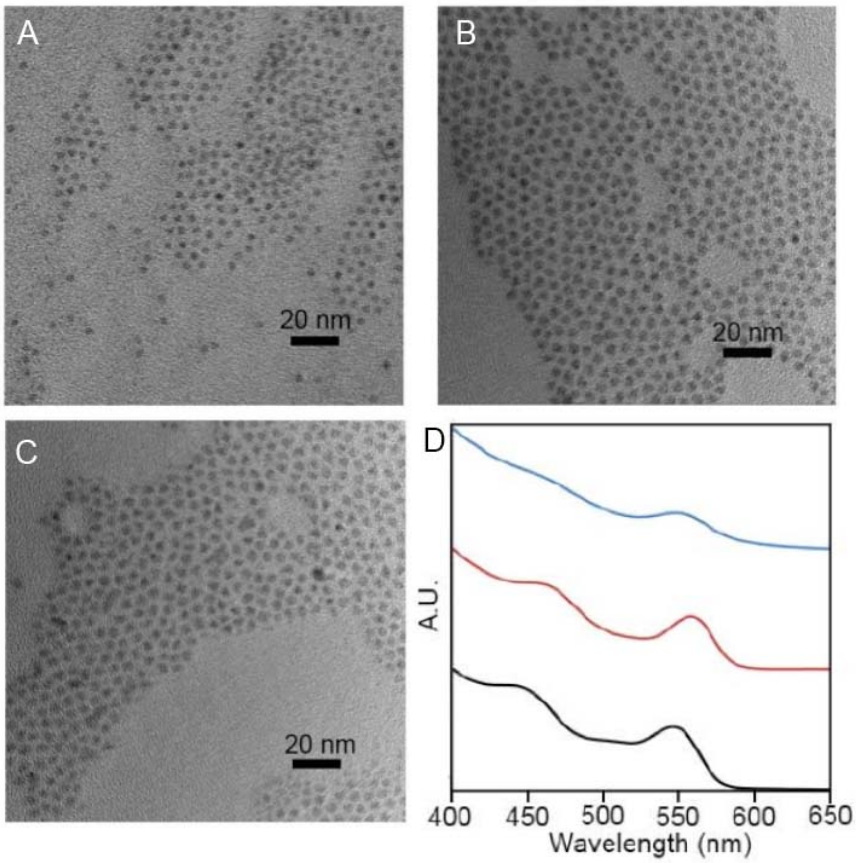

Figure 3.1 TEM of CdSe seeds (A) CdSe@ZnS core/shells with crystal-bound DDT no initial ZnS shell (B) and CdSe after the shelling procedure with no Zn present (C). Absorbance spectra of CdSe seeds (black), CdSe@ZnS core/shells with crystal-bound DDT no initial (red), and CdSe after the shelling procedure with no Zn present (blue)(D).

To obtain fluorescent particles an initial ZnS layer with surface-bound ligands was grown around a different batch of CdSe seeds (d = 2.8 ± 0.2 nm, n = 125, QY=26%). ZnS shell with surface bound ligands was grown around the seeds following a literature procedure[87] to ensure a complete shelling of the QDs (d = 3.2 ± 0.2 nm, n = 127, QY = 50%). To synthesize the secondary shell with crystal-bound ligands, the premade core/shells QDs were injected with dodecanethiol (DDT) into a solution of $Zn(OAc)_2$ in oleic acid and trioctylamine at 150°C for 1 h.[22] The resulting QDs had increased in size to 3.9 ± 0.3 nm n = 133 and the quantum yield increased to 80% (Figure 3.2). We considered the possibility that the differences in behavior

(*vide infra*) are a result of differing surface densities of ligands resulting from the differing synthetic routes. However, the ligand density was determined by ^{1}H NMR and was found to be similar for the crystal-bound DDT QDs (3.9 ligands/nm^2) and the surface-bound QDs that had undergone a room temperature ligand exchange to DDT (3.6 ligands/nm^2). The peak of the S2*p* XPS spectra of QDs with crystal-bound thiols is shifted towards a lower binding energy than QDs with surface-bound thiols (Figure 3.3). The decreased high binding energy component for QDs with crystal-bound thiols is consistent with a lack of low binding-energy surface thiolates, as we reported previously for crystal-bound ligands on Cu_2S. [9]

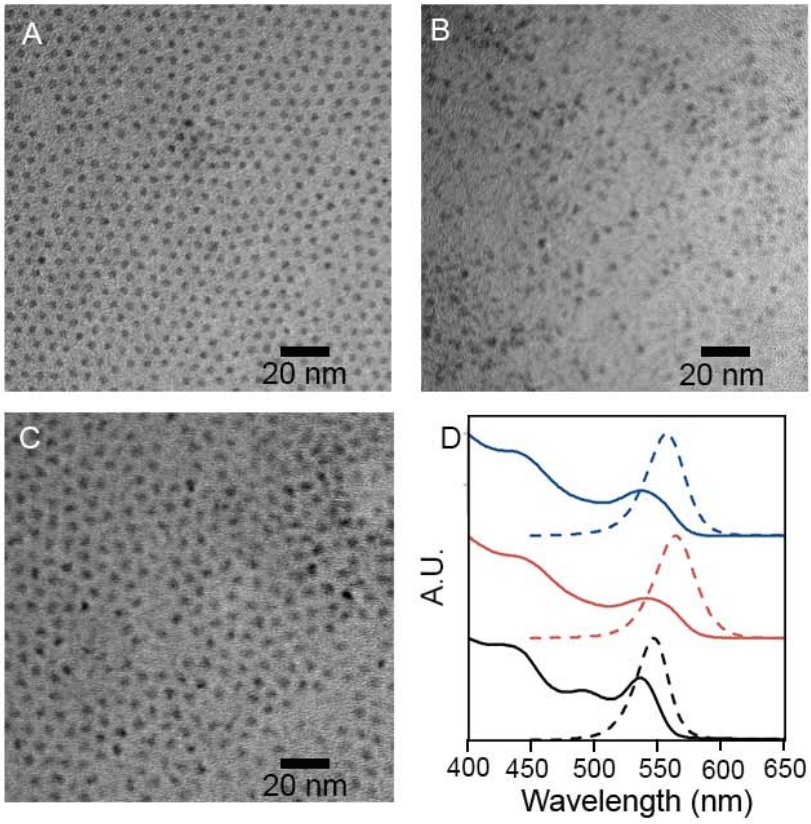

Figure 3.2 TEM of CdSe seeds (A) CdSe@ZnS core/shells with native ligands (B) and crystal-bound DDT (C). Absorbance (solid) and PL (dashed) spectra of CdSe seeds (black), CdSe@ZnS with native ligands (red), and crystal-bound DDT (blue)(D).

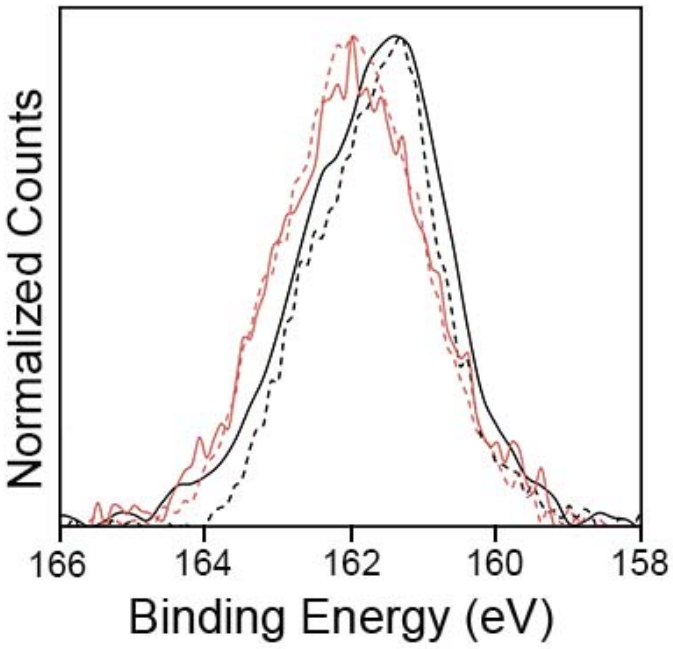

Figure 3.3: S2*p* XPS of CdSe@ZnS with crystal-bound (black spectra) and surface-bound (red spectra) thiols. Both DDT (solid line) and MPA (dashed) capped particles are shown.[8] Overlapping signal from the Se3*p* in this region prevented detailed fittings of the spectra.

IR spectroscopy of the QDs capped with crystal-bound DDT shows vibrational modes at 1560 cm^{-1} and 1379 cm^{-1}, which can be assigned to X-type coordination of acetate to the surface Zn sites (Figure 3.4A).[88] While oleic acid is also part of the synthesis, the absence of signals due to the double bond by IR and NMR suggest that acetate causes the observed C-O stretching modes rather than oleate (Figure 3.4A).

^{1}H NMR was used to show increased stability of the organic chain for QDs with crystal-bound ligands over QDs with surface-bound ligands when undergoing ligand exchange at the cation sites. The as-synthesized QDs with crystal-bound and surface-bound DDT were suspended in THF and exposed to aqueous base to facilitate a ligand exchange at the cation sites to the X-type ligand, OH^{-}.[89] No additional free thiol ligands were added. Dipolar effects of the metal atoms in and the slow tumbling of the QD quench the signals of protons close to the

QD,[36] therefore an increase in the -CH_2- peak is evidence of an increase in the free ligand concentration as thiol ligands are removed from the QD surfaces. (Figure 3.4B). Such an increase in free ligand was observed for the particles capped with surface-bound DDT, indicating the removal of X-type dodecanethiolate by OH^-. No change in solubility was observed for the crystal-bound case, indicating the crystal-bound ligands are more robustly attached to the particle surfaces.

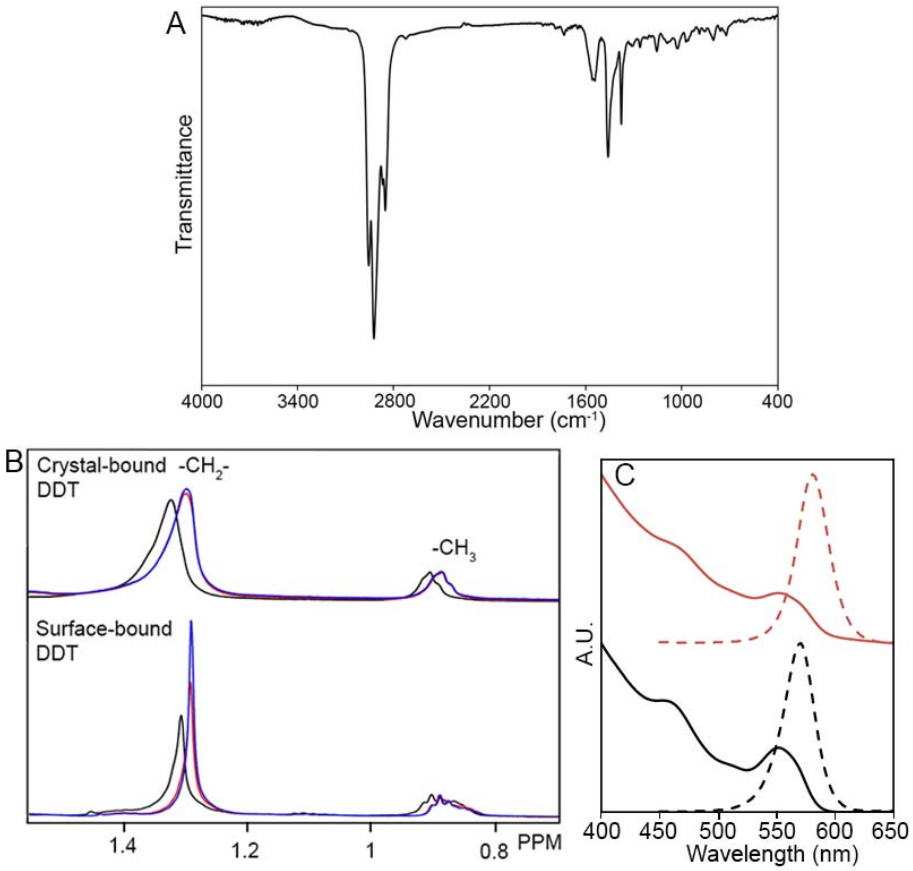

Figure 3.4: IR of CdSe@ZnS with crystal-bound DDT (A) ^{1}H NMR of crystal-bound (top) and surface-bound (bottom) DDT capped CdSe@ZnS in D_8-THF, initial (black), after the addition of base (red), and after 10 sec. of sonication (blue) (B). Absorbance and PL of CdSe@ZnS capped with crystal-bound DDT and before (red) and after (black) base treatment (C).

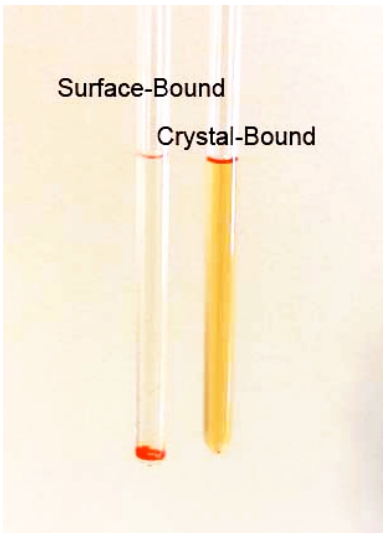

Figure 3.5: Picture of the NMR tubes for the experiment described in Figure 3.4A 1 h after the experiment. The left NMR tube contains the surface-bound DDT capped nanocrystals and the right NMR tube contains the crystal-bound DDT capped nanocrystals. The nanocrystals in the surface-bound sample lose colloidal stability because the ligands are removed in the base treatment. The crystal-bound sample remains colloidally stable in D_8-THF because the long chain thiol ligands are not removed by base treatment.

Despite the ^{1}H NMR evidence that CdSe@ZnS QDs capped with crystal-bound DDT did not undergo loss of the organic ligands, the QDs underwent a near immediate quench and red-shift in the fluorescence upon exposure to base (Figure 3.4C). This observation hinted that the crystal-bound ligand binding mode provides new opto-electronic properties; however, further study of this phenomenon and comparison to the surface-bound ligand binding mode became challenging because the QDs with surface bound thiols quickly precipitated from solution after the base exposure. As a result, we changed to our system to study the effects of our surface chemistry in aqueous phase catalysis, compared to traditional surface-bound ligands.

To allow for phase transfer of the crystal-bound capped CdSe@ZnS into an aqueous environment, dodecyl-3-mercaptopropionate (D3MP) was used in place of DDT in the

synthesis.[9] D3MP replaces DDT in the crystal-bound shell synthesis yielding similar particles as the DDT sample, where the particle size increased to 3.9 ± 0.3 nm n = 121 as did the quantum yield to 83% (Figure 3.6). A base hydrolysis was used to cleave the ester rendering the QDs water soluble (Figure 3.7). Evidence of hydrolysis is seen in the changing IR spectra with the shifting of the C=O peak from 1700 cm^{-1} to the stretching mode of the free carboxylate at 1550 cm^{-1}, similar to the Cu_2S with D3MP capped particles in Chapter 2. After the hydrolysis, the particles maintained their size and shape (3.9 ± 0.3 nm n = 146). The photoluminescence (PL) was shifted to lower energies and quenched to 6% (Figure 3.6).

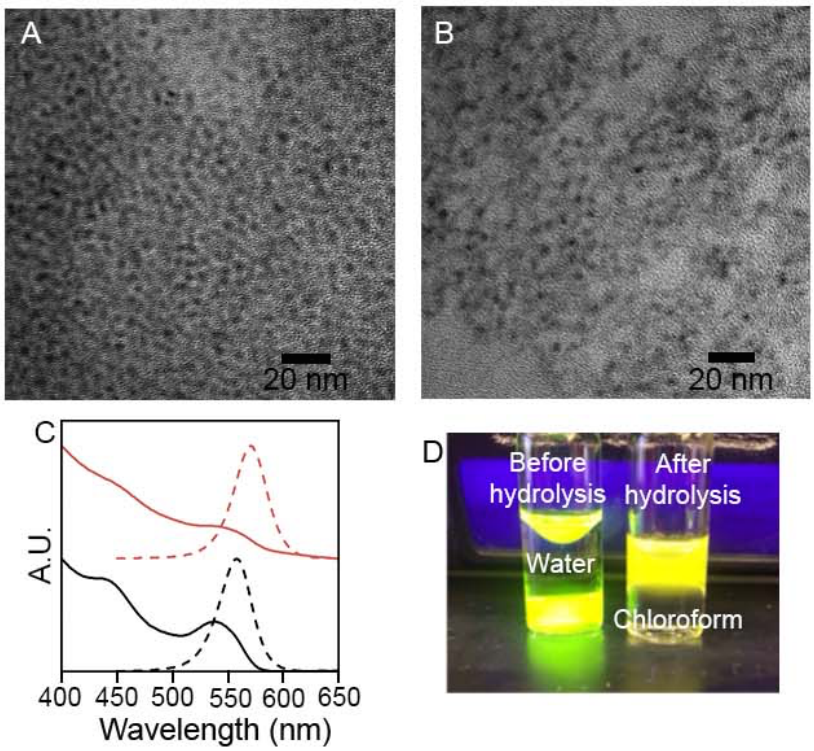

Figure 3.6: TEM of CdSe@ZnS with crystal-bound D3MP before (A) and after (B) hydrolysis. Absorbance and PL spectra of CdSe@ZnS with crystal-bound D3MP (black) and MPA (red) (C). D3MP capped CdSe@ZnS before and after hydrolysis (D)

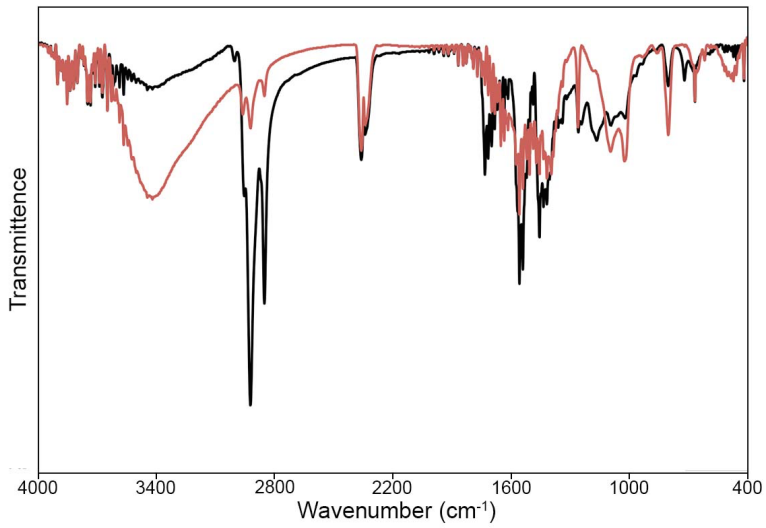

Figure 3.7: Infrared spectra of CdSe@ZnS with crystal-bound D3MP before (black) and after (red) hydrolysis. Evidence of the hydrolysis is observed by the loss of the ester C=O stretching mode at 1700 cm^{-1} after the hydrolysis.

When the size of the CdSe core was changed, so too was the magnitude of the fluorescence red shift. Larger CdSe cores resulted in a smaller shift (4.06 nm, -0.025 eV) and smaller cores resulted in a greater shift (2.65 nm, -0.068 eV) (Figure 3.8). In contrast, when native ligands on the CdSe@ZnS were exchanged to give surface-bound mercaptopropionic acid (MPA), no significant shift was observed in the fluorescence spectrum (Supporting Information). Two non-mutually-exclusive hypotheses emerged regarding atomistic origin of the red shift in the QD PL spectrum for crystal-bound thiols upon hydrolysis. The first hypothesis is that the addition of base alters the coordination of the surface Zn from acetate to hydroxide, as small anions are known to charge balance the surface of QDs.[84] This change in surface cation chemistry alters the electron wavefunction since the conduction band is dominated by the orbitals of the cations.[90] The second possibility is that the hydrolysis of the ester causes a shift in the band gap. Crystal-bound thiols are part of the anion sublattice of the QD, which dominates the orbital make-up of the valence band in CdSe and ZnS.[90] As a result,

the hole wavefunction may be perturbed by energetic subtleties between ester and carboxylate groups on the crystal-bound ligands.[91]

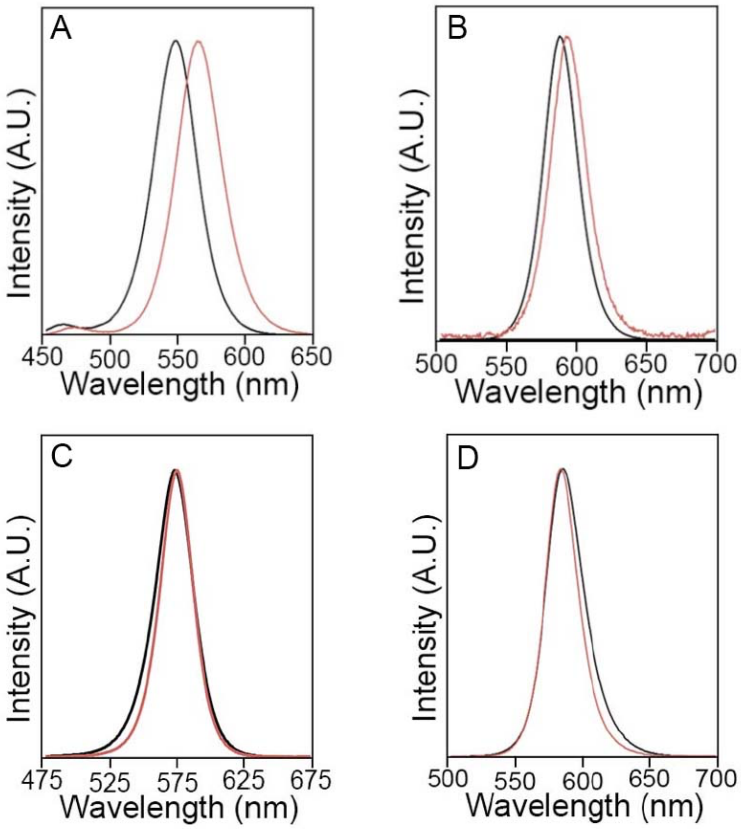

Figure 3.8: (A) Fluorescence spectra of 2.65 nm CdSe@ZnS with crystal-bound D3MP, before (black) and after (red) hydrolysis. (B)Fluorescence spectra of 4.06 nm CdSe@ZnS with crystal-bound D3MP, before (black) and after (red) hydrolysis. (C) Fluorescence spectra of 3.04 nm CdSe@ZnS with surface-bound native ligands (black) and after ligand exchange with MPA (red). (D) Fluorescence spectra of 4.06 nm CdSe@ZnS with surface-bound native ligands (black) and after ligand exchange with MPA (red).

Density functional theory (DFT) was used to investigate the change in the QD band gap for different surface terminations providing an atomistic origin of the red shift upon hydrolysis. The calculations were performed for slab models of the (110) surface, which is the lowest energy surface of zinc blende ZnS and likely to dominate faceting of the cubic crystal-structured QDs.[92] HR TEM of D3MP capped core-shell QDs before and after hydrolysis showed lattice

fringing consistent with CdSe throughout, indicating ZnS is strained to match the CdSe lattice. Therefore, the calculations used CdSe lattice parameters for CdSe for the strained ZnS shell (Figure 3.9).

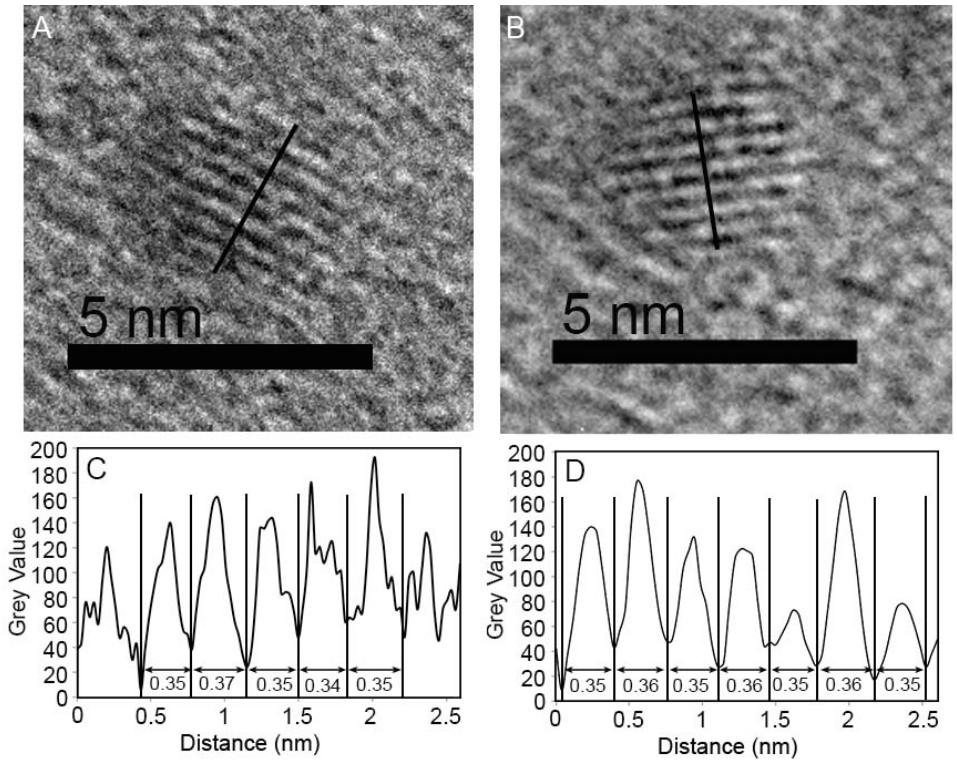

Figure 3.9: High-resolution TEM images of CdSe@ZnS with crystal-bound D3MP before (A) and after (B) hydrolysis. (C) and (D) are plots of the intensity profiles along the marked lines in the TEM images. Distances between lattice planes are noted. The observed d-spacing of 0.35 nm is consistent with the d-spacing of the (111) of zinc blende CdSe. The d-spacing of (111) zinc blende ZnS is 0.30 nm. From this we infer that the CdSe core dominates the lattice parameters and the ZnS shell is strained.

Two sets of slab models were constructed to simulate quantum confinement of two QD sizes. The thicker slab model consists of 11 layers of CdSe and 2 layers of ZnS (one on each side), emulating the larger nanoparticles. The thinner slab model consists of 5 layers of CdSe and 2 layers of ZnS, emulating the smaller QDs. The confinement energies ($E_{confinement}$) from the models are shown in Table I, along with the experimental data showing that the two are within reasonable agreement. Details of calculations are in Supporting Information.

Figure 3.10 A-C shows the three types of surface terminations of the CdSe@ZnS QDs considered in the calculations. Model A represents the state of QD surface before hydrolysis, when the Zn site is terminated by acetate. Models B and C represent two possible models of the surface after hydrolysis. In model B, hydrolysis only happens at the ester ligand leaving crystal-bound MPA, while in Model C the hydrolysis occurs on both the ester and the Zn site to give Zn-OH cation termination.

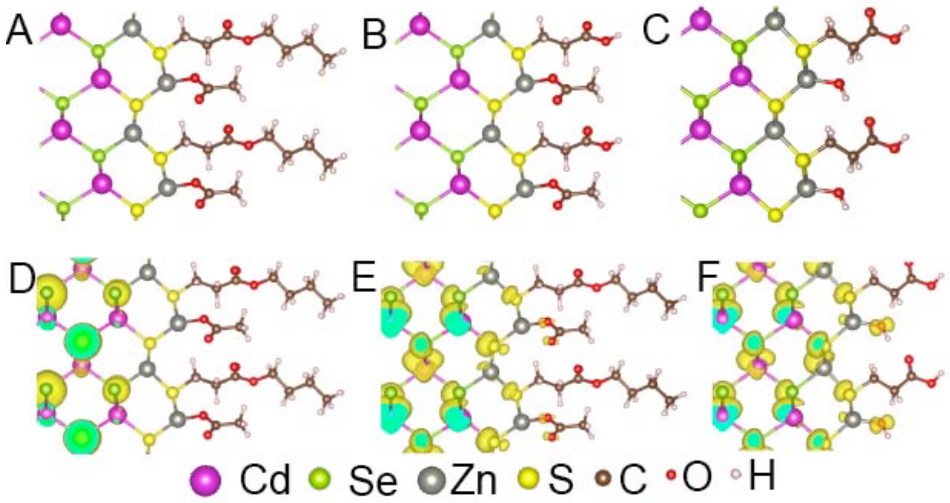

Figure 3.10: Models of the CdSe@ZnS core shell surface used in calculations (A-C). (D) The hole wavefunction (VBM) in Model A for thick slab of CdSe/ZnS core shell. (E) The electron wavefunction (CBM). (F) The electron wavefunction (CBM) of Model C.

Table 3.1 Experimental and computational redshifts

Experiment			
	$E_{confinement}$	E_{shift}	
Large QDs (4.06 nm)	0.372 eV	-0.025 eV	
Medium QDs (3.04 nm)	0.432 eV	-0.036 eV	
Small QDs (2.65 nm)	0.523 eV	-0.068 eV	
DFT (Figure 3.10)			
	Model A	Model B	Model C
	$E_{confinement}$	E_{shift}	E_{shift}
Thick Slab	0.259 eV	0.013 eV	-0.042 eV
Thin Slab	0.616 eV	0.003 eV	-0.164 eV

The calculated shift (E_{shift}) in the band gap of the CdSe@ZnS QDs upon hydrolysis of the dual-mode crystal-bound/surface-bound capping ligands are shown in Table I. The hydrolysis of D3MP ligand in Model B introduces very small increase in the band gap of 13 meV for the thicker slab and 3 meV for the thin slab. Therefore, the large experimentally observed redshift cannot be explained by hydrolysis of the D3MP ligands alone. Instead, additional surface contributions must be considered. Combining the hydrolysis of D3MP ligand with a change of Zn termination from Zn-acetate to Zn-OH results in a reduction of the band gaps: -42 meV for the thicker slab and -164 meV for the thinner slab. Both results are of the same order of magnitude as the experimental data (-25 to -68 meV for large and small QDs, respectively). The small discrepancies between the theoretical and experimental redshifts are likely due to the use of slab models that are confined in 1-dimension to simulate the confinement energy of nanoparticles that are confined in 3-dimensions, an oversimplification of the exposed ZnS crystallographic surfaces, and tensile strain on the ZnS shell.

The DFT calculations show that the band gap in the dual mode capping is altered mostly by the change in Zn termination from Zn-acetate to Zn-OH and not by the hydrolysis of the ester of crystal-bound D3MP. The calculations show strong confinement of the hole wavefunction by the ZnS layer (Figure 3.10D), but the electron wavefunction penetrates the ZnS shell and contains contributions from the X-type ligand on the Zn site (Figure 3.10E). Therefore, the conduction band minimum (CBM) is sensitive to the change of the Zn site passivation. Indeed, after the change in Zn passivation from acetate to hydroxide there is an increased contribution in the electron wavefunction from the hydroxide (Figures 3.10E and 3.10F). The greater extension of the electron wavefunction in the Zn-OH surface indicates that the quantum confinement effect on electron is weaker than in the Zn-acetate surface and thus

the band gap is smaller, consistent with the observed redshift after hydrolysis. It should be noted that although one would expect good confinement of electrons in CdSe@ZnS core-shell structure[93] from the bulk band alignment, the ZnS layer is highly strained on CdSe,[94] which alters the band positions in ZnS by lowering the conduction band.

Red shifts in the band gap of QDs have been associated with the extension of the exciton wavefunction into organo-sulfur ligands such as dithiocarbamates and thiols.[91] However, our calculations suggest that for the crystal-bound thiols, the organic ligands bound to the anion sublattice are electronically benign and therefore solely provide colloidal stability. It is the change in inorganic surface cation ligand that causes the modification of the band gap. These calculations explain our initial observation that QDs with crystal-bound DDT undergo shifts in the fluorescence spectrum upon exposure to base without loss of the organic ligands (Figure 3.6).

The changes in fluorescence and colloidal stability of the QDs with surface-bound DDT after exposure to base suggests that hydroxide removes surface-bound DDT and other surface-bound ligands to expose cation sites and change their termination to Zn-OH. The removal of the ligands harms the colloidal stability in organic solvents. In contrast, the organic component in the crystal-bound surface allows for organic-inorganic capping. The organic ligand corona is not disturbed by the hydroxide treatment changing the cation termination to Zn-OH and the colloidal stability is maintained.

This dual-mode ligand structure has important implications for QDs used in applications where charge transport and transfer is crucial, such as solution-based water reduction catalysts that rely on QD photosensitizers.[95] The organic crystal-bound ligands provide solubility of the QDs in desired media and enhanced ligand stability under light exposure.[9] The exposed cation

sites can be used to modify the electronic properties as evident by the increased leakage of the electron wavefunction to the surface upon cation OH^- termination in the DFT calculations (Figure 3.10F). While the DFT calculations do not show the production of mid-gap states upon surface hydroxylation, the increased contribution of the surface atoms to the wavefunction causes the exciton to be more prone to collisional recombination. In addition to the observed fluorescence quench, the QDs are correspondingly more efficient at electron transfer to solution species, aiding in photocatalysis.

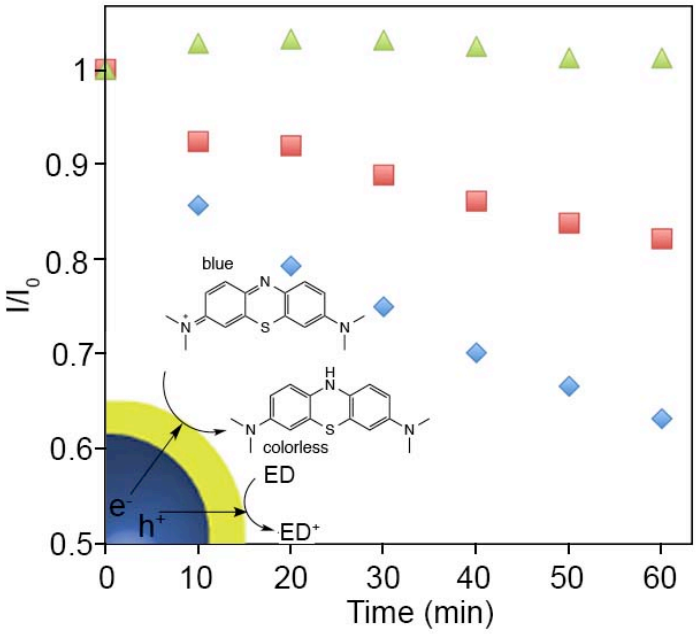

Figure 3.11: The change in absorbance of methylene blue at 666 nm with CdSe@ZnS photocatalysts, crystal-bound ligands (blue), surface-bound ligand (red) and no QDs (green). Insert is the mechanism of the photocatalysis.

As a demonstration of the improved charge transfer possible for this dual mode crystal-bound and X-type ligand QD capping over more standard surface-bound ligand systems, the photodegradation of methylene blue in aqueous solution was perfomed.[96] The change in the absorbance of the dye was monitored in the presence of CdSe@ZnS nanocrystals capped with traditional surface-bound MPA and CdSe@ZnS nanocrystals capped with crystal-bound MPA

and -OH anion terminating (Figure 3.12). After 1 h of irradiation by visible light, the hybrid ligand capped QDs facilitated a 40% degradation of the methylene blue, whereas the QDs with traditional surface-bound organic passivation provided only 17% degradation. The improved photocatalytic degradation of methylene blue shows the dual passivation results in improved photoinduced charge transfer to solution based species. Throughout the photocatalytic study, no degradation on the QDs was observed; as there was no decrease in absorption above 550 nm, where the primaryly absorption is from the QDs (Figure 3.13)

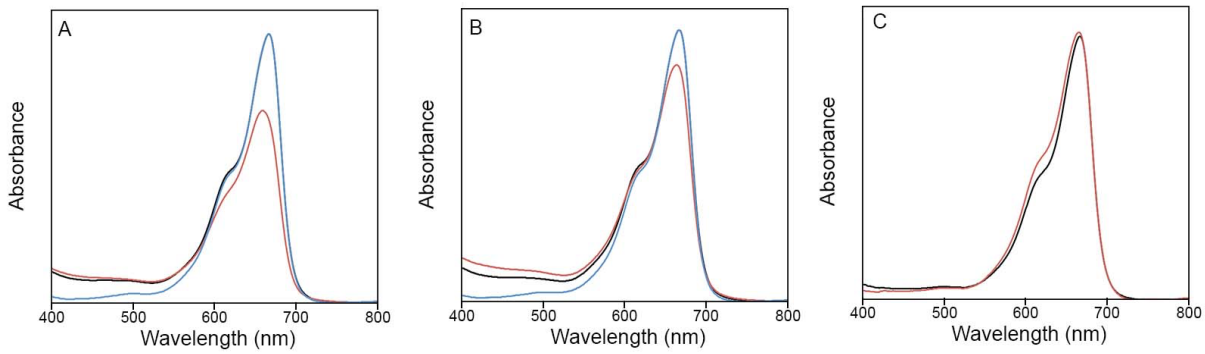

Figure 3.12: (A) Absorbance spectra of methylene blue (blue), CdSe@ZnS with crystal-bound MPA and methylene blue (black) and CdSe@ZnS with crystal-bound MPA and methylene blue after 1 h of exposure to blue light (red). (B) Absorbance spectra of methylene blue (blue), CdSe@ZnS with surface-bound MPA and methylene blue (black) and CdSe@ZnS with surface-bound MPA and methylene blue after 1 h of exposure to blue light (red). (C) Absorbance spectra of methylene blue (black) and methylene blue after 1 h exposure to blue light (red). Absorbance at wavelengths below 550 nm is attributed to the QDs. No change in the absorbance in this region is observed during the catalysis, suggesting no degradation of the QDs.

3.3 Conclusion

In this dual mode capping system, the organic capping component controls the colloidal stability while the inorganic component influences the optical properties. Crystal-bound thiols, which terminate the anion sites, are not displaced in base exposure and have been shown to be resistant to removal. Photooxidation of the thiol ligands to disulfides, resulting in a loss of

colloidal stability is a well-described problem in biological and photocatalytic applications.[57] The use of the ester containing D3MP as a thiol ligand provides a route to modify the solubility of particles in polar and nonpolar media as well as provides a chemical handle for later surface functionalization. In essence, the organic ligand corona is robust and can be tailored to give solubility in water or organic solvents. Concomitantly, the inorganic component modifies the surface cation chemistry and influences the electronic properties in CdSe@ZnS quantum dots, improving catalytic activity. Improved QD based applications can be obtained by controlling the organic and inorganic capping ligands in this system. The stability afforded by crystal-bound ligands and the improved charge transfer using inorganic ligands are desirable and should be exploited for improved catalytic systems.

3.4 Experimental methods

Materials: Cadmium myristate and dodecyl-3-mercaptopropinoate (D3MP) were prepared following literature procedures (details below). Selenium dioxide (99.8%), 1,2-hexadecanediol (90%), 1-octadecene (ODE, 90%), oleic acid (OA, 90%), oleylamine (OLAM, 70%), trioctylphosphine (TOP, 90%), zinc diethyldithiocarbamate ($Zn(ddtc)_2$, 97%), dodecanethiol (DDT, >98%), trioctylamine (TOA, 98%), mercaptopropionic acid (MPA, >99%) tetramethylammonium hydroxide pentahydrate (TMAH, >97%), myristic acid (≥98%),1-dodecanol (98%), and potassium hydroxide (85%) were obtained from Sigma Aldrich. Zinc acetate dihydrate ($Zn(OAc)_2 \bullet 2H_2O$), 97%) was obtained from Alfa Aesar. Cadmium nitrate tetrahydrate (98%) was obtained from Strem. All chemicals were used as obtained and standard Schlenk techniques were used during the syntheses.

Cadmium Selenide Synthesis: CdSe was prepared following a modified literature procedure.[86] Briefly, Cd(myristate)$_2$ (0.5 mmol) was combined with SeO_2 (0.5 mmol) and 1,2-hexadecanediol (0.5 mmol) in 10 mL of ODE. The solution was purged by vacuum and the vessel was filled with N_2. The flask was then heated quickly to 240°C and reacted for 1 min at that temperature. The solution was cooled to RT and particles were isolated. First by precipitation by the addition of acetone and centrifugation at 8700 rpm for 5 min. The particles were then washed 3x using chloroform and acetone, then stored in the dark dispersed in chloroform.

*Zinc Sulfide Shells with Surface-Bound Ligands:*The ZnS shell was prepared following a modified literature procedure.[87] The concentration of the CdSe stock solution was determined by the absorbance at the first exciton peak.[97] 500 nmol of CdSe seeds were combined with Zn(ddtc)$_2$ (118 mg, enough for 2 monolayers (ML), calculated following a literature procedure[98]), OLAM (3 mL), TOP (3 mL), and ODE (10 mL). The solution was placed under vacuum for 1 h at room temperature to remove the $CHCl_3$. The solution was then heated at a rate of 80°C/h to 120°C and reacted for 1 h at that temperature. The particles were then cooled to RT and precipitated by the addition of acetone and centrifuged at 8700 rpm for 5 min. The particles were washed with acetone and chloroform until no unbound ligands were observed by ^{1}H NMR, typically 4×. Particles were stored in the dark in $CHCl_3$.

Surface-Bound Thiol Ligand Exchange: To exchange DDT onto the surface of CdSe@ZnS, 100 mg of TMAH•5H_2O was dissolved in 1 mL of $CHCl_3$ with 100 µL of DDT. The solution was stirred for 15 min and a phase separation was observed. The bottom $CHCl_3$ layer was collected, added to a $CHCl_3$ solution containing 50 nmol of CdSe@ZnS and stirred for 1 h at room temperature in the dark. The particles were then precipitated by the addition of

ethanol and washed with chloroform and ethanol until no unbound ligands were observed by ^{1}H NMR, typically 5×. MPA exchange was similar except that the particles were washed using only ethanol, then dispersed in a pH 7 phosphate buffer.

Zinc Sulfide Shells with Crystal-Bound Ligands: The concentration of the CdSe@ZnS with surface-bound ligands seeds stock solution was determined by the absorbance at the first exciton peak.[97] A $CHCl_3$ solution containing 50 nmol of CdSe@ZnS was combined with 1 mL of TOA and placed under vacuum for 1 h to remove the $CHCl_3$. In a separate flask, $Zn(OAc)_2 \bullet 2H_2O$ (15 mg, enough for 2 ML of ZnS), 2.5 mL of OA, and 2.5 mL TOA was combined and placed under vacuum at 105°C for 1 h to remove H_2O. The Zn containing solution was then heated to 150°C under N_2 at 150°C. CdSe@ZnS solution and 100 μL of DDT were injected simultaneously into the hot Zn containing solution. The resulting solution was reacted at 150°C for 1 h. Finally, the reaction was cooled to RT and the particles were precipitated by the addition of acetone and centrifuged at 8700 rpm for 5 min. The particles were then washed with acetone and chloroform until no unbound ligands were observed by ^{1}H NMR, typically 4x. Particles were stored in the dark in $CHCl_3$. For D3MP capped particles, DDT was replaced with an equimolar amount of D3MP.

Base Treatment of Dodecanethiol capped CdSe@ZnS: A $CHCl_3$ solution containing 10 nmol of CdSe@ZnS with DDT capping ligands was dissolved in 2 mL of THF and treated with 100 μL of 2 M KOH in H_2O followed by 10 s of sonication. The particles were obtained by centrifuging at 4400 rpm for 5 min; no additional solvent was need for surface-bound DDT while crystal-bound DDT needed methanol to precipitate. The particles were then washed 2× with ethanol to remove any excess base.

Hydrolysis of Dodecyl-3-Mercaptopropionate Capped CdSe@ZnS: 10 nmol of D3MP capped CdSe@ZnS was dissolved in 2 mL of THF and treated with 100 μL of 2 M KOH in H_2O followed by 10 min of sonication. To precipitate the particles, hexanes was added to the solution and centrifuged at 4400 rpm for 5 min. The particles were then washed 2× with ethanol then dissolved in a pH 7 phosphate buffer.

Photocatalytic Degradation of Methylene Blue: A CdSe@ZnS solution was prepared by dissolving the water soluble QDs in a pH 7 phosphate buffer with the first excitation peak having an absorbance of 0.1. In a quartz cuvette sealed with a septum, 0.500 mL of CdSe@ZnS solution, 0.100 mL of 0.177 mM methylene blue solution in deionized water (Millipore, 18 mΩ), and 1.00 mL of pH 7 buffer was combined and bubbled with N_2 for 30 min. After the N_2 purge, 0.500 mL of ethanol that had been purged separately by freeze-pump-thaw was added to the solution. The solution was then exposed to light from a 13 W blue-colored compact fluorescent light (FEIT electric BPESL13T/B). The absorbance of methylene blue was monitored at 666 nm, every 10 min for 1 h. For the control experiment without QDs, the 0.500 mL of CdSe@ZnS solution was replaced with 0.500 mL of buffer solution. The experiments were performed in triplicate and the average of the runs reported.

Synthesis of Dodecyl-3-Mercaptopropionate: Dodecyl-3-mercaptopropionate was prepared following the same procedure as in Chapter 2 see page 46 for details.[9]

Synthesis of Cadmium Myristate: Cadmium myristate was prepared following a literature procedure.[86] Briefly, two solutions were prepared, one of 1.54 g of cadmium nitrate tetrahydrate (5 mmol) in 50 mL of ethanol and the other of 3.42 g of myristic acid (15 mmol) and 0.60 g of sodium hydroxide (15 mmol) in 500 mL of ethanol. The solution of cadmium nitrate was then added drop wise to the sodium myristate solution. The resulting precipitate was

filtered and washed with methanol 3×. The product was then dried over night at 60°C under vacuum.

Quantum yield: Quantum yields were determined by comparison of the emission of the nanocrystals to a standard of Rhodamine B in methanol (excitation at 348 nm gives a quantum yield, ϕ_{std} = 70%).[99] The concentrations of the nanoparticles were adjusted so that the absorbance at 348 nm was 0.1 abs for all samples to assure reabsorption is not a problem. To calculate the photoluminescence quantum yield of the sample (ϕ_x), the following equation was used:

$$\phi_x = \frac{F_x a_{std} n_x^2}{F_{std} a_x n_{std}^2} \phi_{std} \quad (3.1)$$

Where F is the integrated intensity of the fluorescence, a is the absorbance at the excitation wavelength (348 nm), and n is the refractive index of solvent.

Density Functional Theory Calculations: DFT calculations were performed using the PBE version of the exchange-correlation functional,[100] PAW potentials,[101] and a plane-wave basis as implemented in the VASP code.[102] The plane-wave energy cutoff was set at 353 eV and a 5x3x1 k-point sampling was used. In all the slab models, the ligands from the periodic images of the slabs were separated by at least 19 Å, ensuring no artificial interactions between the images.

Determination of ligand density: Using QDs with a known surface area determined by sizing the particles using TEM images and assuming a spherical particle. A NMR tube was filled with 700 μL of a QD stock solution in $CDCl_3$ with a known concentration determined by UV-Vis and 10 μL of a 0.12 mM solution of 1,2-dibromoethane. The number of bound ligands

was determined by the 4:3 ratio of the integration of the 1,2-dibromoethane at 3.65 ppm to the terminal -CH_3 at 0.88 ppm. The number of ligands/particles was then determined by dividing the number of bound ligands to the number of particles in the sample. The ligand density is obtained by comparing the number of ligands/particle to the total surface area. ^{1}H NMR spectra shown below for CdSe@ZnS with crystal-bound DDT (Figure 3.13) and surface bound DDT (Figure 3.14).

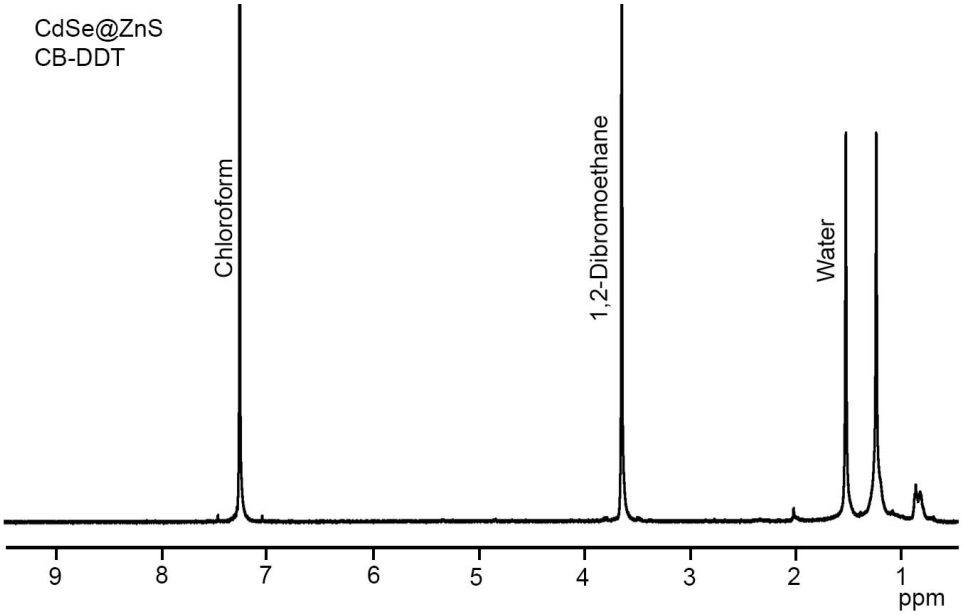

Figure 3.13: ^{1}H NMR of CdSe@ZnS with crystal-bound DDT. 1,2-dibromoethane was added as an internal standard, ligand density was found to be 3.9 ligands/nm^2 for crystal-bound DDT. There are there are no resonances for the protons associated with the double bond of oleic acid despite being a reagent during the synthesis, indicating no oleic acid passivation.

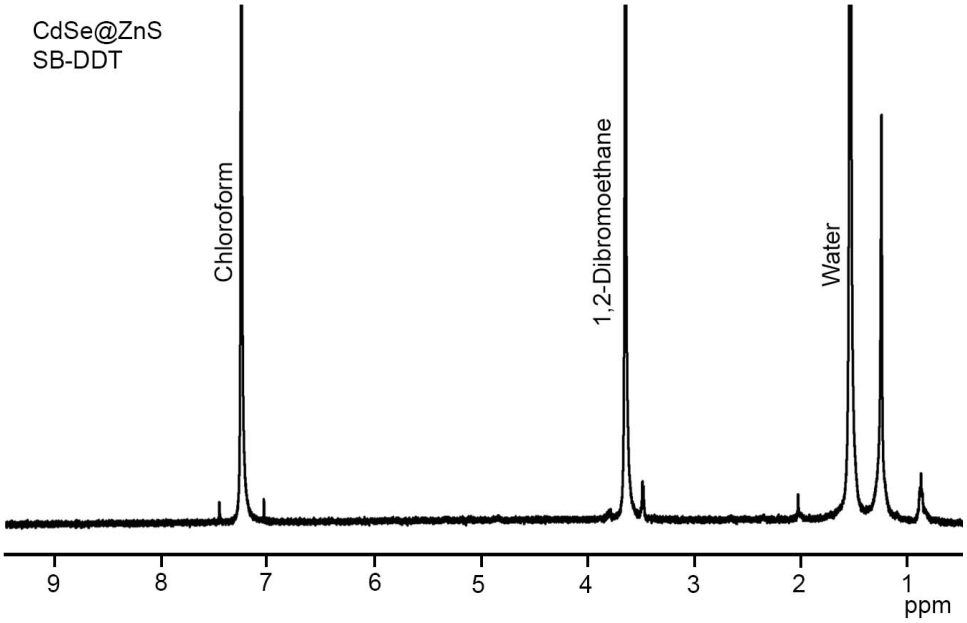

Figure 3.14: ^{1}H NMR of CdSe@ZnS with surface-bound DDT. 1,2-dibromoethane was added as an internal standard, ligand density was found to be 3.6 ligands/nm^2 for the surface-bound DDT.

CHAPTER IV

COMPUTATIONAL MODELING OF THE LIGAND COORDINATION ON CORE-SHELL QUANTUM DOTS

4.1 Introduction

Quantum dots (QDs) have emerged as a promising class of nanomaterials for electronic, energy, and biomedical applications.[11, 15] QDs are often made using solution based syntheses, which allow for control over the reaction parameters and yield monodisperse products. In the solution based synthesis of QDs, organic ligands are used to coordinate to the surface of the crystal lowering the surface energy and preventing growth beyond nanocrystal sizes.[17] The resulting QD is a sum of the crystalline inorganic core and these long-chained organic molecules, which cover the surface. The organic capping ligands play a key role in controlling colloidal growth and act as an insulating barrier around the QD core after the synthesis.[18] Therefore, understanding the nature of the coordination of organic ligands to the surfaces of QDs is vital to unraveling and optimizing growth mechanisms and ligand exchange processes needed for functional QD-based applications.[30, 103]

Organic ligands coordinate to surfaces of QDs in a similar fashion to established coordination compounds, as a neutral L-type ligand and a negatively charged X-type ligands.[33] L-type ligands, such as amines, are neutral donors of two electrons to a surface metal atom. In the case of X-type ligands, the negative charge allows for the passivation of excess charged metal atoms at the surface.[33] The models described here are a nonpolar surface, therefore the

excess surface metal cation is not part of the crystal lattice, and effectively the ligand binds to the surface as a MX_2 complex. This binding mode is called a Z-type ligand (Figure 4.1).[32]

The other ligand coordination modeled in this chapter is crystal-bound ligands.[9] For crystal-bound ligands, an alkyl chain passivates the sulfur site of a metal-sulfide. As I shared in chapter 3 for ZnS shells with crystal-bound thiols there is the presence of an additional small molecule X-type ligand is present at the cation site and provides charge balance to the system.[10]

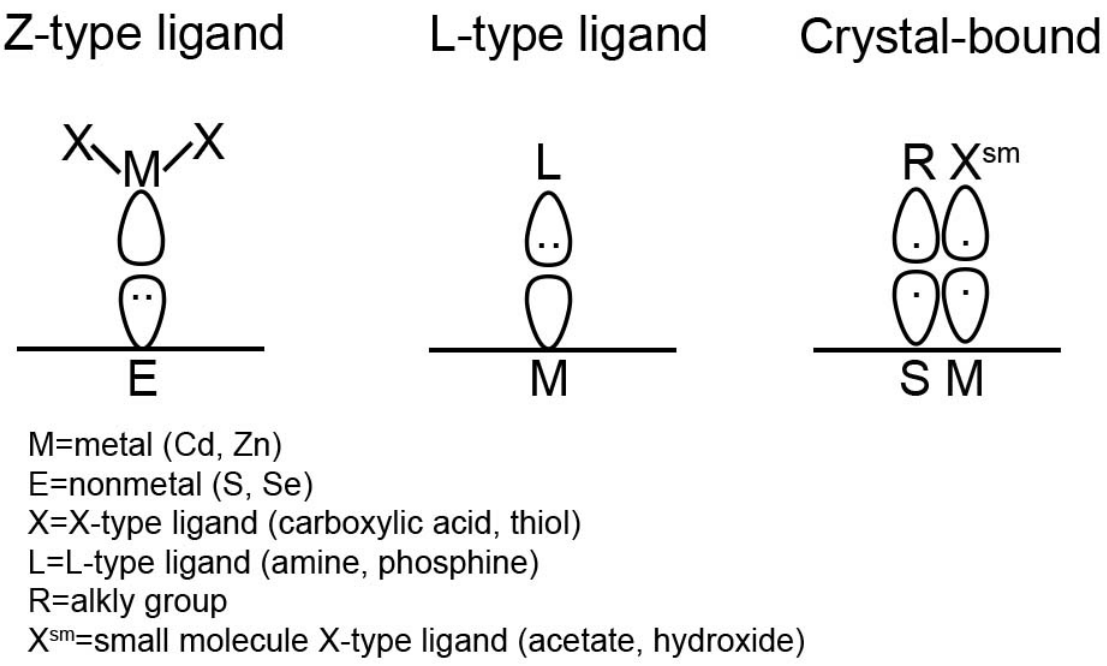

Figure 4.1: Binding of neutral ligands to a nonpolar surface

Current methods for the analysis of ligand coordination only indirectly probe the surfaces of quantum dots.[37] NMR and various 2D NMR techniques have become the most common methods used, however the surface chemistry can only be inferred by examining ligand exchange or surface reactions.[36] Similarly, mass spectrometry techniques including TGA-MS and MALDI rely on characterizing removed organics from the surface.[9, 104] Infrared

spectroscopy,[105] XPS,[106] and solid state NMR[107, 108] can provide chemical information about the surface and the ligands, however these techniques are limited in providing structural data and single crystal studies are limited to well defined homogenous clusters.[109]

One characterization technique that has the potential to directly probe the surface of QDs is X-ray Absorbance Spectroscopy (XAS).[110, 111] XAS looks at two types of effects, the dipole allowed transitions from core orbitals to unoccupied molecular orbitals and the scattering of the photoexcited electrons.[112] The dipole allowed transitions, as studied in X-ray Absorption Near Edge Spectroscopy (XANES), are sensitive to localized bonding.[112] The higher energy transitions are called Extended X-ray Absorption Fine Structure (EXAFS) which are a result of scattering of photoexcited electrons off neighboring atoms, providing information about the local structure.[112] The focus of my study is on the S K-edge XANES, which is the transition from the S1s orbital to the conduction band orbitals with p-orbital character. Meaningful interpretation of XAS spectra requires structural models for comparison.

4.2 Results and discussion

4.2.1 Surface-bound structural models

In order to begin to analyze the simulated XAS of surface coordination the structural effects of surface-bound ligands needs to be understood. Density Functional Theory (DFT) calculations were performed using the Purdew-Burke-Ernzerhof (PBE) version of the exchange-correlation functional,[100] Projector Operator Wave (PAW) potentials,[101] and a plane-wave basis as implemented in the Vienna *Ab initio* Simulation Package (VASP) code.[102] The plane-wave energy cutoff was set at 540 eV and a 6x6x1 k-point sampling was used. For all of the slab

models, the cell parameters were also relaxed in addition to the atomic positions. The slab consisted of 9 layers of zinc blende CdSe and 2 and 4 layers (1 and 2 monolayers (ML)) of ZnS placed epitaxially placed on the CdSe core. The focus of the simulation is on the nonpolar (110) facet of zinc blende CdSe@ZnS since the (110) facet is the lowest energy facet.[92] Therefore, a rotated unit cell was used with the C axis as the (110) facet, the A axis as the ($\bar{1}$10), and the B axis as the (001). The slabs were separated by at least 10 Å, ensuring no artificial interactions. The density of ligands on the slab is 3.8 ligands/nm^2, which is consistent with observed ligand densities on QDs.[36]

All of the models in this chapter were constructed and simulated by myself, as opposed to the models presented in Chapter 3, which were constructed by Dr. Xiao Shen. The models here built on Dr. Shen's work. In Chapter 3, we assume the ZnS is strained and takes on the lattice parameter of the CdSe. In this chapter we allow for complete relaxation of the cell parameters. The results in this chapter, therefore, are more accurate but more computationally expensive. We also extend the models to additional ligand binding modes and thicknesses of ZnS shell.

Figure 2 shows the relaxed structure of the different surface-bound ligand coordinations, including the L-type amine, the Z-type Zn(carboxylate)$_2$, and the Z-type Zn(thiolate)$_2$. The binding energies per cell ($E_{binding}$) of the different surface-bound binding coordinations are shown in Table 4.1 and were determined by the equation (4.1):

$$E_{binding} = E_{total} - E_{surface} - E_{ligand} \quad (4.1)$$

Where E_{total} is the energy of the relaxed structure with the surface-bound ligands per cell, $E_{surface}$ is the energy of the relaxed slab without any capping ligand per cell, and E_{ligand} is the energy of

the free ligand. The binding energies of the surface-bound ligands is consistent with experimental observed trends in ligand coordination, where thiolates bind more strongly than carboxylates and amines, and amines and Z-type carboxylates can displace each other.[32, 113]

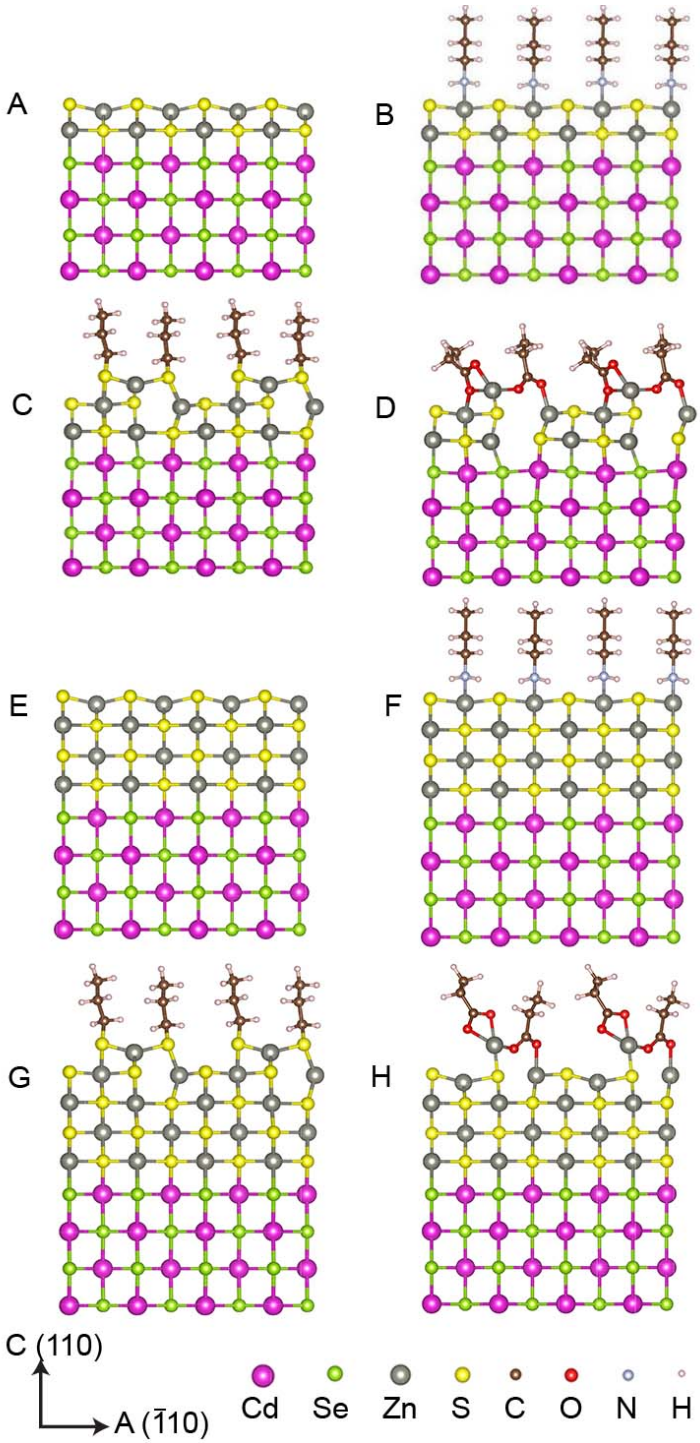

Figure 4.2: Structural models of ligand coordination to the (110) surface of CdSe/ZnS slabs. (A) 1 ML of ZnS and no ligands, (B) 1 ML of ZnS and L-type propylamine, (C) 1 ML of ZnS and Z-type Zn(propanethiolate)$_2$, (D) 1 ML of ZnS and Z-type Zn(propionate)$_2$, (E) 2 ML of ZnS and no ligands, (F) 2 ML of ZnS and L-type propylamine, (G) 2 ML of ZnS and Z-type Zn(propanethiolate)$_2$, (H) 2 ML of ZnS and Z-type Zn(propionate)$_2$.

Table 4.1: Binding energies of the capping ligands

Passivation	Shell Thickness	Energy (eV)	Binding Energy (eV) per cell
No Ligands	1 ML	-125.84	
	2 ML	-152.55	
Amine	1 ML	-264.80	-1.56*
	2 ML	-291.75	-1.66*
$Zn(carboxylate)_2$	1 ML	-248.41	-1.60
	2 ML	-274.95	-1.43
$Zn(thiolate)_2$	1 ML	-243.44	-1.80
	2 ML	-270.37	-2.02

*Binding energy is for 2 amine ligands

The structure of the relaxed bare surface results in an expected distortion of the surface atomic arrangements, where the Zn atoms relax to below the surface to increase coordination.[114] Upon the addition of L-type amine capping ligands there is a slight return of the surface structure towards the bulk configuration. In contrast, the coordination of Z-type ligands has a different structural effect, the formation of cracks in the shell lattice. In the 1 ML and 2ML models with no passivation or L-type passivation, epitaxy is maintained throughout the shell lattice with a Zn-S bond distance of around 2.50 Å in the AB plane. For the slab models with Z-type $Zn(thiolate)_2$ passivation, the crack only forms on the surface layer with a Zn-S bond distance of 3.60 Å at the surface compared to 2.67 Å at the CdSe/ZnS interface for the 1 ML model. For the 2 ML model the, the crack at the surface is narrowed slightly to a Zn-S bond distance of 3.30 Å, while at the CdSe/ZnS interface a distance of 2.48 Å was measured. In the

Z-type Zn(carboxylate)$_2$ for 1 ML the defect persists throughout the shell with Zn-S bond distances of 3.65 Å at the surface and 3.58 Å at the CdSe/ZnS interface. 2 ML Zn(carboxylate)$_2$ has a significantly smaller defect with a Zn-S bond distance of 2.71 Å at the surface and 2.47 Å at the interface. For the 2 ML model there is only one bridging carboxylate resulting in less strain on the surface and the smaller defect.

The crack defects stem from a bridging coordination where the organic ligand binds to both the adatom cation and an open surface site.[115] Similar bridging coordinations of Z-type ligands have been previously observed in single crystal x-ray structure of InP clusters passivated by X-type ligands.[109] This additional passivation increases the tensile strain on the already strained shell, resulting in a displacements within in the atomic layers. The observed defects are a separation along the $(\bar{1}10)$ lattice direction.

The bridging coordination significantly increases the binding energy of the ligand. For Zn(thiolate)$_2$ both of the thiols relaxed to coordinate surface Zn atoms, 1-bridging thiolate coordination resulted in a decrease in the binding energy of the Zn(thiolate)$_2$ ligand by 0.47 eV for 1 ML and 0.49 eV for 2 ML. The non-bridging structure would not relax to a local minimum.

For the Zn(carboxylate)$_2$ models, the 1 ML slab only stabilizes as a 2-bridging coordination, while the 2 ML slab relaxed to both the one and two bridging ligands. Interestingly the two different bridging modes had similar total energies with the 2-bridging model 0.03 eV lower in energy. The similar energies are a result of a trade off between the passivation of the surface sites and the formation of defects in the lattice. There is a significant dislocation in the shell for the 2-bridging model with Zn-S bond distance of 3.98 Å at the

surface and 3.58 Å at the CdSe/ZnS interface. This lattice separation results in an increase in the total energy of the core/shell structure of 0.65 eV if the ligands are removed.

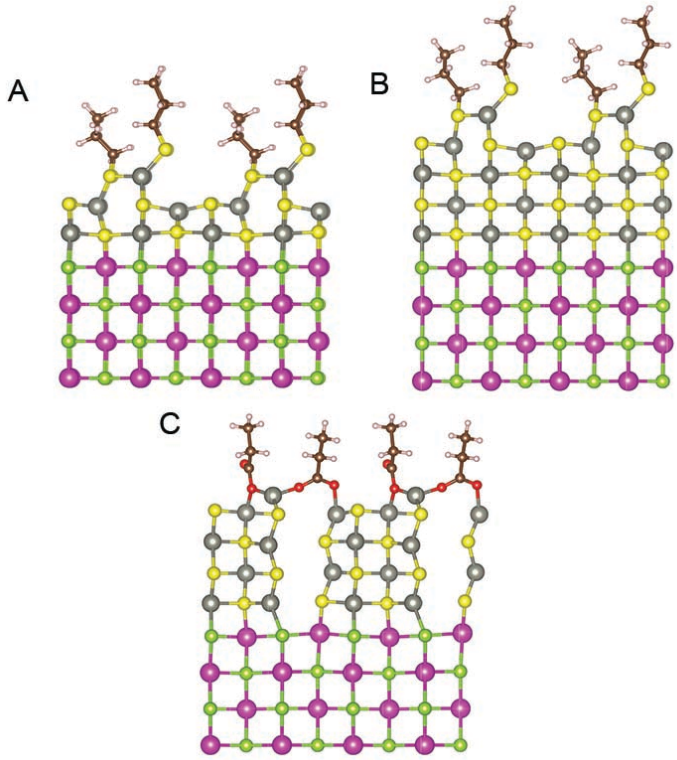

Figure 4.3: Alternate bridging coordinations of Z-type ligands (A) 1 ML ZnS with a 1-bridging Z-type Zn(propanethiolate)$_2$, (B) 2ML of ZnS with a 1-bridging Z-type Zn(propanethiolate)$_2$, (C) 2 ML of ZnS with a 2-bridging Z-type Zn(propionate)$_2$.

The different structural effects of the Zn(thiolate)$_2$ compared to the Zn(carboxylate)$_2$ are a result of the bond length between the Zn-ligands and the increased binding configuration of the carboxylate. The average Zn-O bond distance in the samples is 2.04 Å, while for the Zn-S bond distance of the capping ligands that distance is increased to 2.34 Å.

Somewhat surprisingly, calculated densities of states (DOS) indicate the lattice crack defects do not form any midgap states. For the DOS calculations, the 1 ML thick ZnS shell was used. The DOS of the clean surface is consistent with previous simulations of ligand free (110) surfaces where the structural relaxations at the surface shift the unpassivated states out of the

band gap.[114] All of the ligand passivated models calculated here also do not have any midgap states. The absence of midgap states is attributed to the defect forming a $(\bar{1}10)$ surface, therefore the same structural relaxations that occur on the unpassivated surface also are inside of the crack passivating any midgap states.

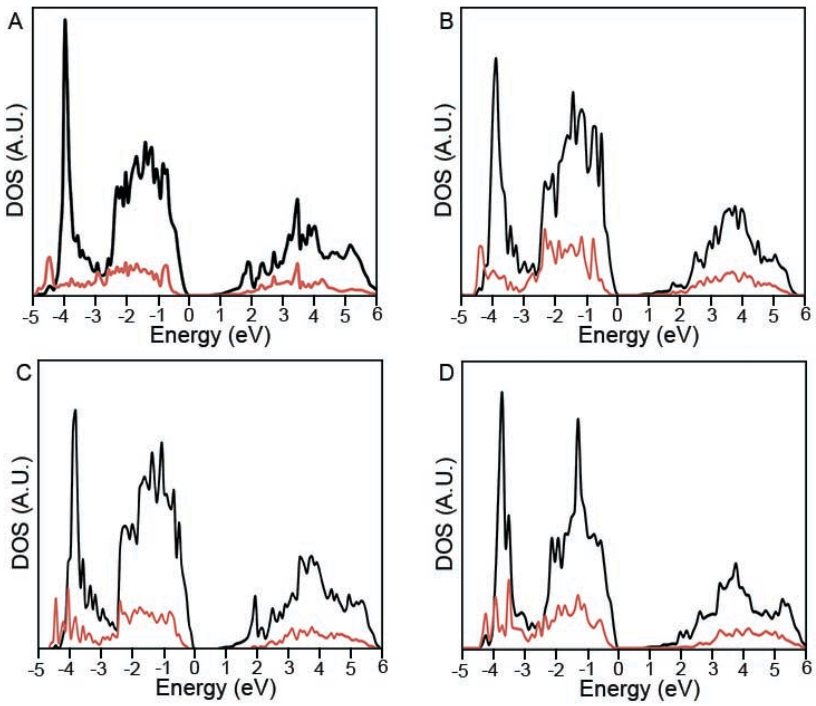

Figure 4.4: Total densities of states for the CdSe (black) and ZnS (red) of the structural models. (A) 1 ML of ZnS and no ligands, (B) 1 ML of ZnS and L-type propylamine, (C) 1 ML of ZnS and Z-type Zn(propanethiolate)$_2$, (D) 1 ML of ZnS and Z-type Zn(propionate)$_2$. All plots are calibrated such that the Fermi energy is 0 eV.

Previous experimental work has shown that Z-type ligands can induce structural changes in QD systems. Buhro *et al.* showed that for the nonpolar (112) facet of wurzite CdSe nanoplatets, ligand exchange from a L-type oleylamine capping to a Z-type Cd(Oleate)$_2$ capping causes a reversible red shift in the absorbance spectrum resulting from the induced strain on the CdSe lattice.[116] Additionally, Greytak *et al.* observed an irreversible red-shift upon the ligand

exchange of L-type ligands with Z-type ligands on the surface of CdSe@CdS,[117] this structural change can be attributed to the cracking of the shell releasing compression strain on the core.[118]

The structural defects resulting from the coordination of the Z-type ligands may play a key role in the formation of lattice defects during shell growth. Recent HR-TEM studies have shown the appearance of lattice defects in the shell even when there is no lattice mismatch between the core and shell structure.[119] This study concluded that ligand coordination during shell growth plays a key role in the formation of stacking faults. The appearance of stacking faults in shells can be directly correlated to increased blinking of the QD.[120] The computational models presented in this chapter reveal a structural explanation for the role surface ligand coordination can play in inducing lattice defects. The induced strain from the bridging coordination of Z-type ligands can cause surface defects that can lead to the stacking fault as the shell grows.

4.2.2 XAS simulations for ligand binding determination

For the determination of ligand binding with XAS, the relaxed structures of CdSe/ZnS with crystal-bound ligand passivation were computed similarly to the surface-bound models discussed in section 4.2.1 (Figure 4.5). Structurally, crystal-bound ligands maintain the epitaxy of the core/shell lattice with no crack formation. Hydride was used as the small molecule X-type ligand to passivate the exposed zinc sites and maintaining charge balance of the models. Hydride was used to decrease the computational resources needed.

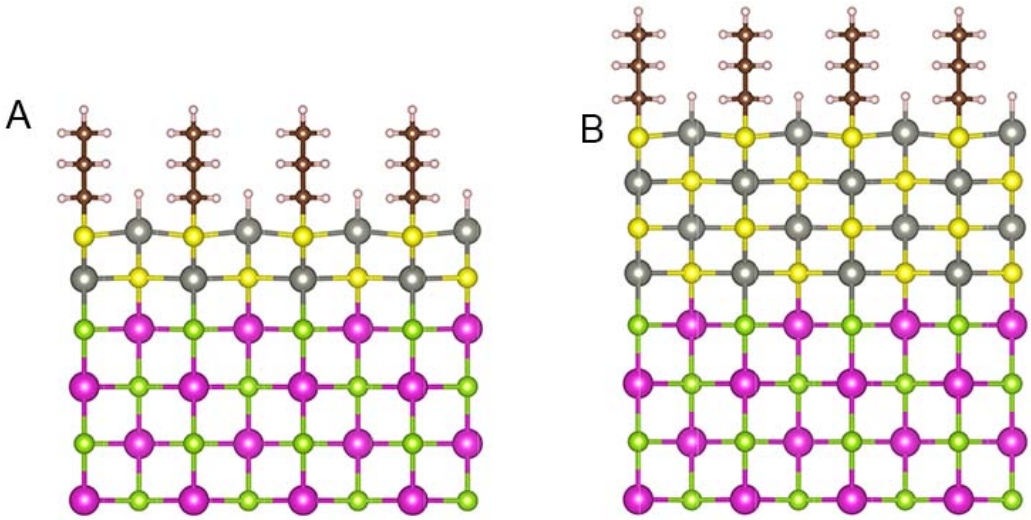

Figure 4.5: Relaxed structural models for CdSe/ZnS with crystal-bound ligand passivation with 1ML (A) and 2ML (B) of ZnS. Hydride was used as the small molecule X-type ligand.

XAS were computed by DFT with a planewave basis set using the Quantum Espresso code.[121] To calculate the final state of the electronic structure the eXcited electron Core-Hole (XCH) method was used.[122] XCH solves the wavefunction for the model when a core hole is localized on a single atom with an electron in the lowest energy unoccupied orbital. The subtraction of the initial and final states results in a calculated spectrum of an individual atom. The total spectrum of a model consists of the average spectra of each atom in a unique chemical and local environment.

Figure 4.6 is the simulated S K-edge XAS spectrum of bulk zinc blende ZnS. The computed spectrum agrees well with spectra in the literature. For zinc blende ZnS there are four peaks related to the transition between the S1s orbital and the conduction band states with p-orbital character, labeled A-D in Figure 4.6.[123, 124] In the 2ML models the same four peaks can be identified in all the average spectra (Figure 4.7). However there are differences in the relative contributions of peaks B, C, and D depending on the surface passivation. For crystal-

bound ligands there is a depression in all of the peaks relative to peak A, for the L-type amine passivation there is a suppression of peak D, and in the Z-type $Zn(thiolate)_2$ sample there was a decrease in peak B.

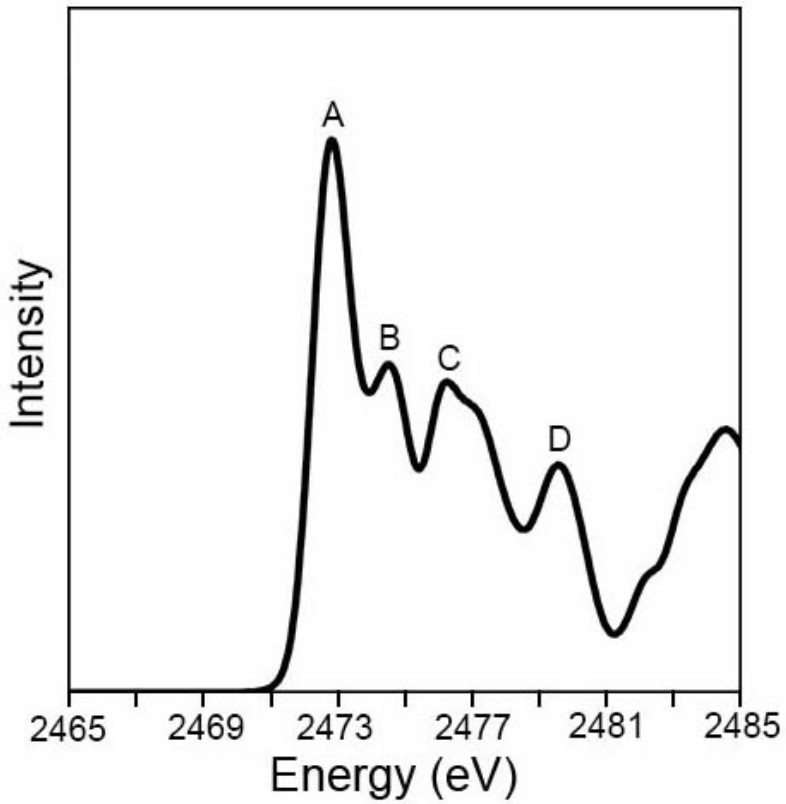

Figure 4.6: Simulated S K-edge XAS spectrum of bulk zinc blende ZnS. Labels correspond to peaks discussed in the text.

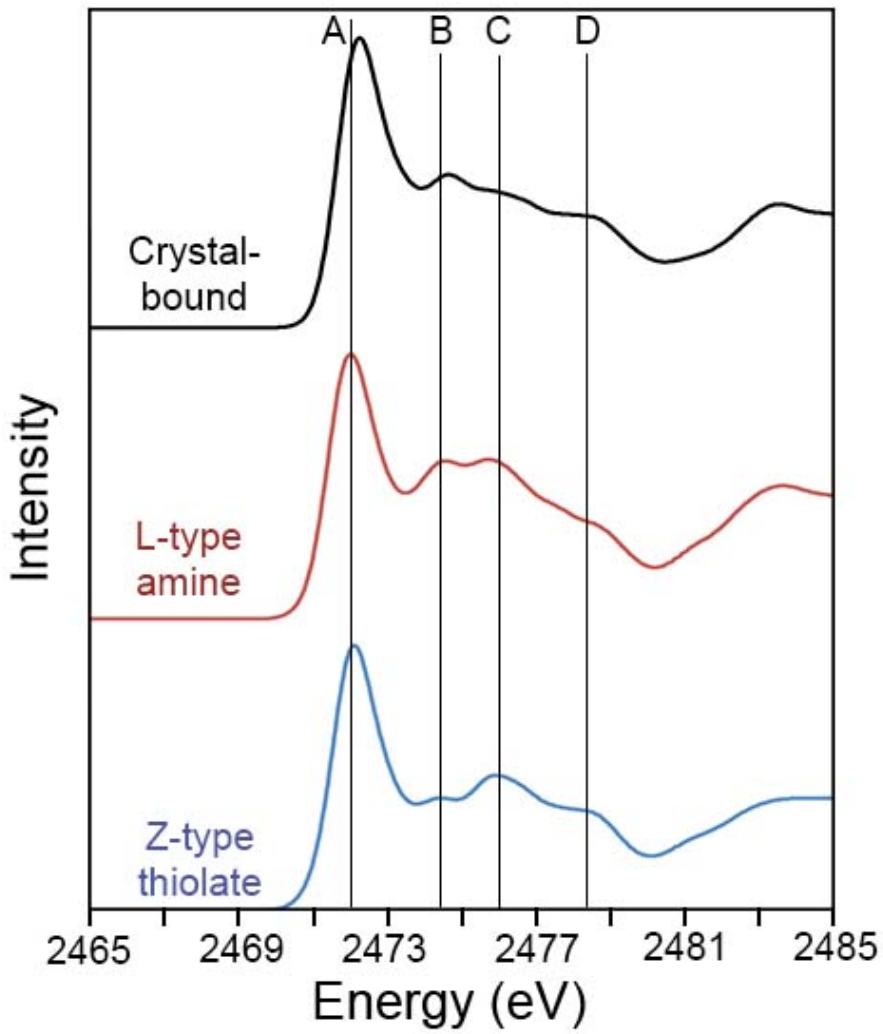

Figure 4.7: Simulated S K-edge for the average XAS spectra for different ligand binding modes on the surface of CdSe/ZnS slab models with 2ML of ZnS. Black spectrum corresponds to crystal-bound thiol ligands, red spectrum is for L-type amine passivation, and blue plot is for Z-type $Zn(thiolate)_2$ passivation.

By looking at the individual atomic contributions to the average spectrum, the nature of the changes in the peak intensities can be determined. In all of the models, the two monolayers at the interface maintained all of the four characteristic peaks for ZnS. For the crystal-bound model (Figure 4.8) the contribution of the top layer is dominated by the C-S bond, which has a similar position to peak A. This causes an apparent relative decrease in the contributions of peaks B, C, and D. The L-type ligand passivation model has open surface sulfur atoms that

result in the decrease of peak D (Figure 4.9). In the Z-type $Zn(thiolate)_2$ model, the defects in the surface structure discussed in section 4.2.1 cause a decrease in the intensity of peak B (Figure 4.10). Similar trends are observed in the 1ML models as the 2ML models, however peaks B, C, and D are not as clearly defined (Figures 4.11 to 4.14).

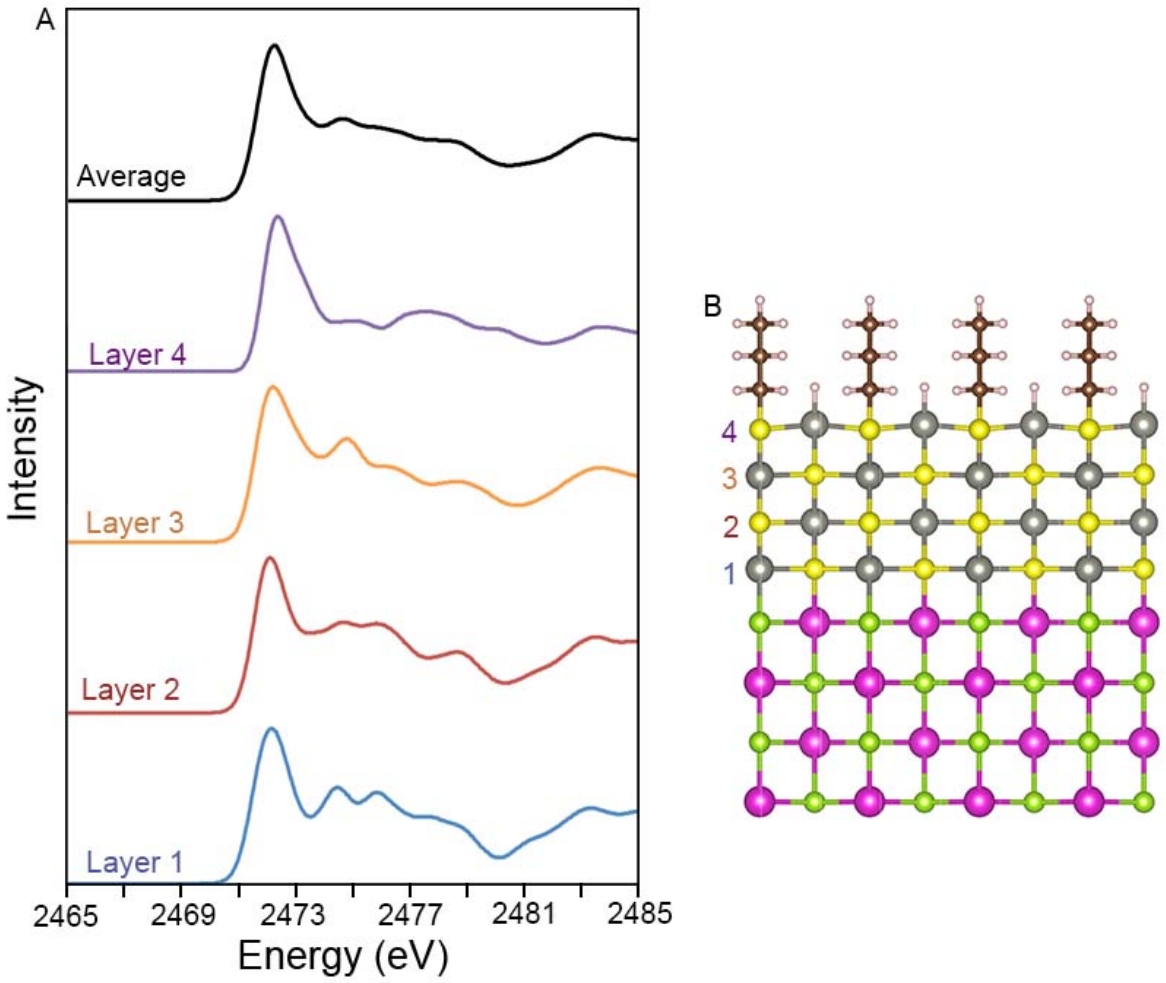

Figure 4.8: (A) Simulated S K-edge XAS spectra for CdSe/ZnS core shell model with 2ML of ZnS and crystal-bound ligands and (B) the corresponding structural model. The black spectrum is the average of individual atomic calculations. The colored spectra are the spectra for each individual atom. Layer 1 is the layer at the CdSe/ZnS interface, represented by the blue spectrum, layer 2 is the red spectrum, layer 3 is the orange spectrum, and layer 4, the surface, is the purple spectrum.

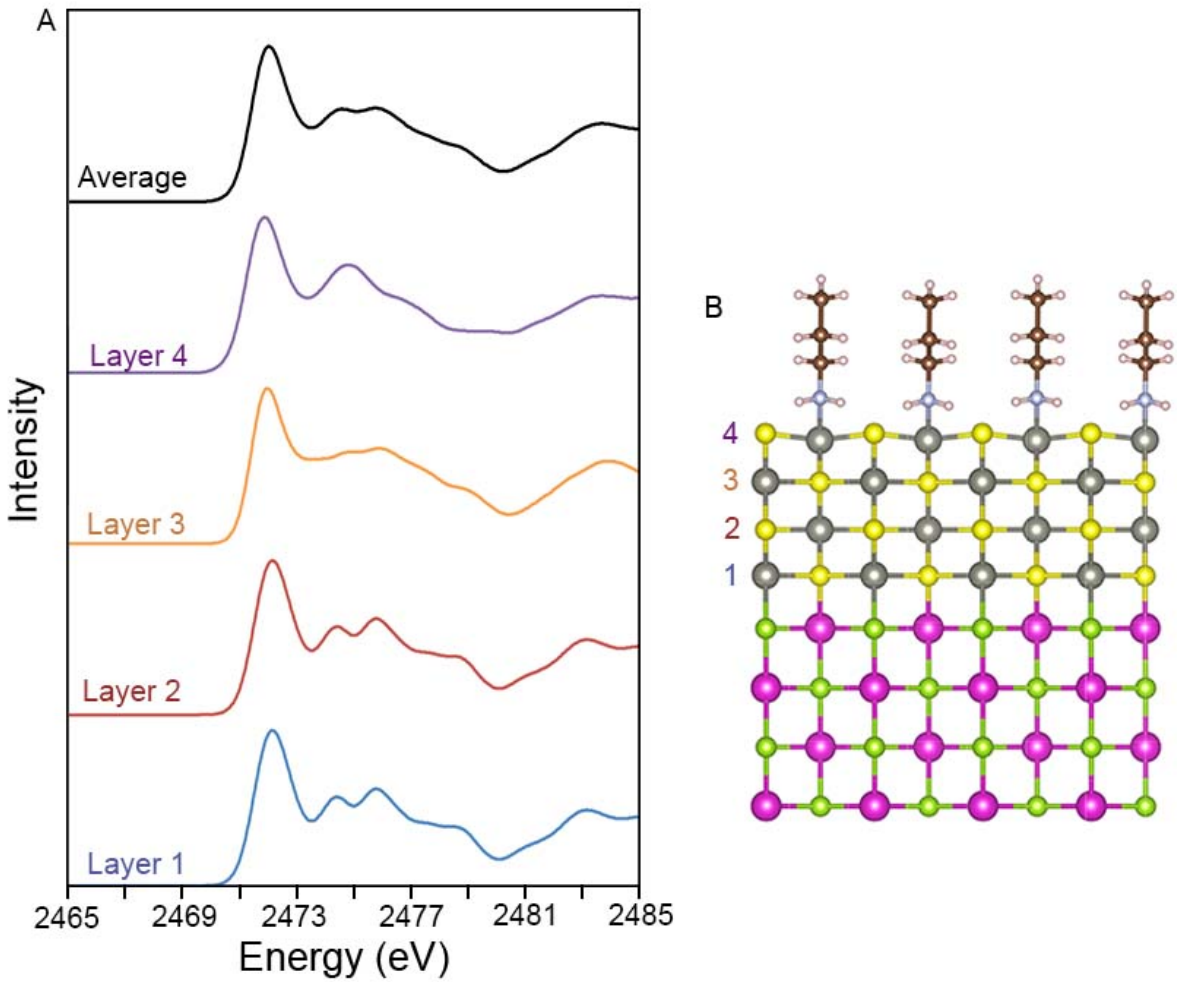

Figure 4.9: (A) Simulated S K-edge XAS spectra for CdSe/ZnS core shell model with 2ML of ZnS and L-type amine ligands and (B) the corresponding structural model. The black spectrum is the average of individual atomic calculations. The colored spectra are the spectra for each individual atom. Layer 1 is the layer at the CdSe/ZnS interface, represented by the blue spectrum, layer 2 is the red spectrum, layer 3 is the orange spectrum, and layer 4, the surface, is the purple spectrum.

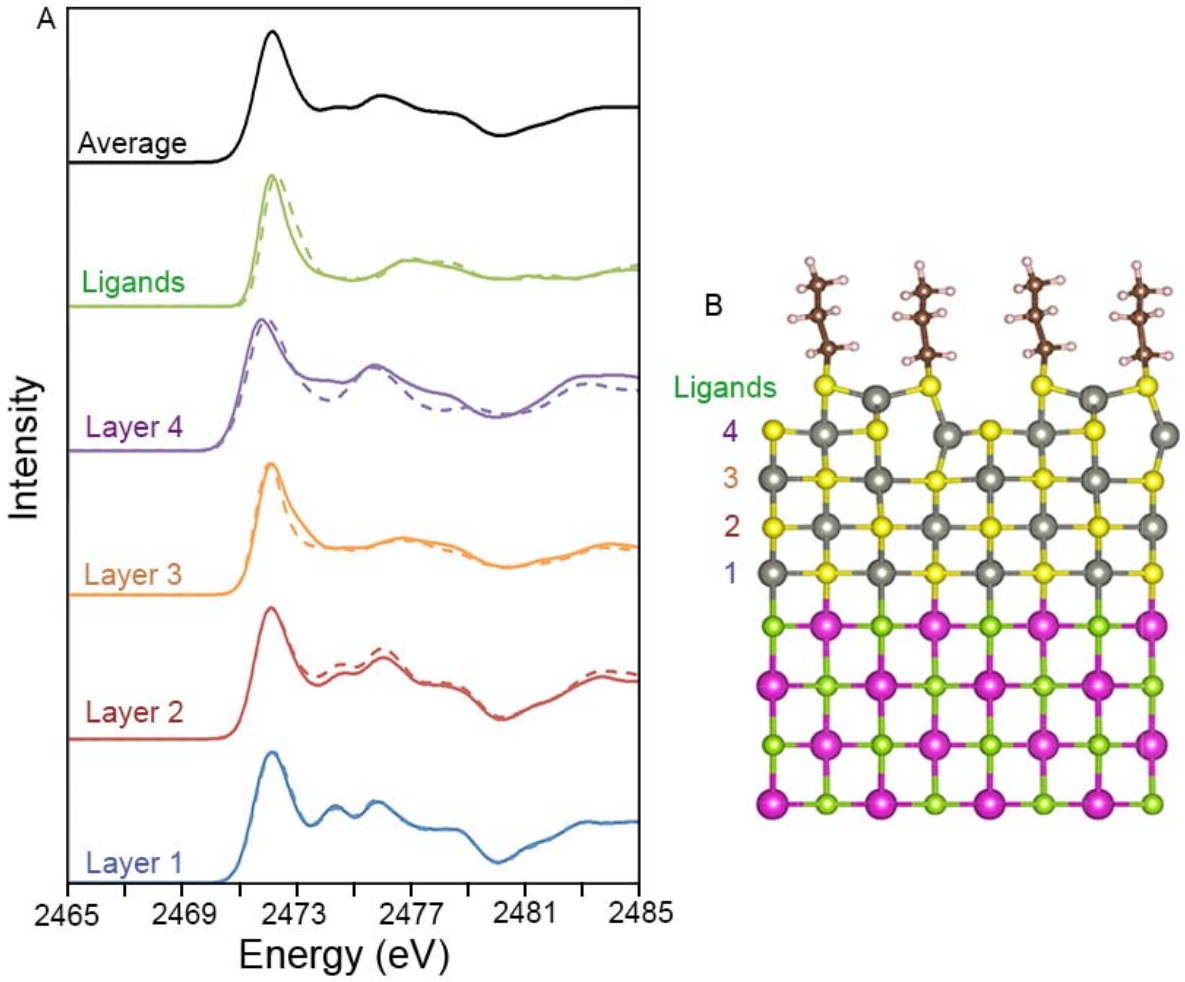

Figure 4.10: (A) Simulated S K-edge XAS spectra for CdSe/ZnS core shell model with 2ML of ZnS and Z-type Zn(thiolate)$_2$ ligands and (B) the corresponding structural model. The black spectrum is the average of individual atomic calculations. The colored spectra are the spectra for each individual atom. Layer 1 is the layer at the CdSe/ZnS interface, represented by the blue spectrum, layer 2 is the red spectrum, layer 3 is the orange spectrum, and layer 4, the surface, is the purple spectrum. The green spectra are the sulfur in the surface capping thiolates. The presence of the Z-type ligand results in the formation of the crack at the surface causing two different local environments to be present at each layer. This resulted in two spectra for each layer one presented as a solid line and the other as a dashed line.

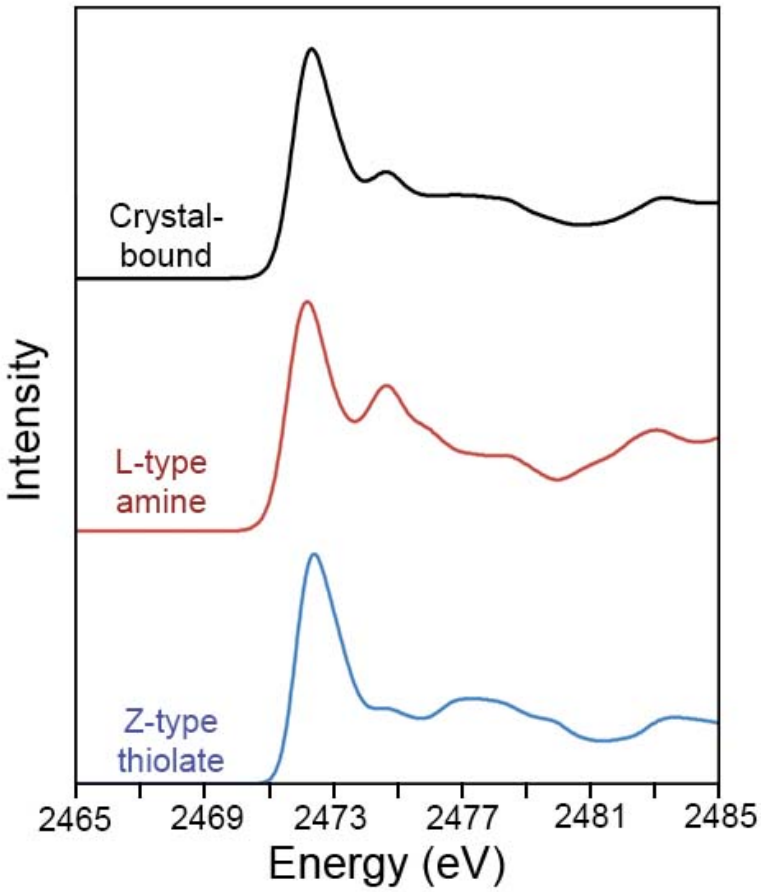

Figure 4.11: Simulated S K-edge for the average XAS spectra for different ligand binding modes on the surface of CdSe/ZnS slab models with 1ML of ZnS. Black spectrum corresponds to crystal-bound thiol ligands, red spectrum is for L-type amine passivation, and blue plot is for Z-type $Zn(thiolate)_2$ passivation.

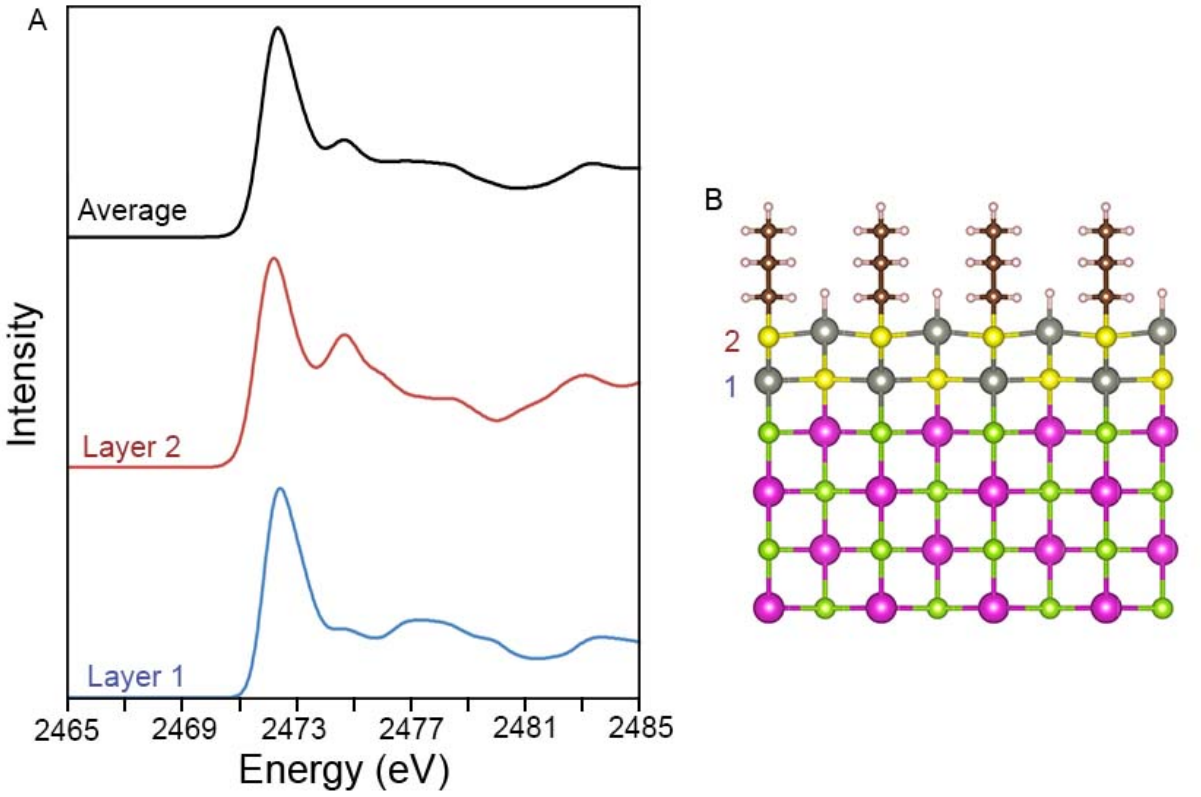

Figure 4.12: (A) Simulated S K-edge XAS spectra for CdSe/ZnS core shell model with 1ML of ZnS and crystal-bound ligands and (B) the corresponding structural model. The black spectrum is the average of individual atomic calculations. The colored spectra are the spectra for each individual atom. Layer 1 is the layer at the CdSe/ZnS interface (blue spectrum) and layer 2, the surface (red spectrum).

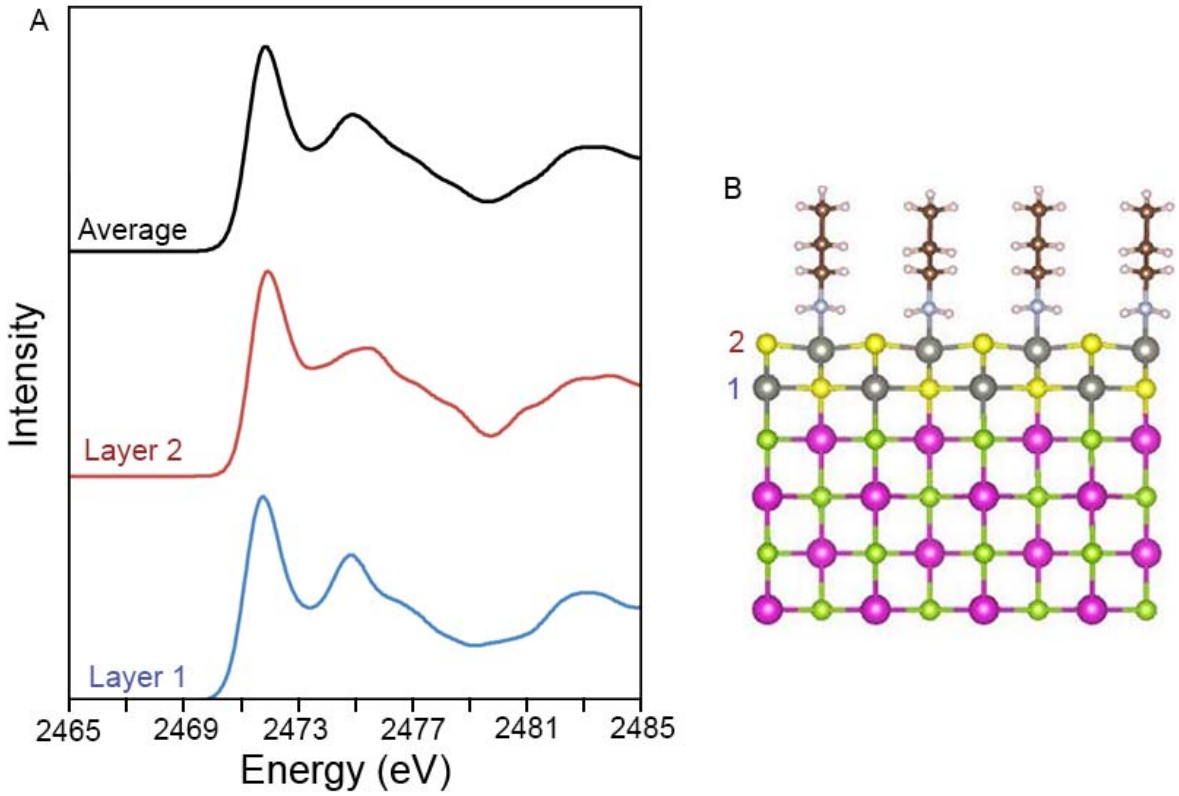

Figure 4.13: (A) Simulated S K-edge XAS spectra for CdSe/ZnS core shell model with 2ML of ZnS and crystal-bound ligands and (B) the corresponding structural model. The black spectrum is the average of individual atomic calculations. The colored spectra are the spectra for each individual atom. Layer 1 is the layer at the CdSe/ZnS interface (blue spectrum) and layer 2, the surface (red spectrum).

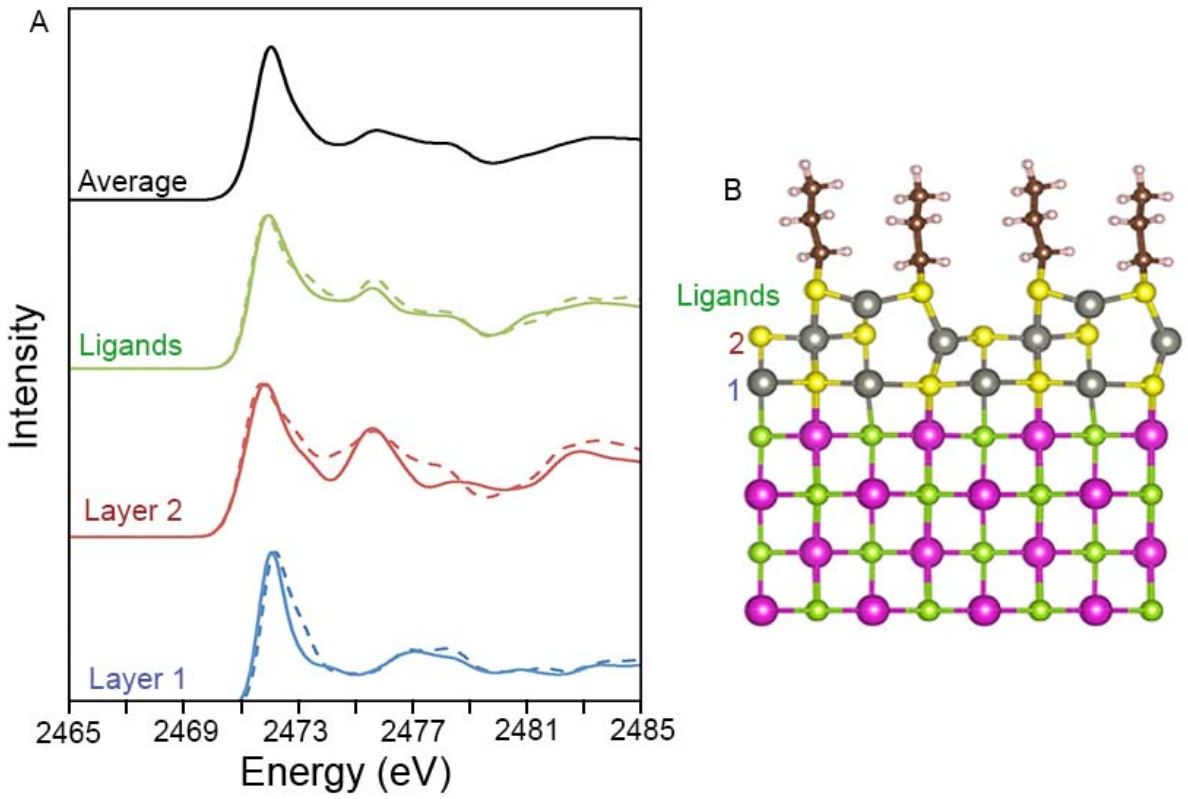

Figure 4.14: (A) Simulated S K-edge XAS spectra for CdSe/ZnS core shell model with 1ML of ZnS and Z-type Zn(thiolate)$_2$ ligands and (B) the corresponding structural model. The black spectrum is the average of individual atomic calculations. The colored spectra are the spectra for each individual atom. Layer 1 is the layer at the CdSe/ZnS interface (blue spectrum) and layer 2, the surface (red spectrum). The green spectra are the sulfur in the surface capping thiolates. The presence of the Z-type ligand results in the formation of the crack at the surface causing two different local environments to be present at each layer. This resulted in two spectra for each layer one presented as a solid line and the other as a dashed line.

4.3 Conclusion

In order to directly probe the surface coordination of crystal-bound thiols to the surfaces of CdSe@ZnS nanocrystals, computational models were developed to provide and atomistic views of the surface. To the best of my knowledge, these are the first models of ligand coordination to the surfaces of core shell QDs. These models resulted in the unexpected formation of cracks in the shell structure for Z-type ligands. The bridging passivation of Z-type

ligands causes additional tensile strain on the surfaces of the crystal. This strain induces the formation of defects on the surfaces of the nanocrystals. The presence of these defects may contribute to the formation of stacking faults during shell growth.

Using the relaxed structural models for both surface-bound ligands and crystal-bound thiols XAS simulations were performed. Ideally XAS can probe local coordination, therefore can provide a direct probe of the crystal-bound ligand coordination. For ZnS there are four defined peaks in the XANES region, the three higher energy peaks are sensitive to the structural effects of the various surface passivations. In the different surface passivation models the contributions of these can be assigned to the structural differences, including surface defects and unpassivated surface atoms.

Overall, these models provide new insights in the effect of ligand passivation on surface structure. They are also the first step towards the use of XAS as a means to directly probing ligand binding on core-shell nanocrystals. Further models involving the coordination of ligands of additional facets such as the (111) and the (100) may be needed to better understand any experimentally obtained XAS spectra. Additionally, for the crystal-bound ligands, different small molecule X-type ligand passivation may play a role in the spectroscopy and may also need to be modeled. Experimental spectra are needed to validate the computational models.

CHAPTER V

HIERACHICAL NANOSTRUCTURES FROM COPPER(I) SULFIDE NANOCRYSTALS WITH CRYSTAL-BOUND LIGANDS[III]

5.1 Introduction

Transformations of presynthesized nanocrystals can provide a path to more advanced functional nanomaterials through processes such as hybrid nanoparticle synthesis[125] and oriented attachment.[126] Since both of these pathways rely on surface interactions, crystal-bound ligand coordination will play a major role by blocking facets and allowing control over the resulting products.

Hybrid nanoparticles are the combination of two or more disparate materials into a singular nanomaterial.[127] The combination of nanomaterials allows for synergistic interactions facilitating for new functionality in application, such as sensing, photocatalysis, photovoltaics, and bioimaging.[127] In the Macdonald laboratory, we are interested in the synthesis of semiconductor-metal hybrid nanoparticles for photocatalytic applications.[7] One of the most well studied semiconductor-metal hybrid nanoparticle system for photocatalytic water splitting is the CdSe@CdS dot in rod with a Pt tip.[128] In these systems the semiconductor (CdSe@CdS) absorbs the light and transfers an electron to the metal domain (Pt) for the reduction of water, the hole subsequently can be used for oxididation reactions, with the ideal reaction being water

[III] Some of the work discussed in this chapter is in preparation for publication in Robinson, E.H.; Turo, M. J.; Macdonald J.E. *in prep*. All work presented in this chapter was performed Michael Turo.

oxidation to yield complete water splitting. Since Cd is a toxic metal, moving towards more benign metals for the semiconductor would be beneficial.

In my work, I studied the synthesis of Cu_2S-Ru hybrid nanoparticles[50, 68] as a replacement for the Cd based nanocrystals for photocatalytic hydrogen production. Cu_2S is a promising material for solar energy capture with a band gap of 1.1-1.4 eV depending on the Cu to S stoichiometry, and a well placed band alignment to the water reduction potential.[71, 129] Ru metal is a known water reduction catalyst.[130] Previously, this system was synthesized by Banin *et al*. and displayed an unexpected structure where the Ru metal was deposited selectively on the edge sites resulting in a cage structure.[50, 68] This unique structure was observed as a result of the removal of the native capping ligands only on the more reactive edge sites at 205°C.[50]

In the previous work concerning the Cu_2S-Ru hybrid nanocages, selective removal of the edge site crystal-bound ligands results in the cage morphology. In my work, I have shown that the selective removal of crystal-bound ligands can be extended to different reactivities of facets. At elevated temperatures, presynthesized Cu_2S nanocrystals will attach at a unique facet and grow into nanorods. The mechanism of the rod formation is oriented attachment. The oriented attachment growth mechanism results in the fusing together of preexisting crystals along a preferential crystallographic axis.[131] This mechanism can be used to synthesize rods, wires, and rings.[126] Oriented attachment occurs as a result of dipole-dipole interactions of exposed surface facets resulting in coalescence to decrease the surface energy.[132] Ligands play a key role in preventing oriented attachment by lowering the surface energy of the facets and providing a physical barrier.[133]

5.2 Results and discussion

5.2.1 Cu_2S-Ru hybrid nanocrystals

The robust coordination of crystal-bound ligands provides a unique and exciting platform for advanced materials. The first example of this is the selective growth of Ru metal on the edge-sites of Cu_2S seed nanocrystals.[68] The control over different hybrid structures can influence the functionality of the nanomaterial. The cage hybrid structure observed for the Cu_2S system is no different. Initially, the cage hybrids were shown to act as a particle-to-particle wire improving the catalytic sensing of peroxide in a solid-state device.[68] Additionally, the cage structure also would improve charge separation compared to traditional hybrids potentially allowing for improved photocatalytic performance. However, since crystal-bound ligands are used in the synthesis of the cages the ligands could not be exchanged, preventing solubility in water and the application of these hybrids for photocatalytic water splitting.

The cages hybrids are synthesized by heating pre-synthesized Cu_2S nanocrystals in octadecylamine to 205°C, at which point $Ru(acac)_3$ in dioctylether is then injected into the Cu_2S-amine solution and left to react of 1h (Figure 5.1). This reaction is highly sensitive to the temperature of the reaction.[50] If the temperature is low the formation of individual Ru nanoparticles was observed resulting from heterogeneous nucleation. At higher temperatures, the growth of Ru nanonets is observed. To ensure the cage product is formed the temperature must be maintained within 1°C of the 205°C. In our lab, a custom heating mantle for a syringe is used to heat up the injected solution.

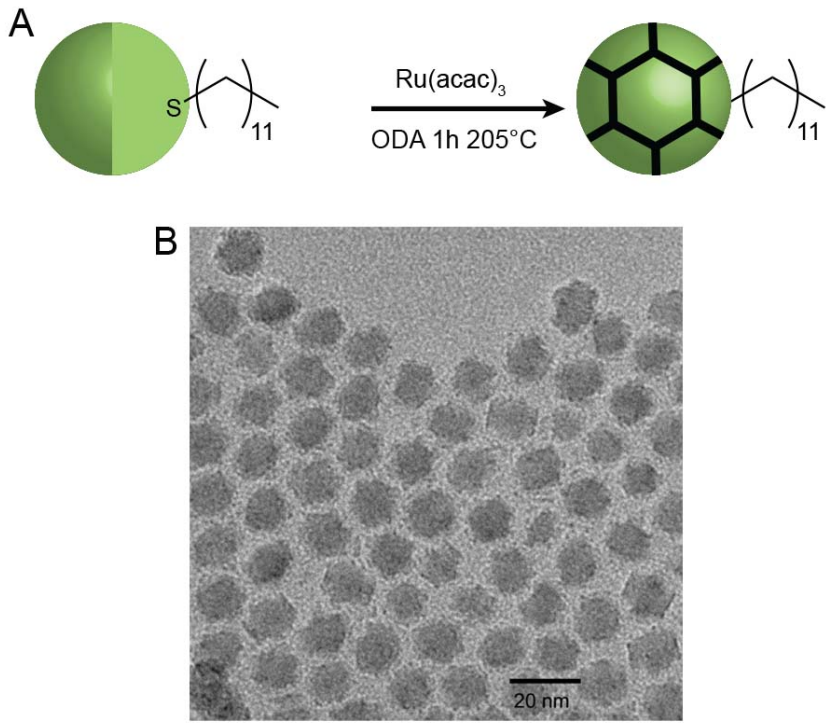

Figure 5.1: (A) Scheme for the synthesis of Cu_2S-Ru hybrid nanocages with DDT capped Cu_2S synthesized at 205°C. (B) TEM of the resulting Cu_2S-Ru cages using D3MP capped particles at 205°C.

To synthesize water-soluble Cu_2S cage hybrids, crystal-bound D3MP capped nanocrystals were synthesized as described in Chapter 2. Using the D3MP capped particles, the cage reaction was performed similar to the previous reports on the DDT capped particles. Unfortunately, the resulting product was not the cages hybrids, but rather the nucleation of individual Ru nanocrystals (Figure 5.2). This is indicative of insufficient heat to cleave the edge site ligands, preventing Ru deposition.

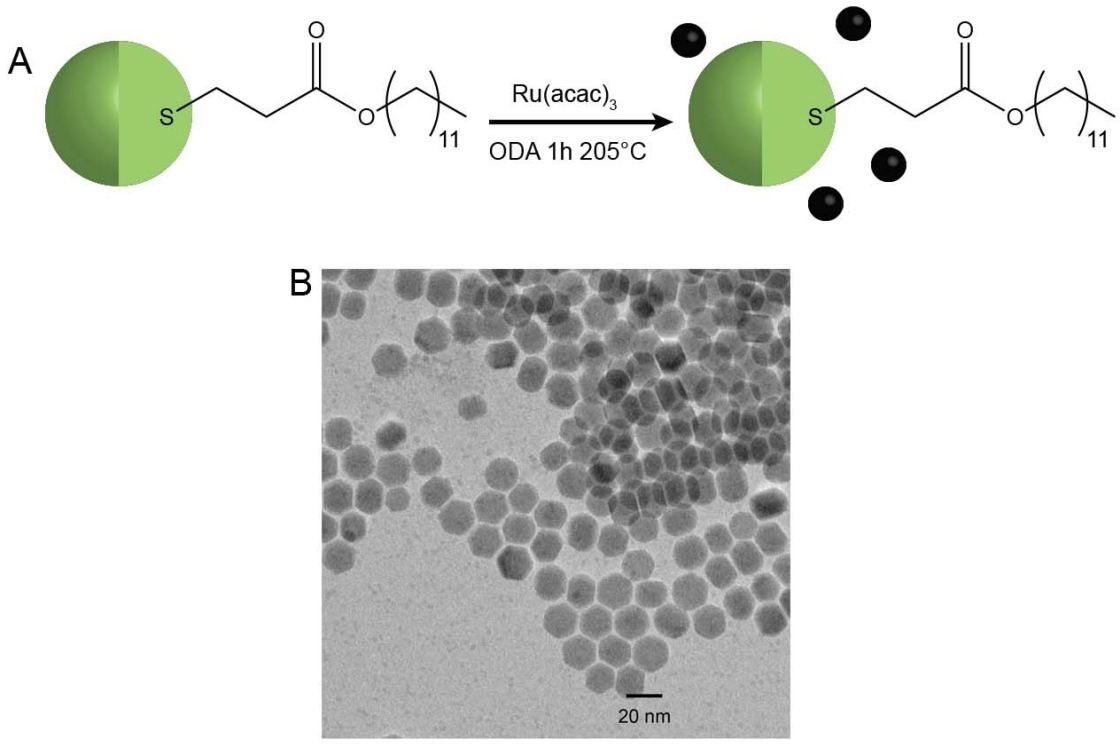

Figure 5.2: (A) Scheme for the synthesis of Cu_2S-Ru hybrid nanocages with D3MP capped Cu_2S synthesized at 205°C. (B) TEM of the resulting Cu_2S-Ru cages using D3MP capped particles at 205°C.

The decomposition of thiol ligands on the surface of Cu_2S nanocrystals results in the alkene product. The formation of the alkene proceeds through a beta-hydride elimination mechanism. However, in order for the β-hydride elimination to occur a 1,1-alkyl migration must first occur to put the alkyl chain onto the metal site.[9] The electron density of the migrating alpha-carbon can influence the rate of alkyl migrations. In D3MP, the ester group would pull electron density away from the α-carbon, which would change the temperature required to cleave the ligand. Using differential scanning calorimetry (DSC), it was determined that the edge site ligands of crystal-bound D3MP were removed at 217°C, significantly higher then the 203°C observed in crystal-bound DDT Cu_2S (Figure 5.3).[50] Therefore, the temperature was

increased in the reaction to form Ru cages on Cu_2S with crystal-bound D3MP to 220°C. Cage formation was successful at the elevated temperature (Figure 5.4).

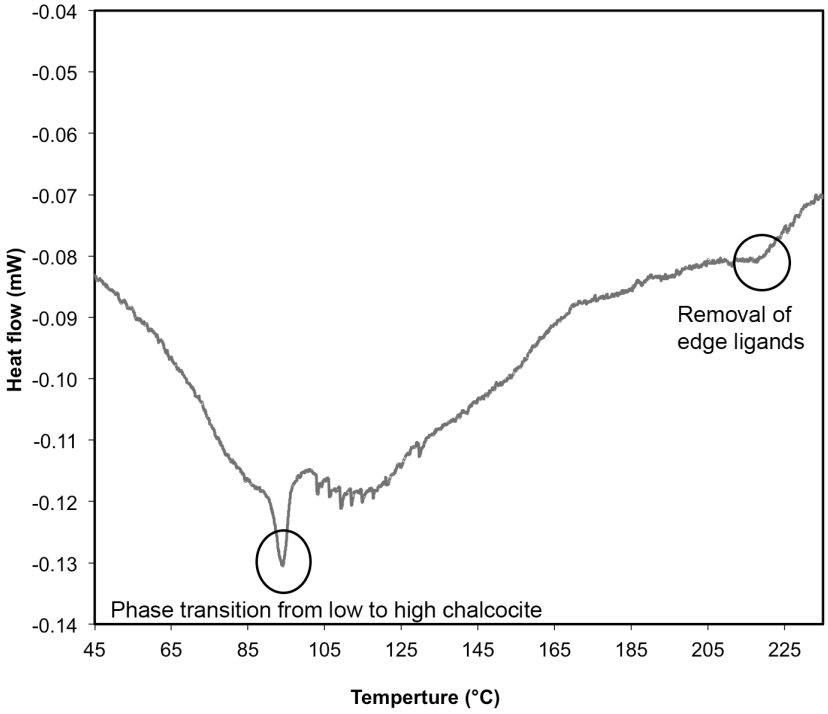

Figure 5.3: DSC heating curve for Cu_2S with crystal-bound ligands.

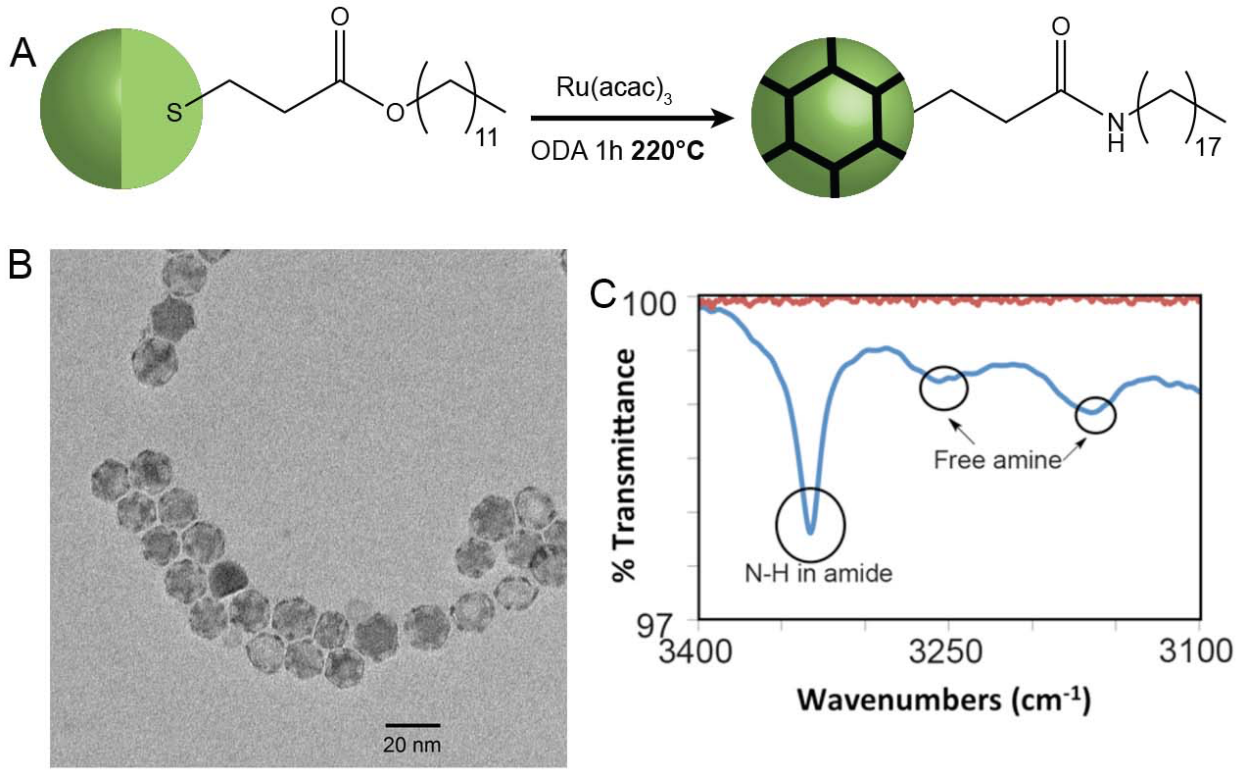

Figure 5.4: (A) Scheme for the synthesis of Cu_2S-Ru hybrid nanocages with D3MP capped Cu_2S synthesized at 220°C. (B) TEM of the resulting Cu_2S-Ru cages using D3MP capped particles at 220°C. (C) Partial IR of Cu_2S with crystal-bound D3MP before (red) and after (blue) the Ru cage formation. The appearance of the peak at 3360 cm^{-1} is evident of the amide formation.

A hydrolysis was attempted on Cu_2S-Ru cage hybrids with crystal-bound D3MP to cleave the ester allowing for water soluble particles.[9] Unfortunately, this failed to yield water-soluble particles. IR spectroscopy revealed the transition of the ester of D3MP to an amide during the cage synthesis (Figure 5.4C). The octadecylamine used as a reducing agent in the reaction also reacts with the ester to form the amide. Amides are significantly more difficult to hydrolyze then esters, and require harsh conditions that would destroy the particles. One mild amide hydrolysis procedure attempted, which involved the use of nitrites to oxidatively activate the amide allowing for less basic conditions and lower temperatures for the reaction.[134]

However, upon the addition of the nitrite, the solution immediately turned blue indicating the leaching of the Cu^{2+} ions from the particles.

To avoid the amide formation a reducing agent that is not a primary or secondary amine was used to replace for the reaction (Figure 5.5). Initial studies were conducted with 1,2-hexadecanediol (1,2-HDD), which resulted in homogeneous nucleation of Ru nanoparticles. Trioctylphosphine (TOP) was also tried as a reducing agent, however TOP is known to leach Cu from Cu_2S nanocrystals and is commonly used for cation exchange reactions.[135] Trioctylamine (TOA) resulted in the formation of Ru domains on some of the particles, in addition to homogeneous nucleation of Ru nanoparticles. It is expected that the trioctylamine is a stronger reducing agent then the primary octadecylamine because of inductive effects.

The use of stronger reducing agents prevents the formation of the cages because homogenous nucleation becomes dominant. With weaker reducing agents, the Cu_2S nanocrystal itself plays a role in the reduction of the Ru.[50] This is evident by the formation of the near-IR a surface plasmon resonance in the sample after the cage reaction.[68] The plasmon resonance is a result of the oxidation of the Cu_2S to substoichiometric $Cu_{2-x}S$ phase.[66] However, a weak reducing agent is still needed to yield the desired product.[50]

Therefore, in order to slow the rate of the reduction a lower concentration of trioctylamine was used. Decreasing the amount of trioctylamine to be stoichiometric with respect to the Ru still resulted in the formation of homogenous Ru nanocrystals. To decrease the reactivity of the tertiary amine was to use triethanol amine (TEA), which also resulted in the hmoogeneous nucleation of the Ru. To date there have been no Cu_2S cage hybrids synthesized without using a primary amine, but there is potential to synthesize the hybrids with further

optimization of trioctylamine as the reducing agent or by using a weaker tertiary amine like triphenylamine. For triphenylamine the electron withdrawing aryl groups would decrease the electron density on the amine and make it a weaker reducing agent. Other potential routes to water soluble hybrid Cu_2S-metal hybrid nanocrystals are proposed in section 5.4 of this thesis.

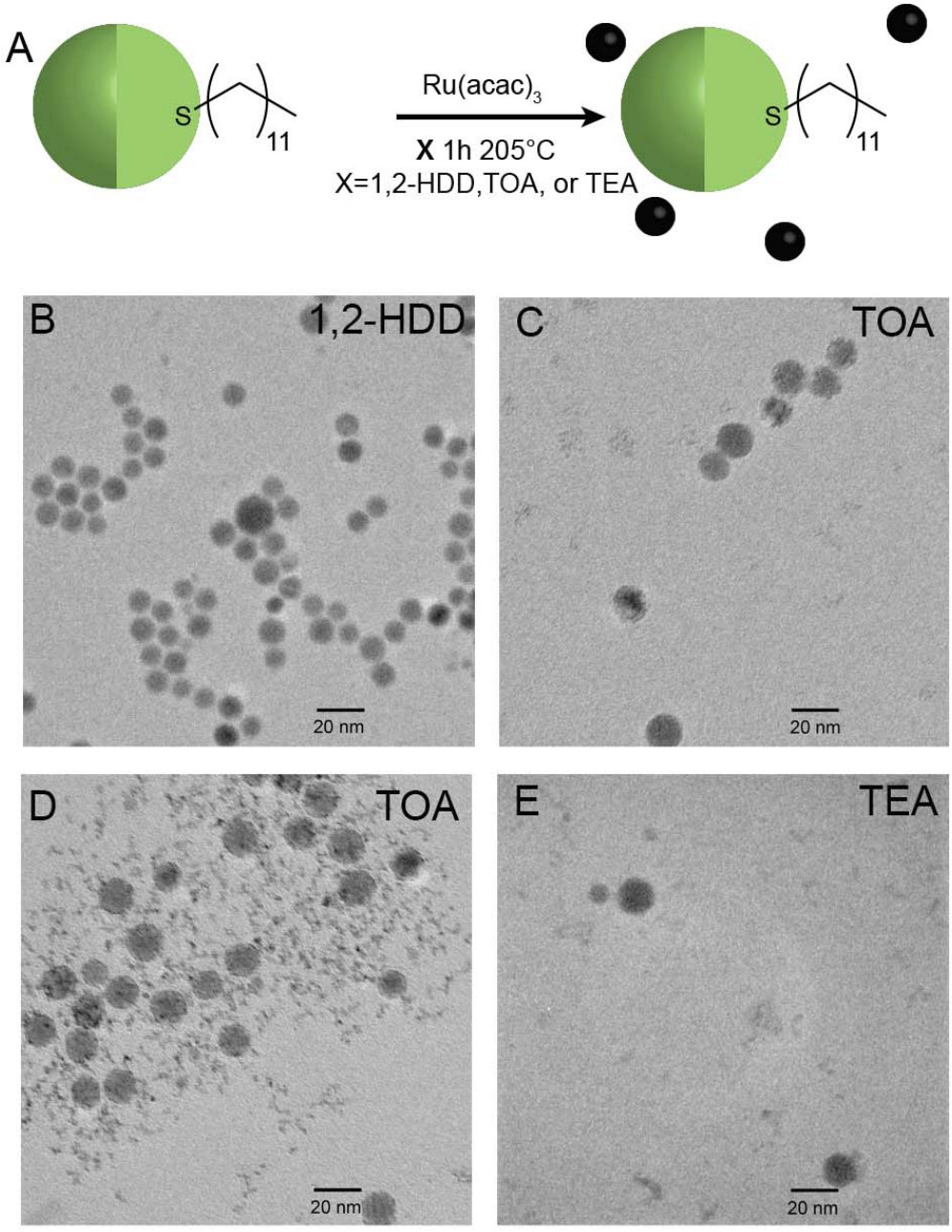

Figure 5.5: (A) Scheme for the synthesis of Cu_2S-Ru hybrid nanocages with DDT capped Cu_2S using different reducing agents. (B) TEM of the resulting product when 1,2-HDD was used as the reducing agent. (C) TEM of the resulting product when TOA was used as the reducing agent. (D) TEM of the resulting product when a stoichiometric amount of TOA was used as the reducing agent. (E) TEM of the resulting product when TEA was used as the reducing agent.

5.2.2 Cu_2S nanorods by oriented attachment

Nanorods are important structures of nanocrystals for light absorption applications. The number of unit cells of a nanocrystal determines the total light absorption of the individual crystal. The control over the diameter can still result in quantum confinement of the nanocrystal, maintaining control over the band gap. To date there have been two methods for the synthesis of nanorods of Cu_2S a direct synthesis procedure using *tert*-dodecane mercaptan (*t*-DDT)[42] and from cation exchange from CdS nanorods.[136] Cation exchange is a useful synthetic tool for the synthesis of otherwise unobtainable morphologies of nanocrystals, and to date, this is the case for quantum confined Cu_2S nanorods.[135] Owing to the well defined synthesis of CdS nanorods a great deal of control over the final nanostructure can be obtained. Cation exchange, however, is limited by poor atom economy and use of Cd.[135]

In the direct synthesis of the Cu_2S nanorods, reported by Kolney-Oleziak *et al.*, *t*-DDT acts as the sulfur source.[42] *T*-DDT is more reactive than DDT resulting from a greater number of β-hydrogens. This leads to a lower decomposition temperature and increased rate of decomposition of the C-S bond, which would be even further enhanced on the metal-rich (002) facets. As a result, using *t*-DDT as the sulfur source for the synthesis of Cu_2S, causes initially spherical 10 nm Cu_2S nanocrystals that grow into nanorods.[42] The formation of the initial spherical nanocrystal causes this method only to allow for control over the length of the rod, not the diameter with a minimum diameter reached of 9 nm. As a result, the direct synthesis of Cu_2S nanorods with *t*-DDT does not allow for quantum confined nanorods and the oriented attachment mechanism presents a path to address this challenge.

In our oriented attachment mechanism of Cu_2S individual nanocrystals attach along the (001) axis forming Cu_2S nanorods. The synthetic procedure involves the heating Cu_2S nanocystals capped with crystal-bound thiols to 220°C in dioctyl ether with 1,2-hexadecanediol (Figure 5.6). The initial hypothesized mechanism for the rod formation is the selective removal of the crystal-bound thiols off the (002) facet and the attachment of the particles to lower the surface energy.

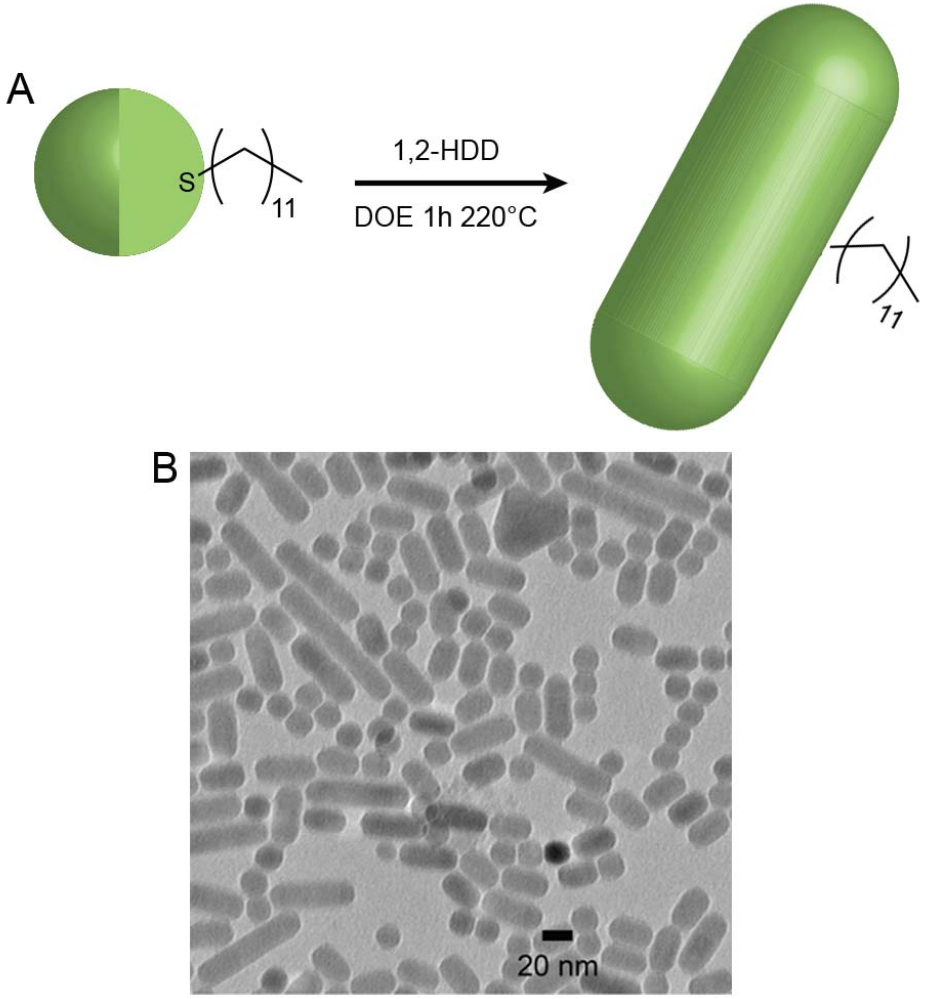

Figure 5.6: (A) Scheme for the synthesis of Cu_2S nanorods with D3MP capped Cu_2S at 220°C. (B) TEM of the resulting Cu_2S nanorods.

Currently in our laboratory, there is ongoing research on this topic by Evan Robinson. He is determining the influence of the surface chemistry and the role of the 1,2-hexadecanediol on the rod formation. One of the opportunities of the oriented attachment mechanism is the potential to control the width of the nanorods by controlling the size of the seed Cu_2S nanocrystals. Such control of the diameter Cu_2S nanorods has not been accomplished without using cation exchange.[71] The concept may be limited by the availability of different facets at different sizes. It could be the case that for the spherical Cu_2S seeds below 9 nm there is not the presence of different facets that allow for the formation of quantum confined Cu_2S nanorods. This oriented attachment mechanism may also be applicable to the other mixed Cu-sulfide nanocrystals.

5.3 Conclusion

In this chapter I explored, the role crystal-bound ligands can play in acting as a template for the synthesis of nanocrystals of increasing complexity. For crystal-bound DDT capped Cu_2S nanocrystals when heated to 205°C selective removal of the edge site ligands is observed and can be used to synthesize Cu_2S-Ru hybrids. When extending the Ru cage formation to D3MP capped particles the ester group decreases the electron density on the alpha carbon slowing the rate of the alkyl migration step need to cleave the ligands. As a result, to synthesize Cu_2S-Ru cage hybrids with D3MP capping ligands the reaction temperature needs to be increased to 220°C. The cage hybrids with D3MP capping ligands were unable to undergo hydrolysis because of the formation of an amide in place of the ester, preventing hydrolysis.

The preferential removal of crystal-bound ligands also can be used to synthesize nanorods. If the Cu_2S nanocrystals are heated to 220°C in the presence of 1,2-HDD oriented

attachment of the seed nanocrystals is observed. There is ongoing work in the lab to determine the role of the 1,2-HDD. Currently, work by Evan Robinson suggests that role is as a dynamic stabilizing agent. The work presented in this chapter highlights the use of crystal-bound ligands to selectively block surfaces allowing for controlled assembly of nanomaterials.

5.4 Future Work

There is potential in synthesize hybrids semiconductor-metal nanoparticles with crystal-bound capping ligands. The increased stability of the organic ligand coordination would make these systems ideal for photocatalysis by avoiding the undesirable oxidative removal of the thiol capping ligands.[57] Using insights from the work discussed in this chapter, there are two potential paths to making Cu_2S hybrids with crystal-bound ligands for photocatalysts.

One of the approaches that may allow for the synthesis of Cu_2S-Ru cage hybrids is to use a new ligand with a different protecting group that is resistant to the presence of primary amines (Figure 5.8). The most likely potential functional group is an alkene. During my time in graduate school I mentored two undergraduates, Samantha Monk and Laura Mast, who worked on utilizing metathesis to functionalize a ligand chain containing a double bond to yield water soluble nanoparticles. Our work on this was limited by the use of iron oxide nanoparticles where decomposition of the capping ligand can occur during the synthesis;[137] however, other groups have shown that this approach works on functionalizing nanoparticles of Au[138] and CdSe.[139] Therefore, this approach may work for the synthesis of the nanocages.

For Cu_2S-Ru cage hybrid system, the use of the alkene is however limited by a significant roadblock: the availability of the thiol. One advantage of D3MP as a replacement for DDT is the ease of preparation of D3MP from cheap and readily available starting

materials.[9] The Fisher esterification used for the synthesis is a one step easily scalable reaction that can be purified by vacuum distillation, and currently in our lab we produce D3MP on a large scale. 10-Undecene-1-thiol would be the potential alkene thiol used.[113] The synthesis of 10-undecene-1-thiol, is a two step reaction from the significantly more expensive 11-bromo-1-undecene. Briefly, The first step involves converting the alkene bromide to S-(undec-10-en-1-yl) ethanethiolate. The resulting product can then be reduced with $LiAlH_4$ to yield the desired 10-undecene-1-thiol.[113] The overall synthesis would be time consuming and would have to be done on a large scale considering that 5 mL of thiol is needed for one Cu_2S seed synthesis. Using 10-undecanethiol the Cu_2S seeds can be synthesized at 200°C, resulting in the ligand shell being functionalized with a terminal alkene. These Cu_2S seeds can be reacted with $Ru(acac)_3$ in octadecylamine at 205°C to yield the Cu_2S-Ru cage hybrids with the terminal alkene intact. To obtain water soluble hybrids a metathesis reaction with acrylic acid will replace the terminal alkene with a carboxylic acid (Figure 5.7).[139] If solubility of the acrylic acid limits the reaction acrylate can be used followed by a hydrolysis to yield the water soluble particles.

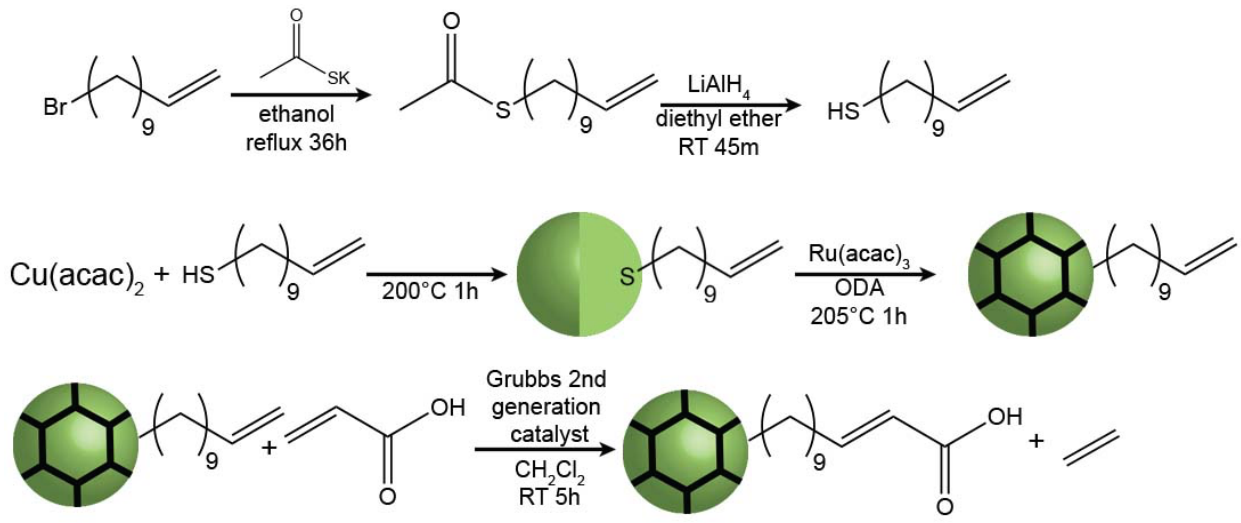

Figure 5.7: Scheme 1 for the total synthesis of water soluble Cu_2S metal hybrid nanoparticles yielding Ru cage hybrids. In the first step 1-bromo-10-undecene is reacted with potassium thioacetate in refluxing ethanol for 36h. The resulting product is then slowly added to a solution of $LiAlH_4$ in diethyl ether at 0°C and then reacted at room temperature for 45m to yield 10-undecene-1-thiol. $Cu(acac)_2$ is then reacted in neat 10-undecane-1-thiol to yield Cu_2S nanocrystals capped with ligands with terminal alkenes. The Cu_2S-Ru cage hybrids can be made by reacting the Cu_2S nanocrystals with $Ru(acac)_3$ in octadecylamine at 205°C for 1h. To make the hybrids water soluble a cross-metathesis reaction with acrylic acid using Grubbs 2nd generation catalyst in dichloromethane at room temperature for 5h. This reaction can be performed under static vacuum to drive off the ethylene side product.

The second approach will build off the oriented attachment work (Figure 5.8). The role of the 1,2-HDD is as a dynamic stabilizing agent, where at increased amounts no attachment/growth is observed. In the synthesis of Pt-semiconductor hybrids, 1,2-HDD plays a different role, as a reducing agent. Using an excess of 1,2-HDD at 220°C may result in the deposition of Pt domains on the exposed facets resulting the formation of the Cu_2S-Pt hybrids.[7] There is concern that the excess HDD and the slight increase in temperature, from 210°C to 220°C, will increase the rate of Pt deposition potentially resulting in nucleation of free Pt nanoparticles in addition to the hybrids. These free Pt nanocrystals would have to be separated by size selective precipitation. This procedure allows for the primary amines to be avoided for the hybrid synthesis and our established D3MP hydrolysis can yield water-soluble hybrids. If

the hybrids can be synthesized using one of the two described methods, the synthesized hybrids would be tested for photocatalytic water reduction.

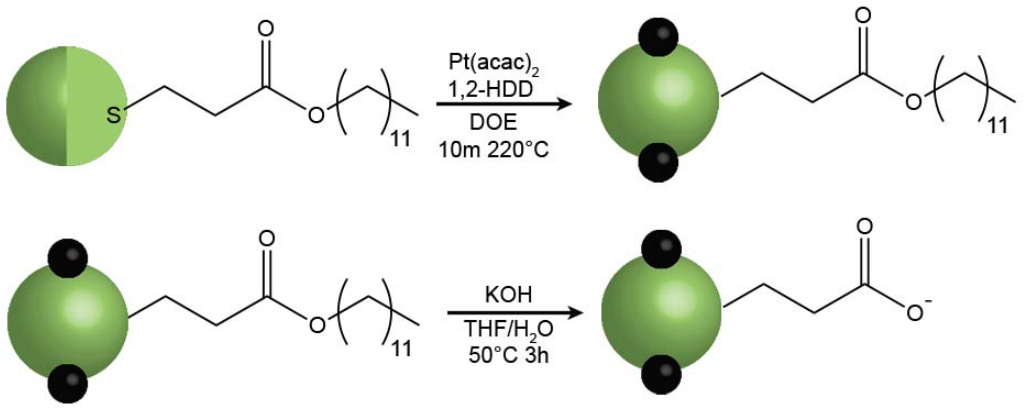

Figure 5.8: Scheme 2 for the total synthesis of water soluble Cu_2S metal hybrid nanoparticles with Pt domains on the (002) facets. D3MP capped Cu_2S nanocrystals are treated with $Pt(acac)_2$ and 1,2-HDD in DOE at 220°C for 10m. At 220°C the selective removal of the crystal-bound ligands from the (002) facet will result in the deposition of the Pt on the exposed facets. The ester functional group of the D3MP capping ligands can then be hydrolyzed to result in water soluble Cu_2S-Pt hybrid nanoparticles.

5.5 Experimental Methods

Materials: Octadecylamine (ODA, 90%), dioctyl ether (DOE, 99%), and 1,2-hexadecanediol (1,2-HDD, 90%) were obtained from Sigma Aldrich. $Ru(acac)_3$ (99%) was obtained from Strem. All chemicals were used as received.

Copper (I) sulfide nanocrystals with crystal-bound DDT: Preparation of copper(I) sulfide with DDT capping ligands was discussed in Chapter 2, see page 43 for details.

Dodecyl 3-mercaptopropanoate (D3MP): Preparation of dodecyl 3-mercaptoproponate was discussed in Chapter 2, see page 46 for details.

Copper (I) sulfide nanocrystals with crystal-bound D3MP: Preparation of copper(I) sulfide with D3MP capping ligands was discussed in Chapter 2, see page 46 for details.

Ruthenium-copper(I) sulfide hybrids[68]*:* 2 g of ODA was degassed in a three neck flask by vacuum for 30 min. Cu_2S seeds in $CHCl_3$ (75 μmol of Cu^{1+} as determined by neocuproine) were added in the glove box. The flask was then returned to the Schlenk line where the $CHCl_3$ was removed by vacuum for 1 hour. The solution was heated to 207.5°C. Meanwhile, in a syringe heated by a custom heating mantle, 1 ml of a 5 mmol solution of $Ru(acac)_3$ in dioctyl ether was heated to 215°C. The $Ru(acac)_3$ solution was quickly injected. The reaction was left to react for 1 hour at 205°C. Particles were precipitated and washed with warm 2-propanol. The resulting black precipitate was dispersed in $CHCl_3$ and centrifuged, collecting the supernatant. The procedure was modified for the Cu_2S seeds capped with the ester ligand by changing the reaction temperature to 220°C.

Copper(I) sulfide nanorods: 3 ml of DOE and 50 mg of HDD was degassed in a three neck flask by vacuum for 30 min. Cu_2S seeds in $CHCl_3$ (75 μmol of Cu^{1+} as determined by neocuproine) were added in the glove box. The flask was then returned to the schlenk line where the $CHCl_3$ was removed by vacuum for 1 hour. The solution was heated to 220°C. The reaction was left to react for 1 hour at 220°C. Particles were precipitated and washed with warm 2-propanol. The resulting black precipitate was dispersed in $CHCl_3$ and centrifuged, collecting the supernatant.

CHAPTER VI

CONCLUSION

6.1 Summary of Thesis

The ongoing theme of my thesis has been the surface chemistry of semiconductor nanocrystals. Specifically, that the synthetic methodology used to prepare the nanocrystals can lead to different modes of surface coordination. By fundamentally understanding these surfaces, nanocrystal-based systems can be designed and synthesized to target specific applications.

As a laboratory, we became interested in this topic because we and others had noticed that ligand exchange on the surface of Cu_2S and $CuInS_2$ was hindered when primary thiols were used as the sulfur source in the synthesis. In Chapter 2, I addressed this challenge by performing surface analysis on Cu_2S nanocrystals synthesized using dodecanethiol and samples prepared without any thiols.[9] Using NMR, XPS, and TGA-MS, I was able to show that there is a difference in the surface chemistry. I attribute this difference to the binding of the DDT into higher coordination number sites on the surface, which we have termed "crystal-bound" ligands. This higher coordination binding is responsible for the inhibited ligand exchange for these nanocrystals.

Since ligand exchange and surface functionalization is important to the application of nanocrystals a procedure was needed to allow for modification of these crystal-bound systems. Also in Chapter 2, I presented my procedure for synthesizing water soluble nanocrystals with crystal-bound ligands.[9] To allow phase transfer, a new thiol ligand was synthesized, dodecyl-3-

mercaptopropionate (D3MP). D3MP has latent functionality through the presence of an ester group in the long alkyl chain. After a nanocrystal synthesis using D3MP, a base hydrolysis can be used to cleave, resulting in the termination of the organic capping ligands with polar carboxylic acid groups, allowing for water solubility. To my knowledge, this was the first time that native ligand modification was used for directly rendering nanocrystals water soluble. This method was shown for Cu_2S and $CuInS_2$ nanocrystals.

In Chapter 3, I expanded the use of crystal-bound ligands to II-VI quantum dot systems. I was able to synthesize a ZnS shell with crystal-bound ligands around a CdSe core.[10] What made this system interesting was that when D3MP was used to induce water solubility there was a change in the optical properties of the system following the ligand hydrolysis. The observed changes were a quenching of the fluorescence quantum yield and a red shift in the peak position while maintaining the full width at half maximum. Through experimental and computational studies it was concluded that the coordination of base to the surface metal sites causes the changes in the optical properties. The same effects were observed for surface-bound thiol capped particles; however, the surface-bound samples also lost colloidal stability, while the crystal-bound samples remained soluble. I was able to exploit the electronic effects of the surface hydroxylation to improve the catalytic degradation of methylene blue.

The techniques used by others and myself for surface analysis does not provide a complete picture the inorganic/organic interface. In Chapter 4, I presented my work towards developing models such that XAS can be used as a direct characterization technique for organic ligand binding at the surfaces of core/shell QDs. My models revealed that the bridging nature of Z-type ligands on a nonpolar surface induce surface defects in the shell resulting from tensile strain. These defects may contribute to the formation of lattice defects in the shell during

growth processes, which can impact the optical properties of the QDs.[120] I also provide a means validate these models spectroscopically with simulated XAS spectra.

In Chapter 5, I discussed my work towards using Cu_2S nanocrystals with crystal-bound ligands for the assembly of hierarchical nanostructures. In the targeted synthesis of nanocrystal systems it is important to understand methods to exchange and remove ligands on the surfaces. By tuning the reaction temperature selective loss of ligands off edges and facets can allow for the synthesis of cage hybrids[68] and nanorods.

6.2 Conclusion and Perspective

Overall, I have studied the nature of ligand coordination of the surfaces of QDs. I have identified a new type of coordination, crystal-bound, that can confer increased stability of the organic capping ligands to exchange and oxidation.[9] By understanding this new coordination, we can begin to design new nanocrystal systems for targeted applications.[10] Some of the most cutting edge research on the surface chemistry of QDs has simplified the surfaces to stoichiometric models.[140] This is an important step; however, I believe there is beauty in this complexity such as edges and faceting. In my opinion, by embracing this complexity, that the true nature of the organic/inorganic interface of QDs can be understood and tuned. To address this concept, I would propose studying the surface chemistry on shape controlled QDs with well defined facets.[141]

As the fundamental understanding of nanocrystal systems grows new and exciting technologies will be developed that has the potential to revolutionize our society. The rational control over surface passivation can lead to improvement and implementation of QD based devices and applications. The insulating nature of the native organic ligands will impact any

charge transfer based application, such as solar cells and photocatalysis.[142] Therefore, in order to fully develop and optimize these applications a complete understanding of the surface chemistry is required. From this perspective it makes sense that light emitting applications such as in display technologies and biological labels are the primary commercial applications for QDs, and I believe this trend will continue with the next major products also avoiding the disruption of the native ligands, such as solar concentrators.[143] However, though the continued study of QD surface chemistry new and exciting technologies will be developed and commercialized.

APPENDIX A

ADDITONAL SURFACE CHARATERIZATION

This Appendix includes the full spectra and characterization of the surface chemistry presented in Chapter 2.

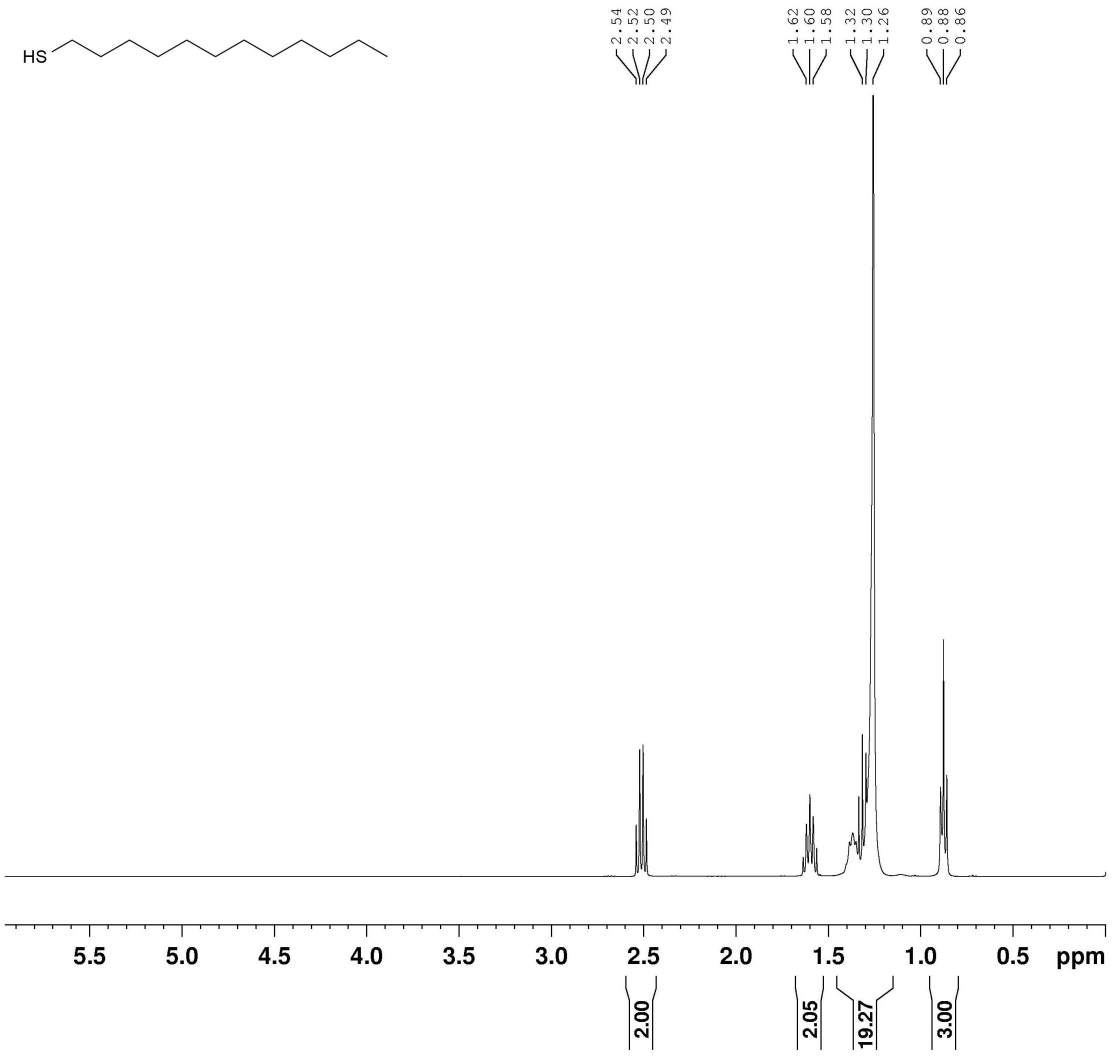

Figure A.1: ^{1}H NMR of 1-dodecanethiol

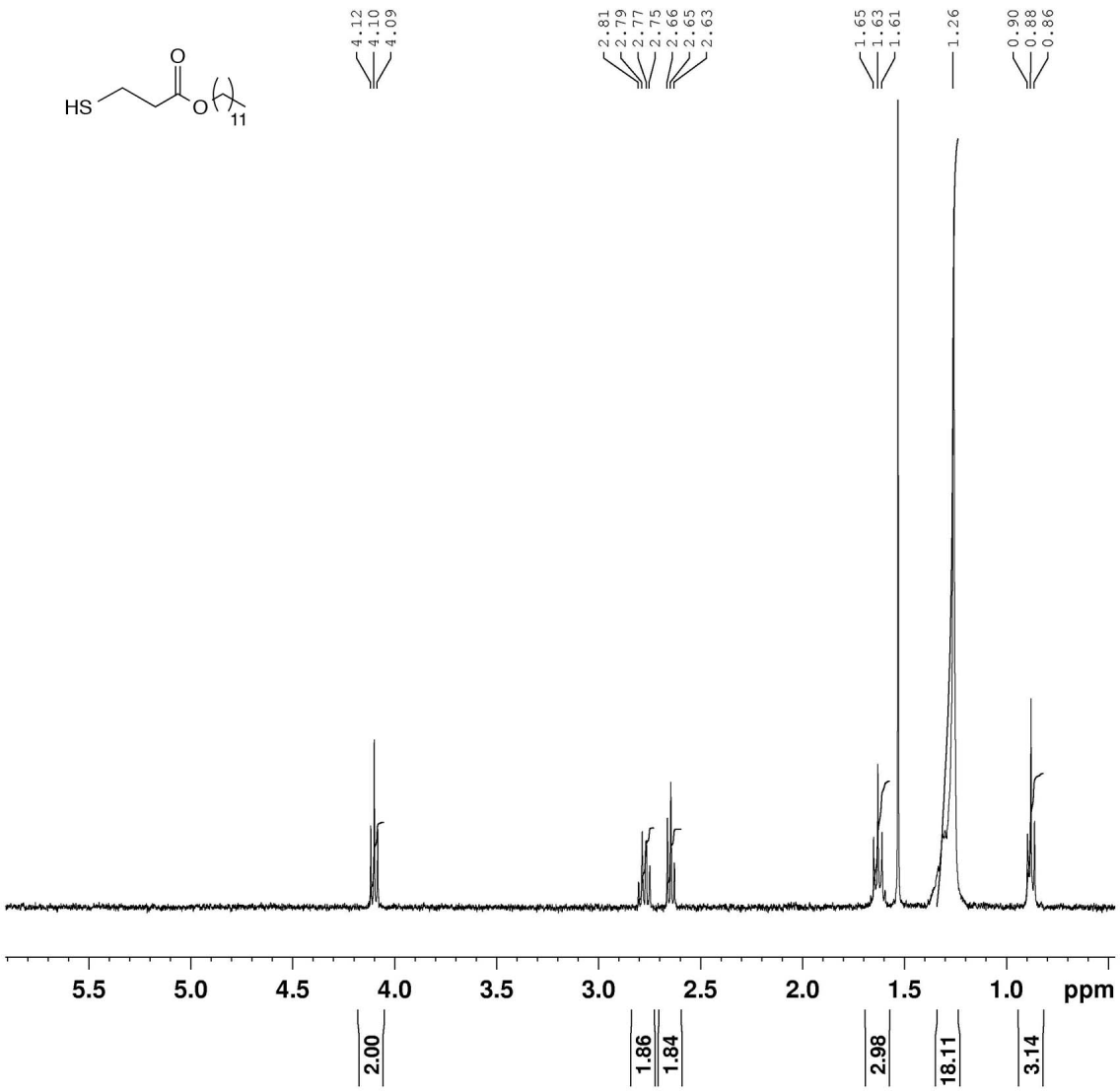

Figure A.2: ^{1}H NMR spectrum of dodecyl-3-mercaptopropionate, 400 MHz

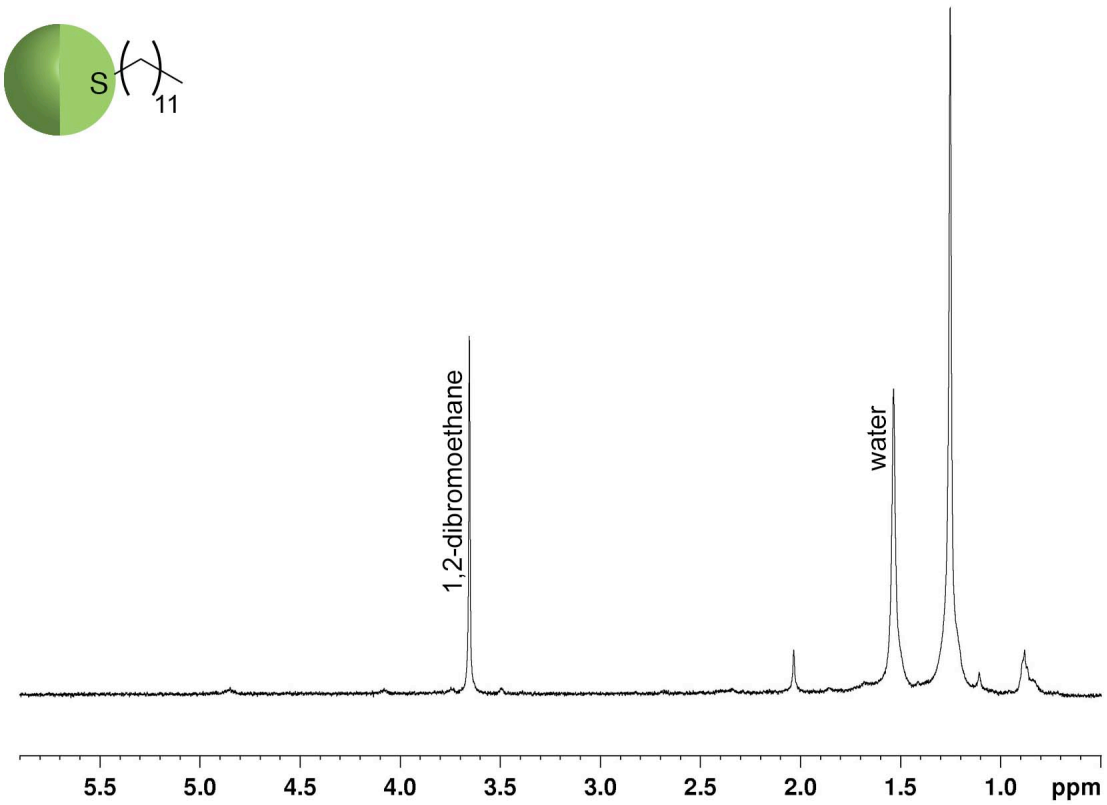

Figure A.3: ^{1}H NMR of Cu_2S with crystal-bound dodecanethiol before the addition of D3MP, 500 MHz.

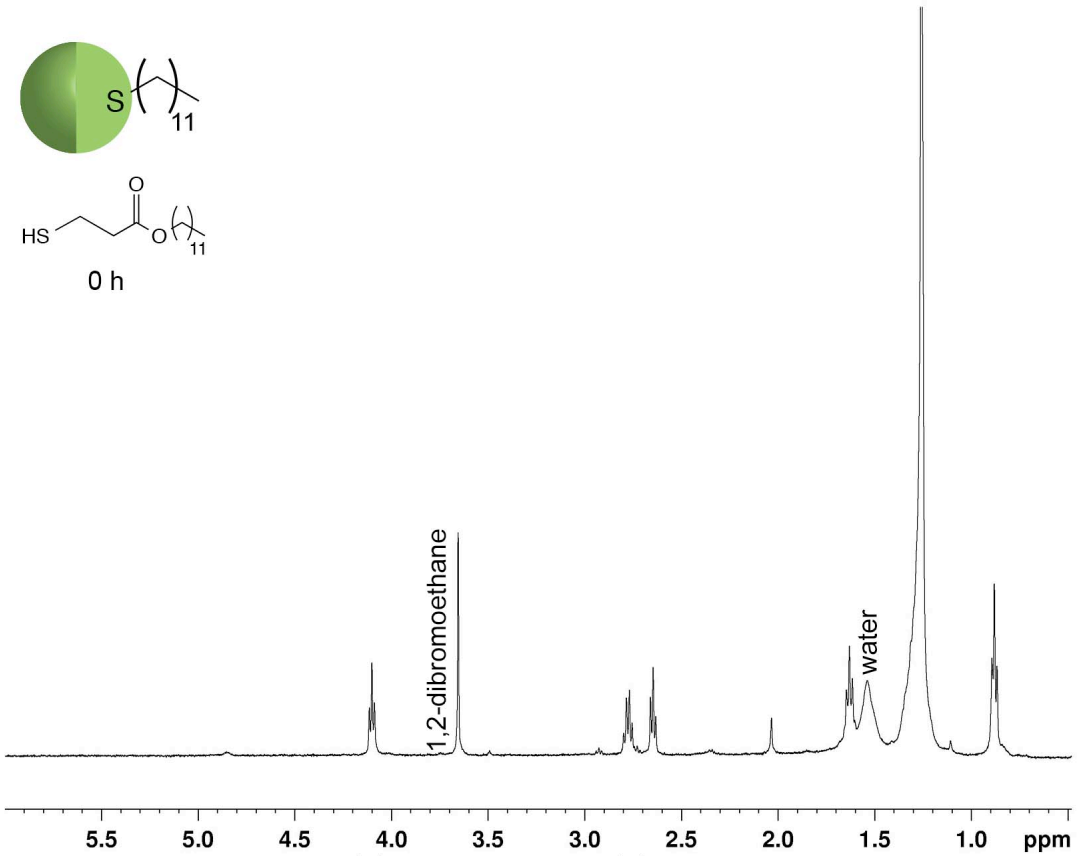

Figure A.4: ^{1}H NMR of Cu_2S with crystal-bound dodecanethiol with dodecyl-3-mercaptopropionate added such that the amount of free ligand is twice the amount of the DDT ligands, 500 MHz.

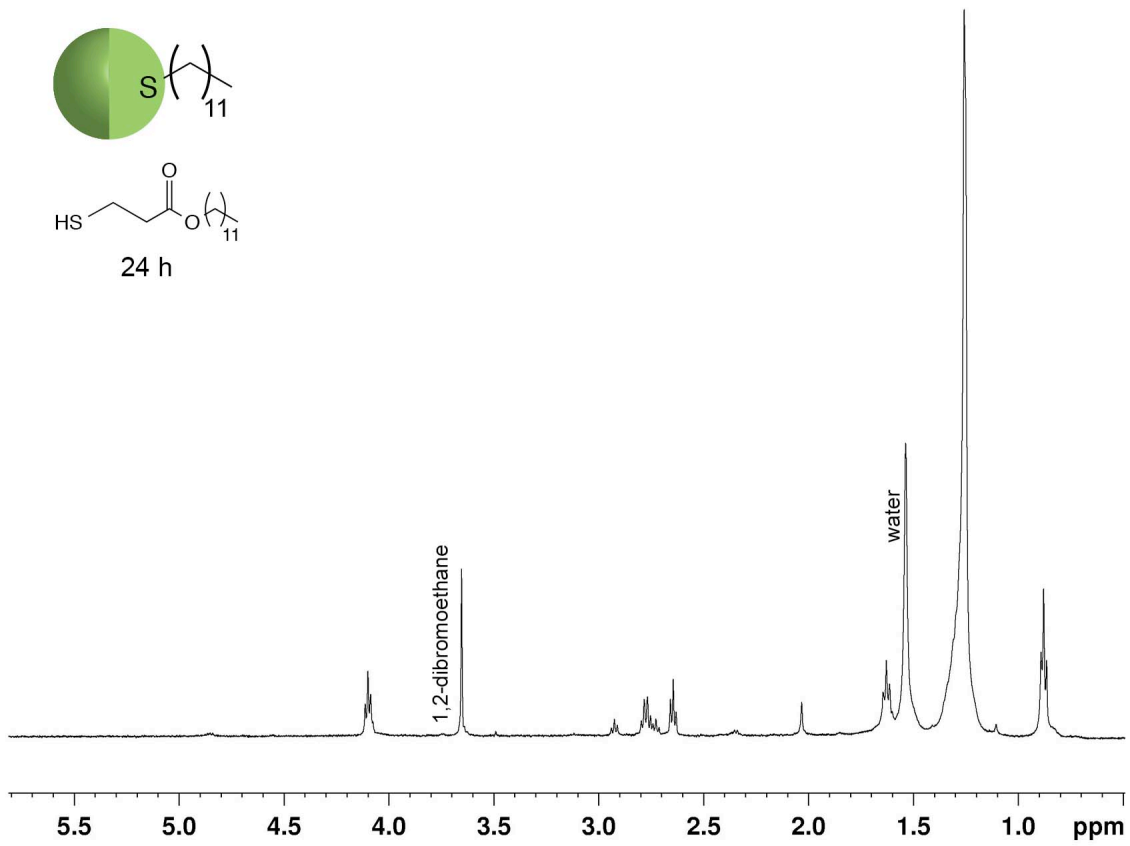

Figure A.5: ^{1}H NMR of Cu_2S with crystal-bound dodecanethiol with dodecyl-3-mercaptopropionate added such that the amount of free ligand is twice the amount of the DDT ligands 24 hours after the addition of the D3MP, 500 MHz.

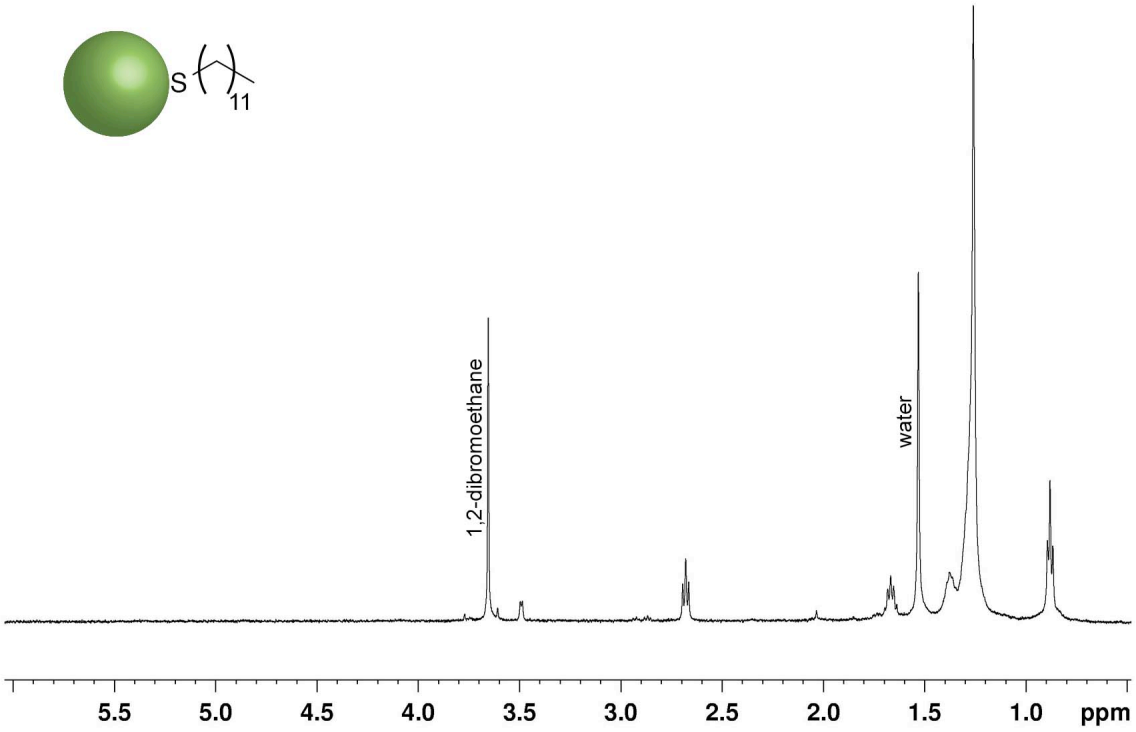

Figure A.6: ^{1}H NMR of Cu_2S with surface-bound dodecanethiol before the addition of D3MP, 500 MHz.

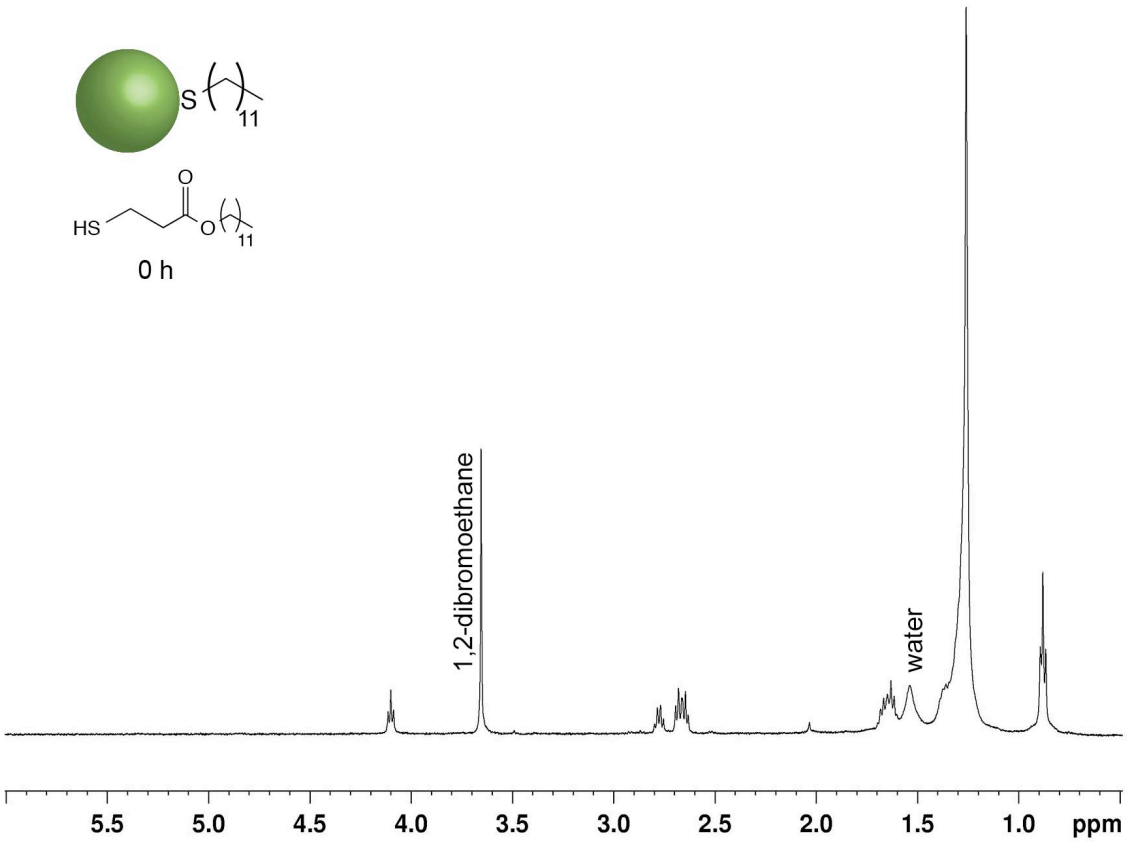

Figure A.7: ^{1}H NMR of Cu_2S with surface-bound dodecanethiol with dodecyl-3-mercaptopropionate added such that the amount of free ligand is twice the amount of the DDT ligands, 500 MHz.

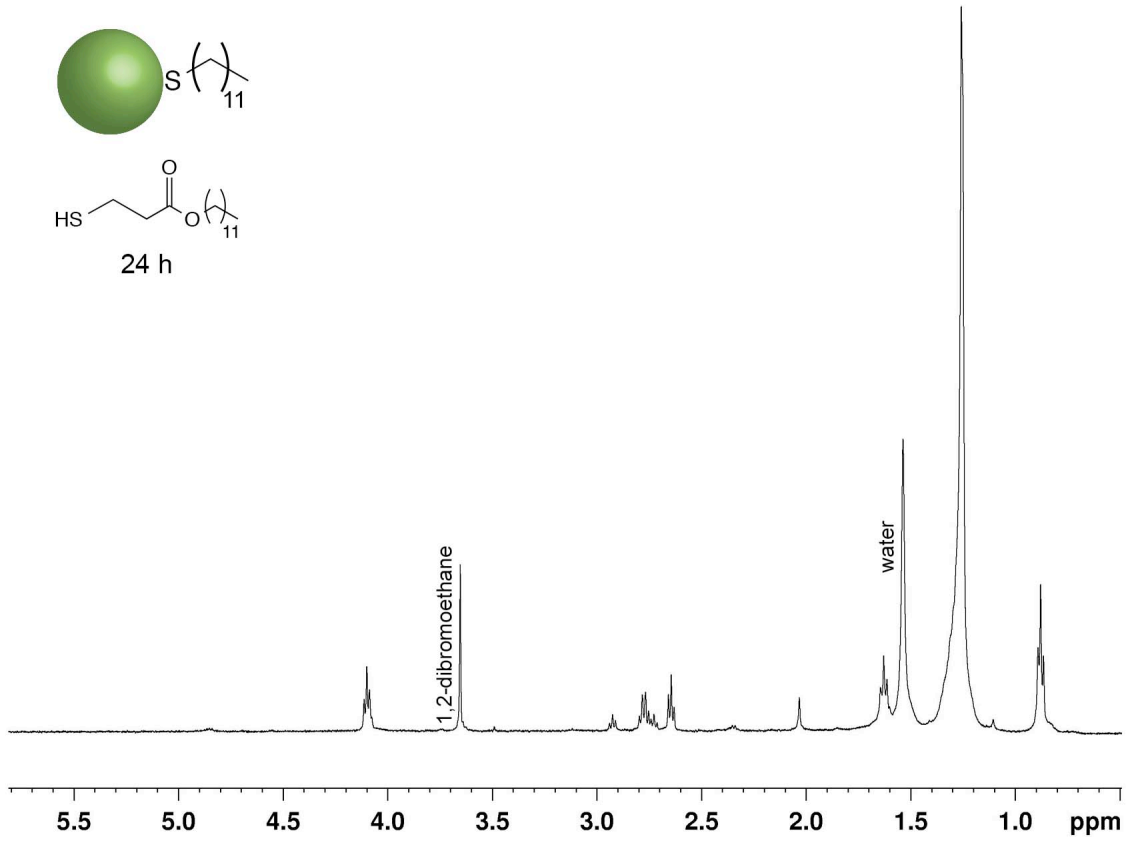

Figure A.8: ^{1}H NMR of Cu_2S with surface-bound dodecanethiol with dodecyl-3-mercaptopropionate added such that the amount of free ligand is twice the amount of the DDT ligands 24 hours after the addition of the D3MP, 500 MHz.

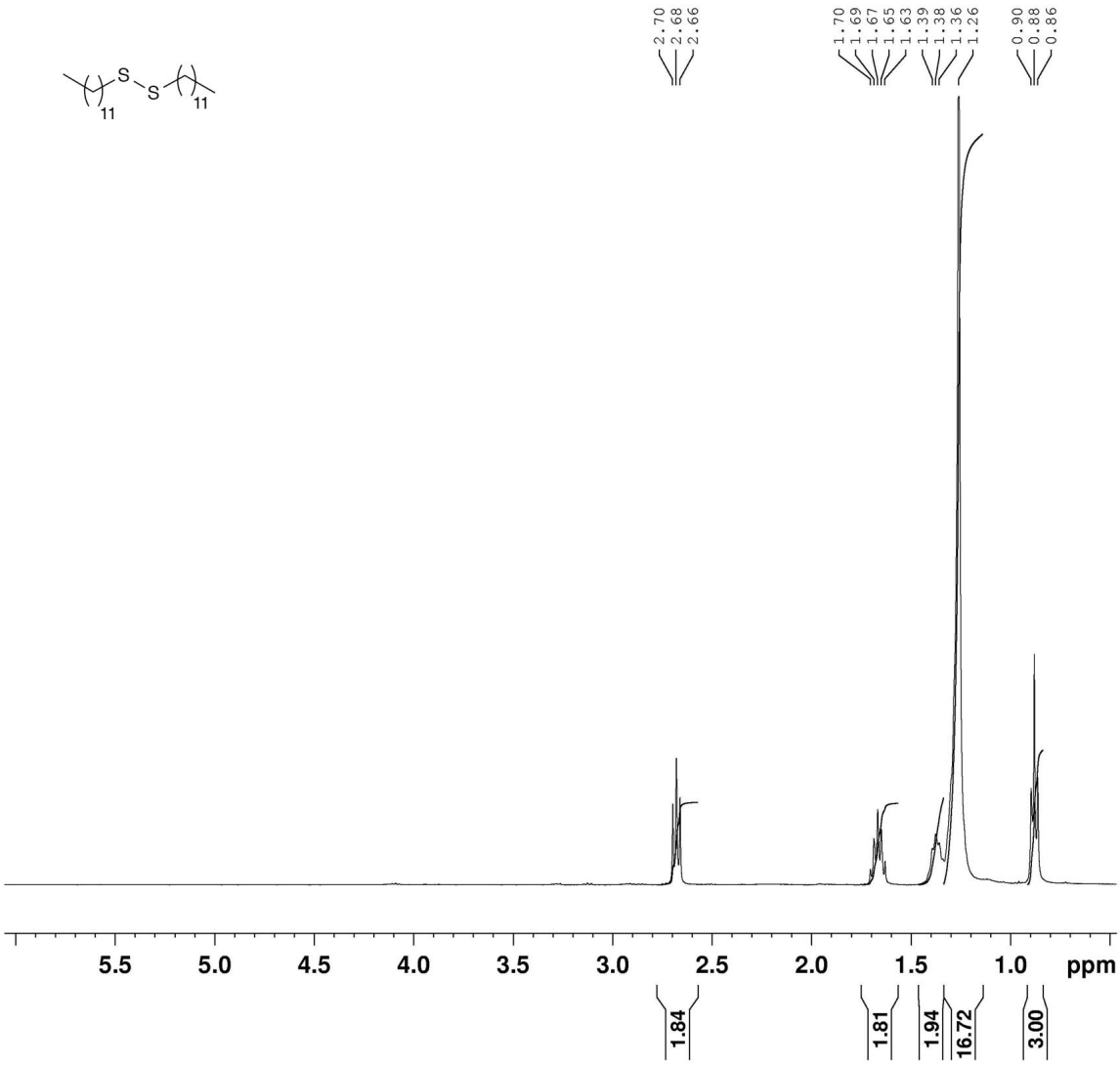

Figure A.9: ^{1}H NMR of 1,1-didodecyldisulfide, 400 MHz

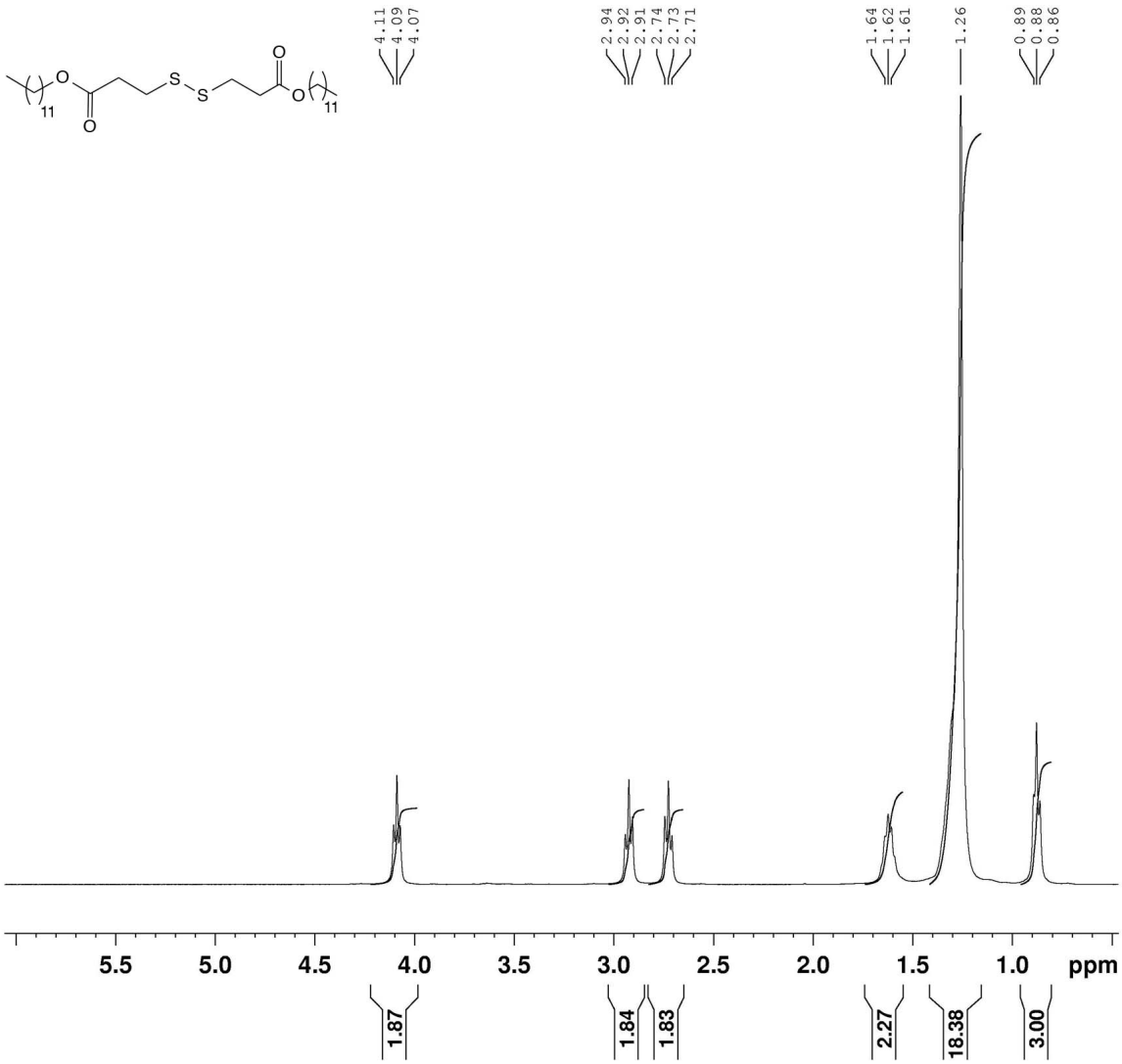

Figure A.10: ^{1}H NMR of didodecyl 3,3'-disulfanediyldipropionate, 400 MHz

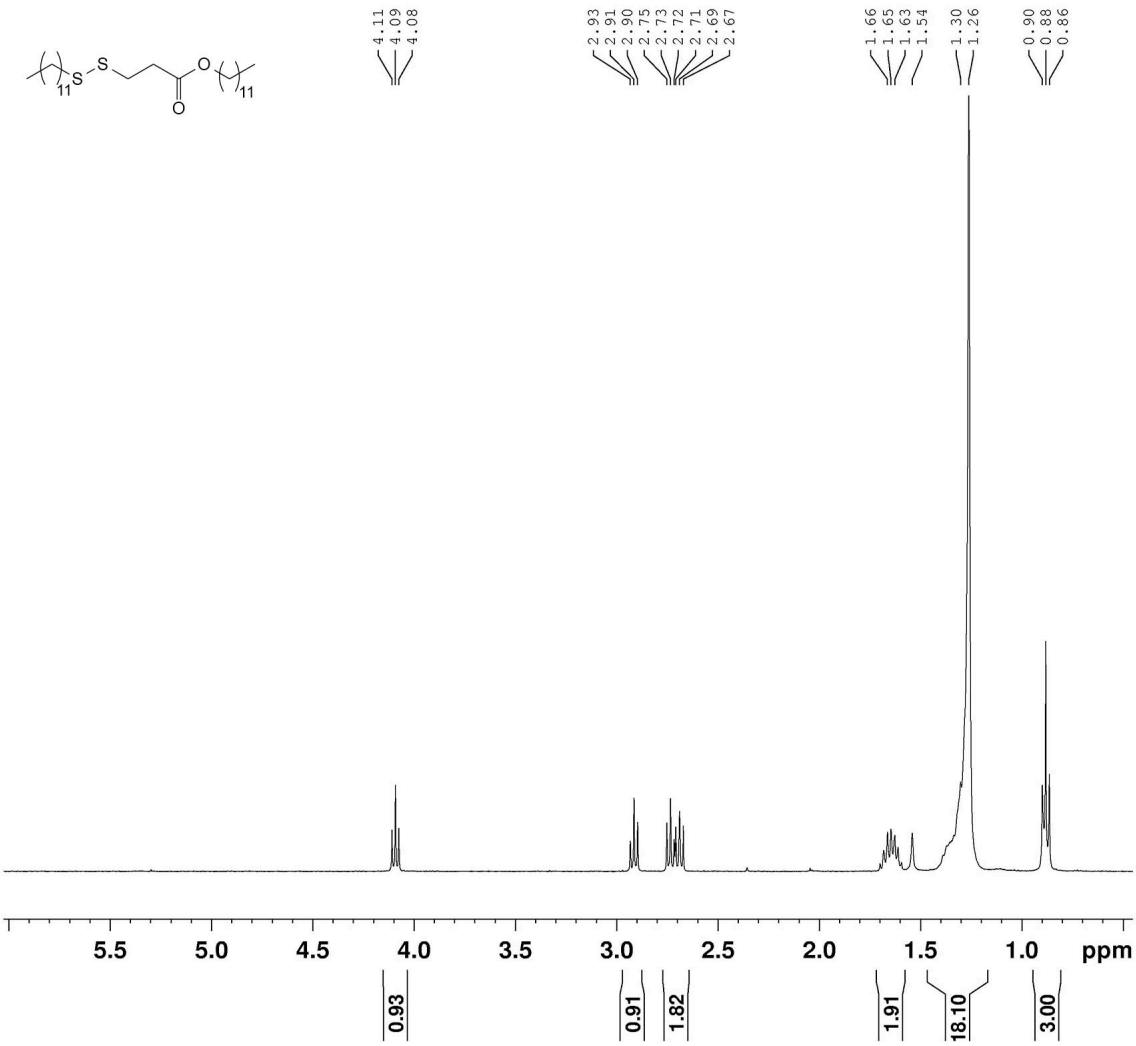

Figure A.11: ^{1}H NMR of dodecyl 3-(dodecyldisulfanyl)propanoate, 400 MHz

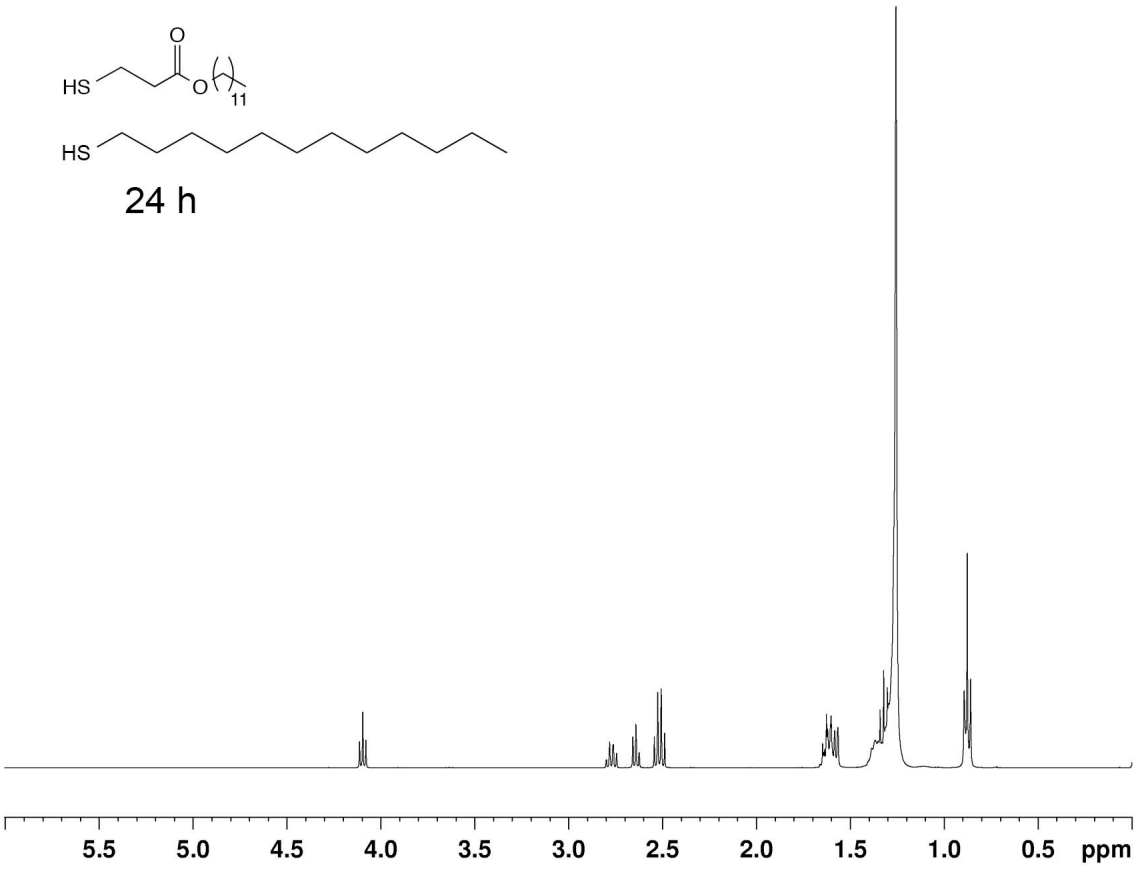

Figure A.12: ^{1}H NMR of dodecyl-3-mercaptopropionate and dodecanethiol combined and exposed to ambient light for 24 hours, 400 MHz, $CDCl_3$. For this control approximately 50 mM of each thiol was used. In the previous experiments with nanocrystals, the concentration of each of the thiols was 1-2 mM. Despite the higher concentrations in this control experiment, no disulfides were observed to form.

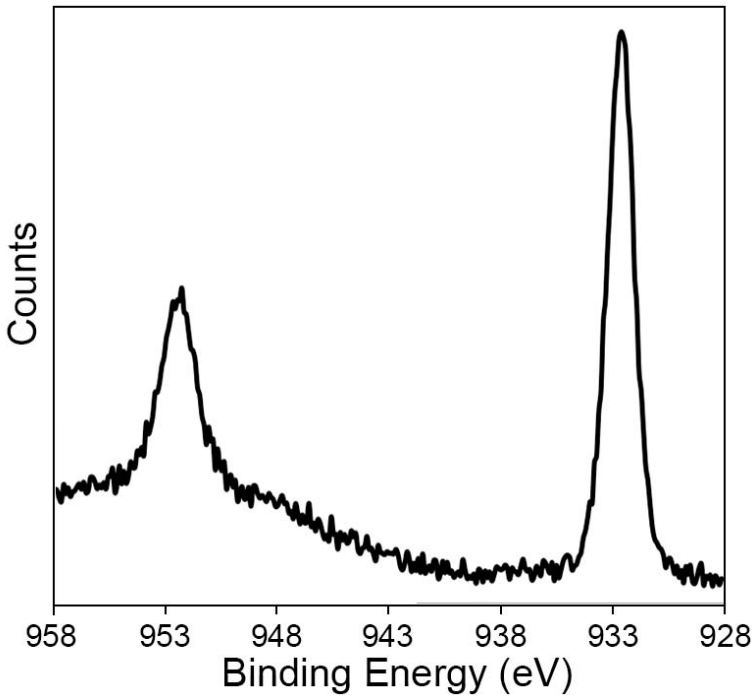

Figure A.13: Cu2p region of the Cu_2S nanocrystals capped with crystal-bound dodecanethiol

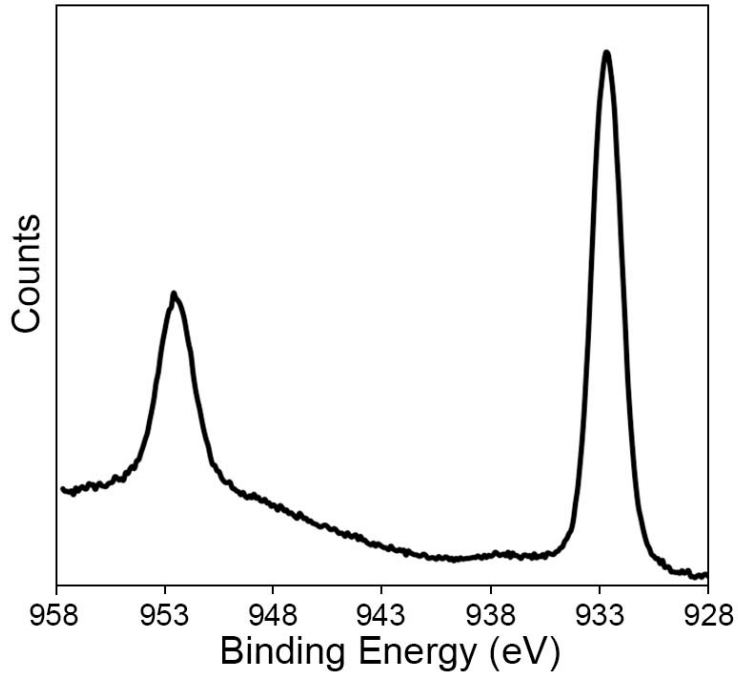

Figure A.14: Cu2p region of the Cu_2S nanocrystals capped with surface-bound dodecanethiol

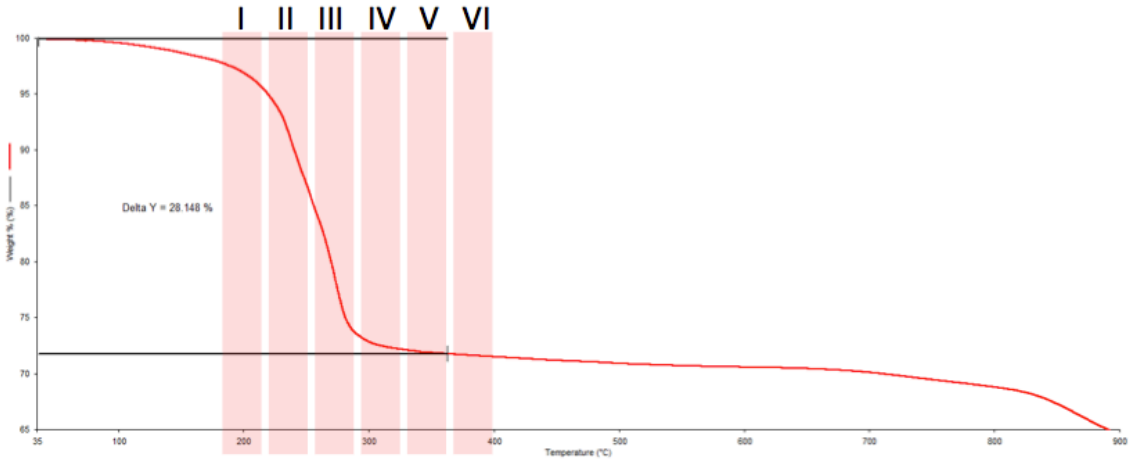

Figure A.15: TGA of Cu_2S capped with crystal-bound dodecanethiol. Highlighted regions were individually sampled by mass spectrometry.

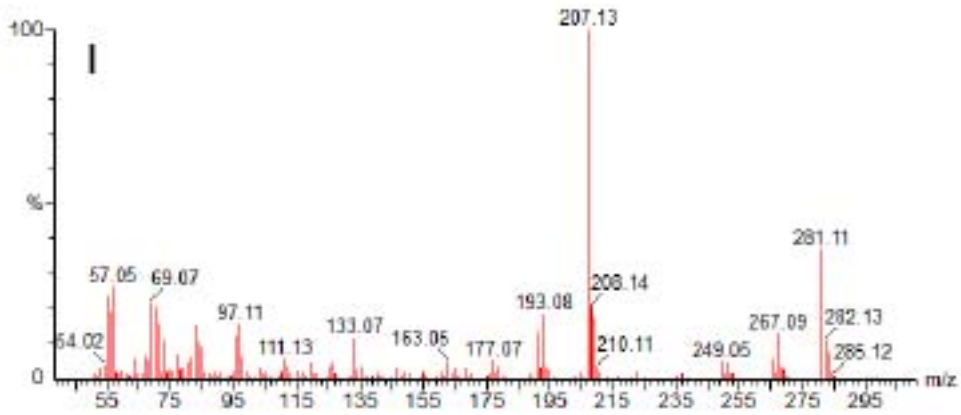

Figure A.16: Mass spectrum of the off gas sampled in region I of Cu_2S with crystal-bound dodecanethiol

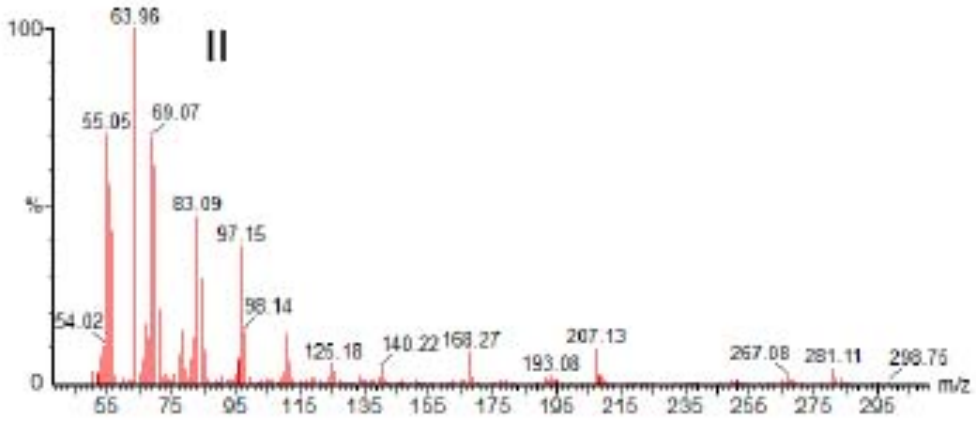

Figure A.17: Mass spectrum of the off gas sampled in region II of Cu_2S with crystal-bound dodecanethiol

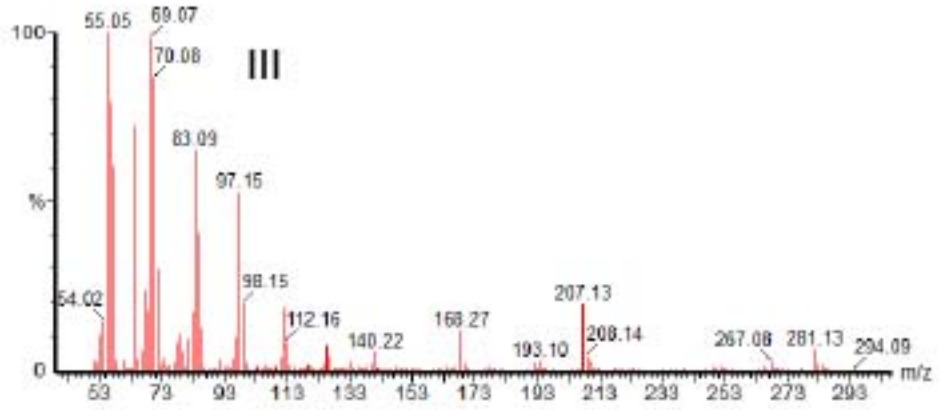

Figure A.18: Mass spectrum of the off gas sampled in region III of Cu_2S with crystal-bound dodecanethiol

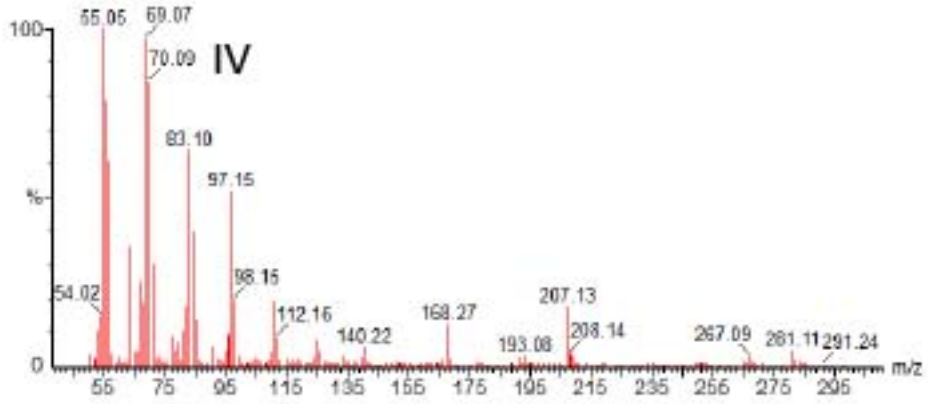

Figure A.19: Mass spectrum of the off gas sampled in region IV of Cu_2S with crystal-bound dodecanethiol

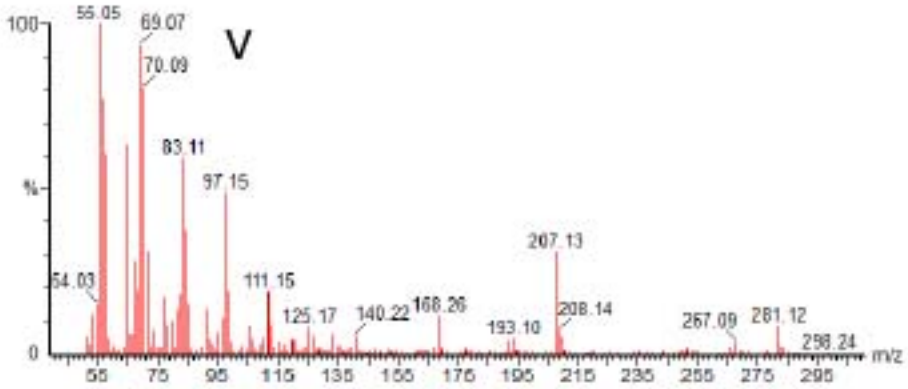

Figure A.20: Mass spectrum of the off gas sampled in region V of Cu_2S with crystal-bound dodecanethiol

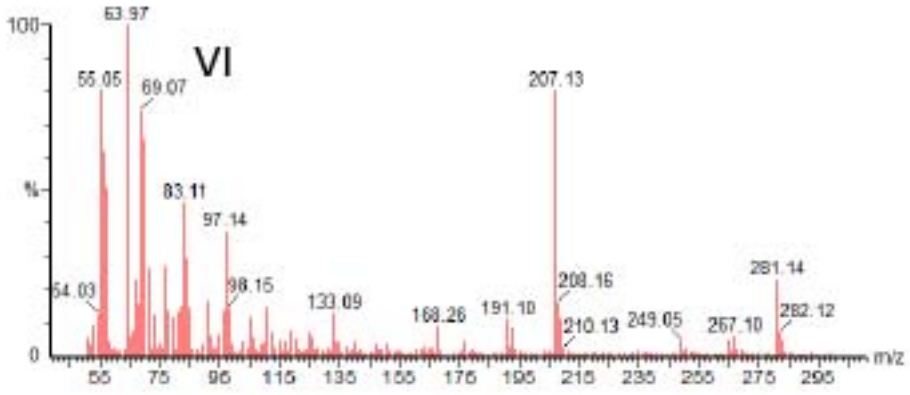

Figure A.21: Mass spectrum of the off gas sampled in region VI of Cu_2S with crystal-bound dodecanethiol

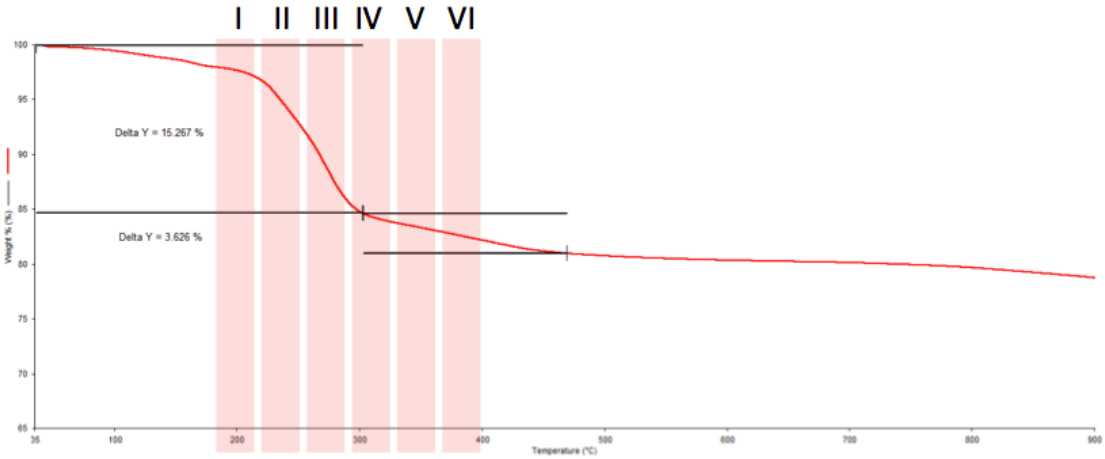

Figure A.22: TGA of Cu_2S capped with surface-bound dodecanethiol. Highlighted regions were individually sampled by mass spectrometry.

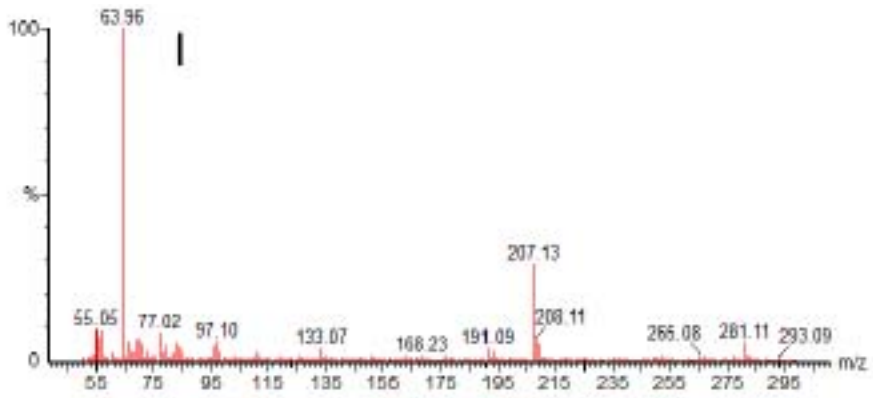

Figure A.23: Mass spectrum of the off gas sampled in region I of Cu_2S with surface-bound dodecanethiol

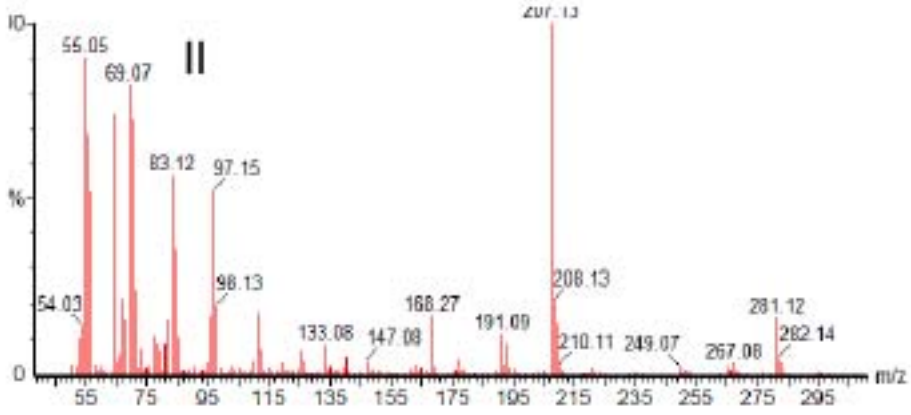

Figure A.24: Mass spectrum of the off gas sampled in region II of Cu_2S with surface-bound dodecanethiol

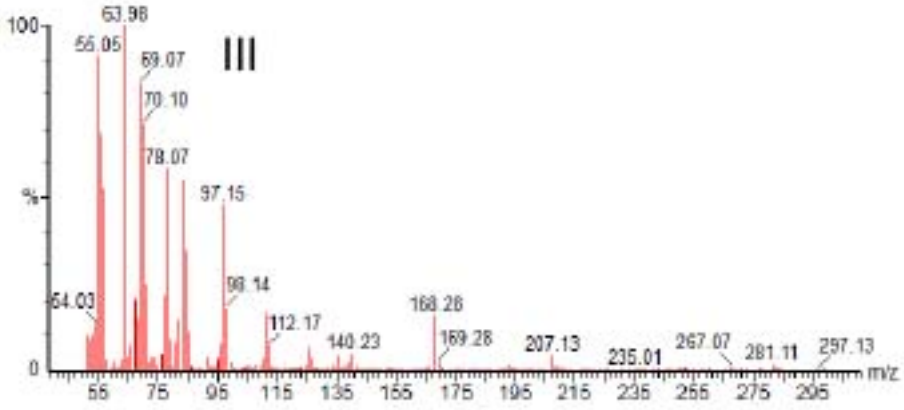

Figure A.25: Mass spectrum of the off gas sampled in region III of Cu_2S with surface-bound dodecanethiol

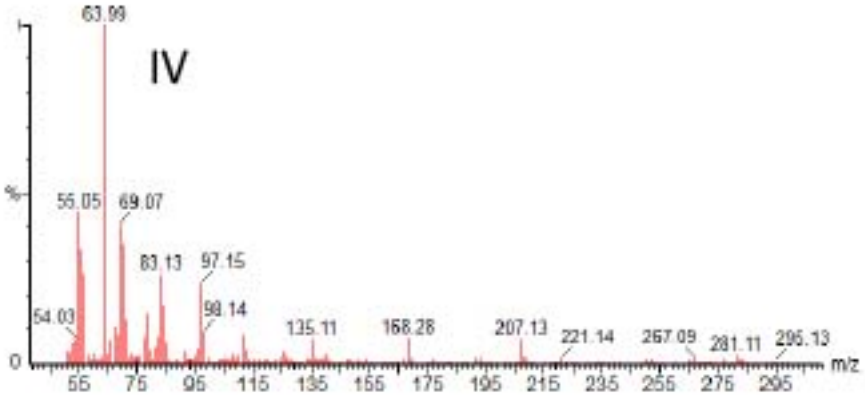

Figure A.26: Mass spectrum of the off gas sampled in region IV of Cu_2S with surface-bound dodecanethiol

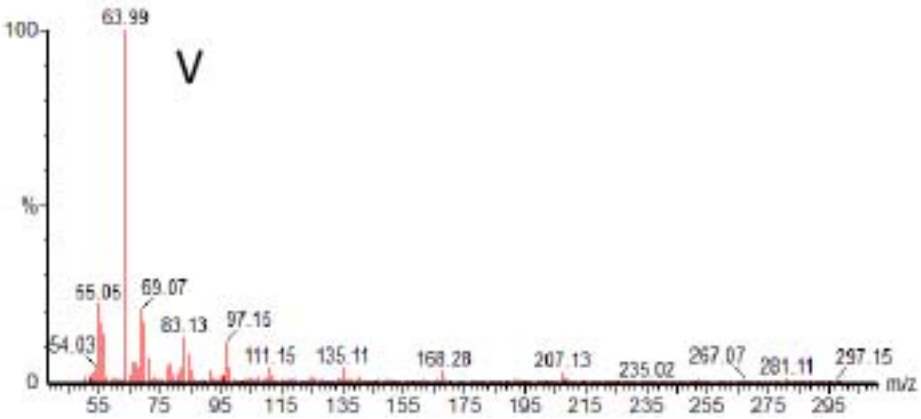

Figure A.27: Mass spectrum of the off gas sampled in region V of Cu_2S with surface-bound dodecanethiol

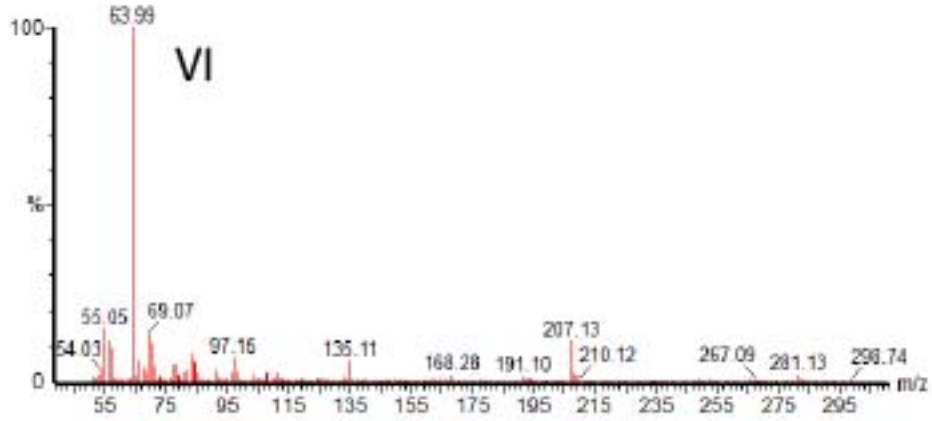

Figure A.28: Mass spectrum of the off gas sampled in region VI of Cu_2S with surface-bound dodecanethiol

$Cu_{2-x}S$ stoichiometry calculations

Free carrier density[67]

The free carrier density was determined by dispersing the Cu_2S in THF directly after hydrolysis.

The bulk plasmon frequency (ω_p) was determined from the peak frequency of the plasmon

(ω_{sp}=0.97 eV). The FWHM of the peak (γ=0.80 eV) was approximated as twice the HWHM at the higher energy because the near-IR solvent cutoff prevented the full plasmon shape to be observed. The dielectric constant (ε_m) of THF is 7.2:

$$\omega_{sp} = \sqrt{\frac{\omega_p^2}{1+2\varepsilon_m} - \gamma^2} \quad \text{(A.1)}$$

The bulk plasmon frequency was determined to be 4.93 eV. The density of free carriers(N_h) can be determined, using the charge of an electron (e), permittivity of free space (ε_0), and the effective mass of the hole (m_h, for Cu_2S=0.8m_0):

$$\omega_p = \sqrt{\frac{N_h e^2}{\varepsilon_0 m_h}} \quad \text{(A.2)}$$

N_h=3.56 × 10^{20} cm^{-3}

The calculation was also used for $CuInS_2$[72] after hydrolysis (ω_{sp}=0.88 eV, γ=0.67) in ethanol (ε_m=24.3). Using the effective mass of the hole in $CuInS_2$ as 1.3m_0, the free carrier density was determined to be 1.44 × 10^{21} cm^{-3}.

Copper deficiency:

The chalcocite unit cell has 96 Cu atoms and 48 S atoms with a volume of 2.42 x 10^{-21} cm^3.[144] Using these parameters the number of free carriers per unit cell can be

$$\frac{Free\ carriers}{unit\ cell} = N_h \times V_{unit\ cell} \quad (3)$$

Therefore the post hydrolysis $Cu_{2-x}S$ has 0.86 free carriers/unit cell. Using the approximation that one free carrier is equal to 1 missing Cu^{1+} the number of Cu atoms in the unit cell can be determined:

$$Number\ of\ Cu\ atoms = 96 - \frac{free\ carriers}{unit\ cell} \quad (4)$$

A unit cell of the post hydrolysis Cu_2S contains 95.14 Cu atoms

$$Cu_{2-x}S\ Stoichiometry = \frac{Number\ o\square\ Cu\ atoms}{Number\ of\ sulfur\ atoms} \quad (5)$$

$Cu_{2-x}S$=$Cu_{1.98}S$

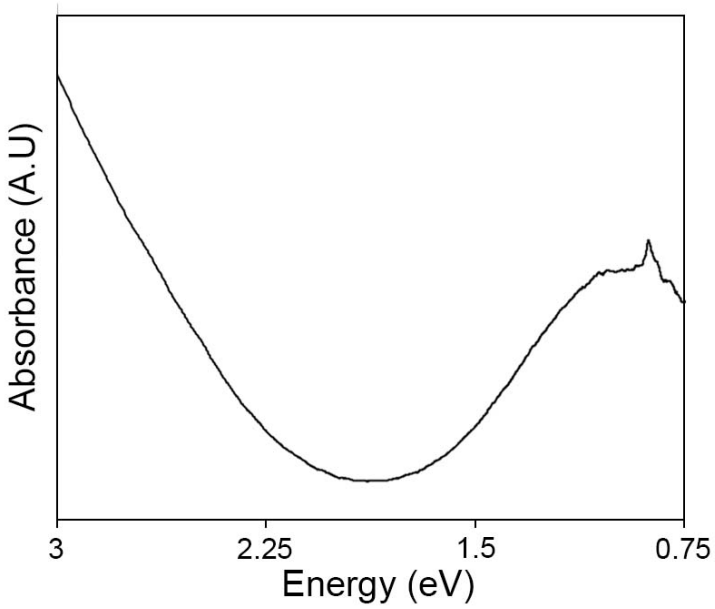

Figure A.29: Absorbance spectrum of Cu_2S capped with crystal-bound D3MP after hydrolysis dissolved in THF.

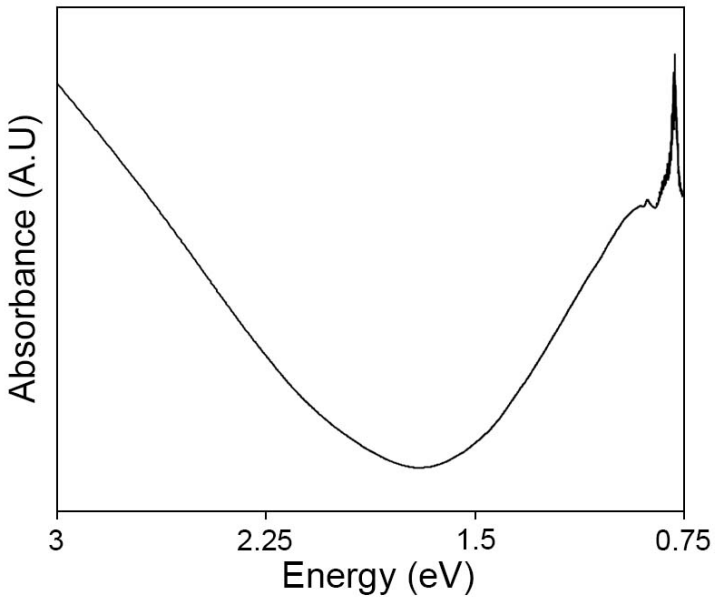

Figure A.30: Absorbance spectrum of $CuInS_2$ capped with crystal-bound D3MP after hydrolysis dissolved in ethanol.

APPENDIX B

ADDITIONAL COMPUTATIONAL MODELS

This Appendix includes additional computational models that supplement the models presented in Chapter 4.

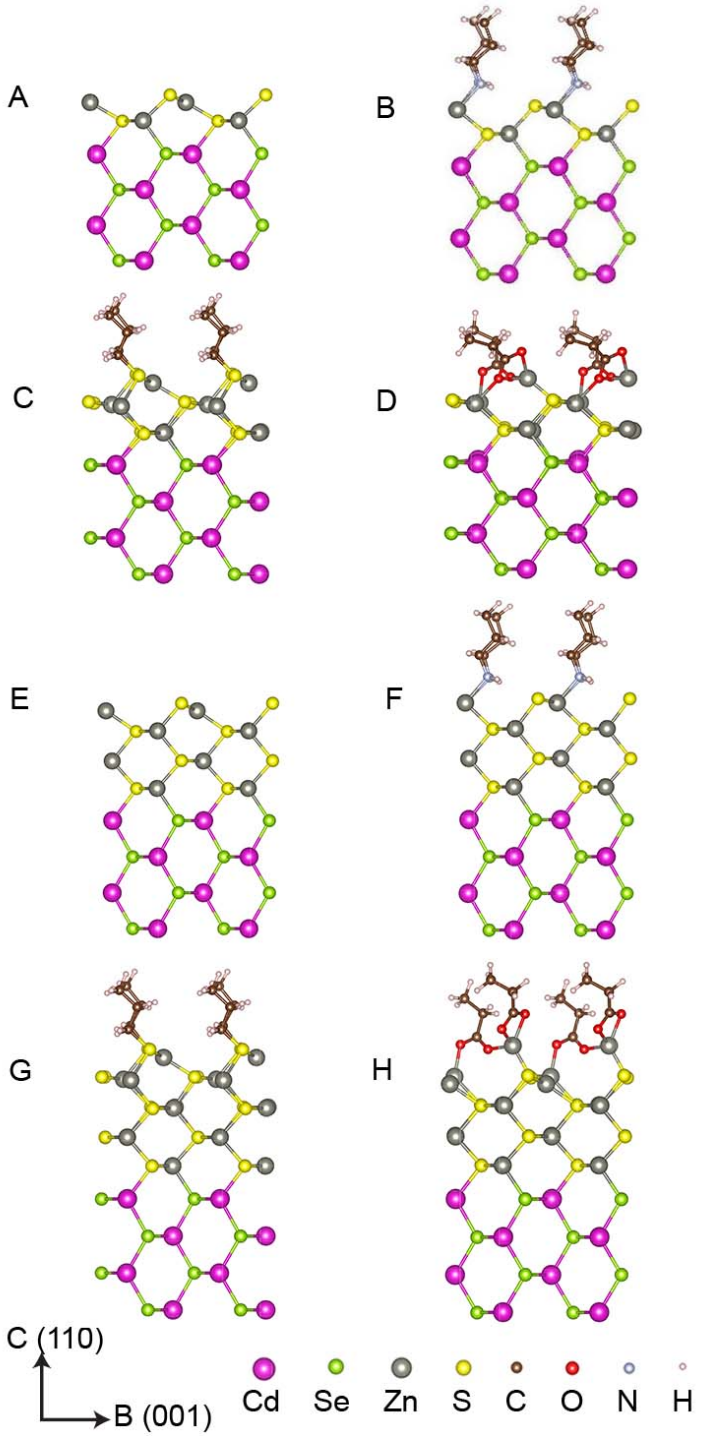

Figure B.1: Structural models of ligand coordination to the (110) surface of CdSe/ZnS slabs looking down the A-axis. (A) 1 ML of ZnS and no ligands, (B) 1 ML of ZnS and L-type propylamine, (C) 1 ML of ZnS and Z-type Zn(propanethiolate)$_2$, (D) 1 ML of ZnS and Z-type Zn(propionate)$_2$, (E) 2 ML of ZnS and no ligands, (F) 2 ML of ZnS and L-type propylamine, (G) 2 ML of ZnS and Z-type Zn(propanethiolate)$_2$, (H) 2 ML of ZnS and Z-type Zn(propionate)$_2$.

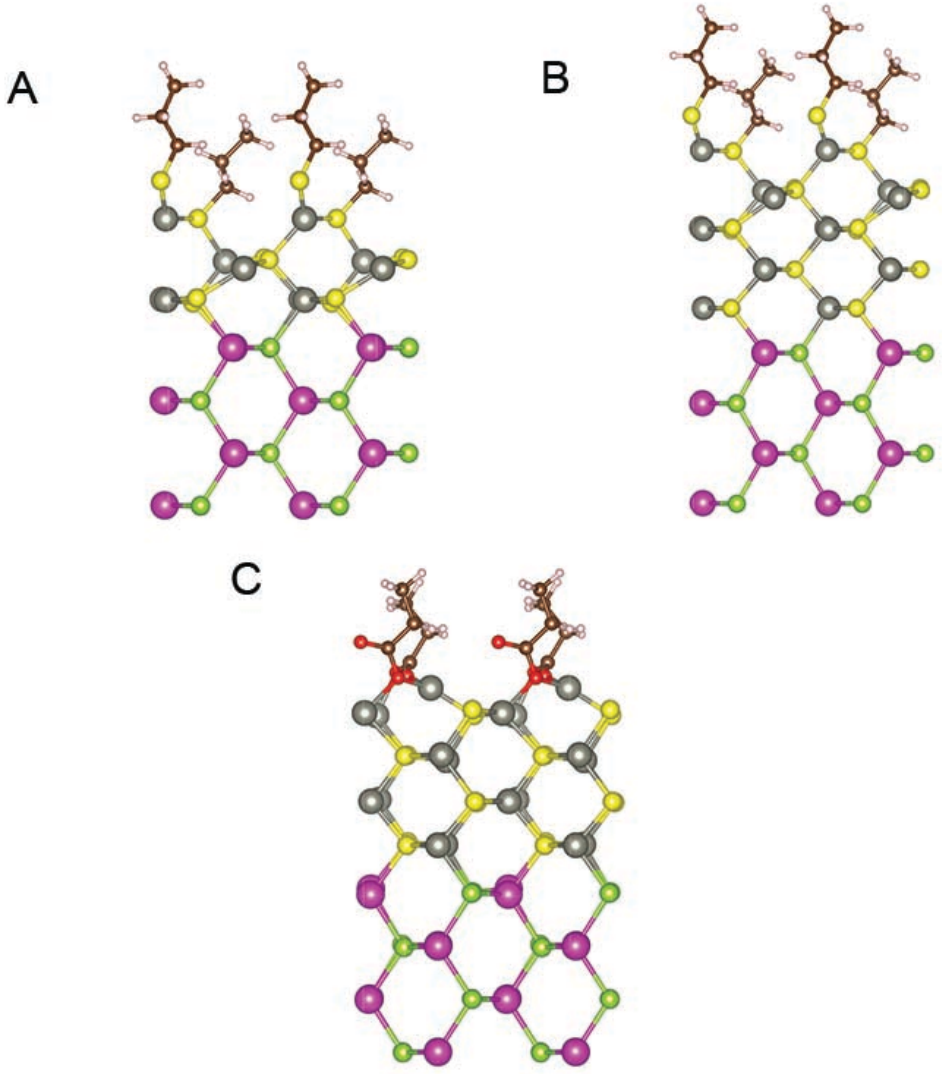

Figure B.2: Alternate bridging coordinations of Z-type ligands looking down the A-axis (A) 1 ML ZnS with a 1-bridging Z-type Zn(propanethiolate)$_2$, (B) 2ML of ZnS with a 1-bridging Z-type Zn(propanethiolate)$_2$, (C) 2 ML of ZnS with a 2-bridging Z-type Zn(propionate)$_2$.

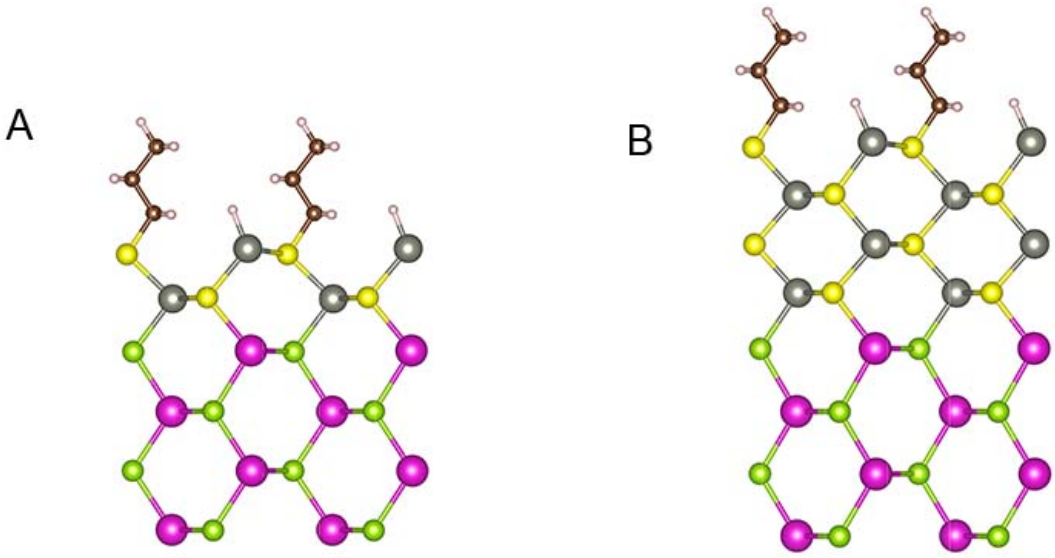

Figure B.3: Relaxed structural models for CdSe/ZnS with crystal-bound ligand passivation with 1ML (A) and 2ML (B) of ZnS looking down the A-axis. Hydride was used as the small molecule X-type ligand.

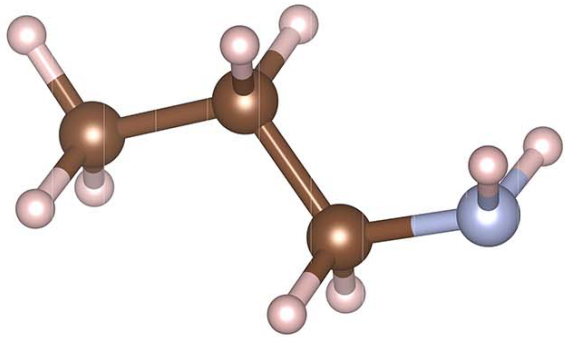

Figure B.4: Relaxed structural model of propylamine. Total calculated energy is -68.77 eV

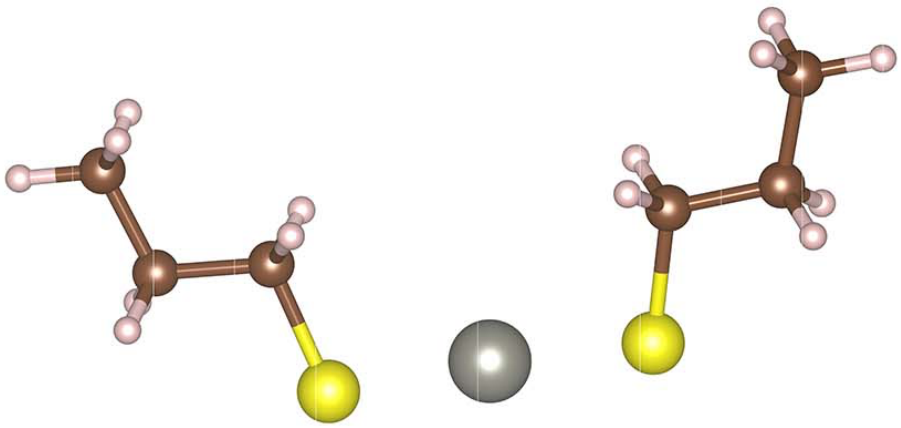

Figure B.5: Relaxed structural model of Zn(propanethiolate)$_2$. The calculated energy is -115.80 eV

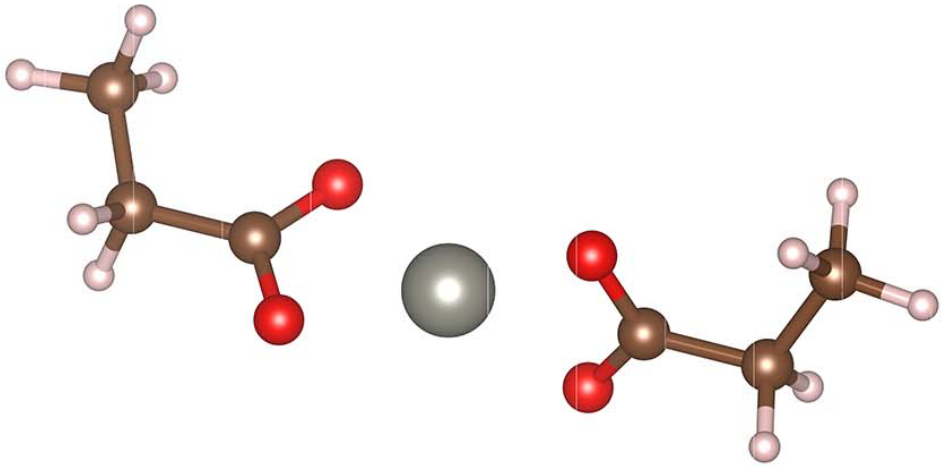

Figure B.6: Relaxed structural model of Zn(propaneionate)$_2$. The calculated energy is -120.97 eV

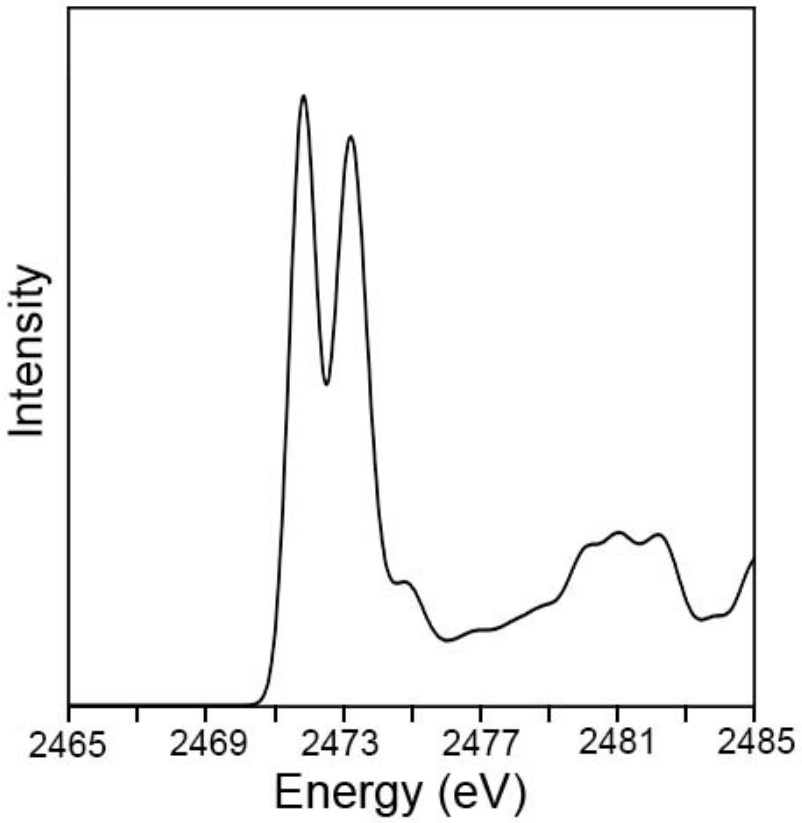

Figure B.7: Simulated S K-edge XAS for Zn(thiolate)$_2$

REFERENCES

1. Schaming, D.; Remita, H. "Nanotechnology: From the Ancient Time to Nowadays" *Found. Chem.* **2015,** 17, 187-205.

2. Colomban, P. "The Use of Metal Nanoparticles to Produce Yellow, Red and Iridescent Colour, from Bronze Age to Present Times in Lustre Pottery and Glass: Solid State Chemistry, Spectroscopy and Nanostructure" *J. Nano. Res.* **2009,** 8, 109-132.

3. Ozin, G. A.; Cademartiri, L. "Nanochemistry: What Is Next?" *Small* **2009,** 5, 1240-1244.

4. Shen, X.; Hernandez-Pagan, E. A.; Zhou, W.; Puzyrev, Y. S.; Idrobo, J. C.; Macdonald, J. E.; Pennycook, S. J.; Pantelides, S. T. "Interlaced Crystals Having a Perfect Bravais Lattice and Complex Chemical Order Revealed by Real-Space Crystallography" *Nat. Commun.* **2014,** 5.

5. Leach, A. D. P.; Shen, X.; Faust, A.; Cleveland, M. C.; La Croix, A. D.; Banin, U.; Pantelides, S. T.; Macdonald, J. E. "Defect Luminescence from Wurtzite $CuInS_2$ Nanocrystals: Combined Experimental and Theoretical Analysis" *J. Phys. Chem. C* **2016,** 120, 5207-5212.

6. Leach, A. D. P.; Mast, L. G.; Hernandez-Pagan, E. A.; Macdonald, J. E. "Phase Dependent Visible to near-Infrared Photoluminescence of $CuInS_2$ Nanocrystals" *J. Mater. Chem. C* **2015,** 3, 3258-3265.

7. Hernandez-Pagan, E. A.; Leach, A. D. P.; Rhodes, J. M.; Sarkar, S.; Macdonad, J. E. "A Synthetic Exploration of Metal Semiconductor Hybrid Particles of $CuInS_2$" *Chem. Mater.* **2015,** 27, 7969-7976.

8. Finn, S. T.; Macdonald, J. E. "Petaled Molybdenum Disulfide Surfaces: Facile Synthesis of a Superior Cathode for QDSSD" *Adv. Energy Mater.* **2014,** 4.

9. Turo, M. J.; Macdonald, J. E. "Crystal-Bound vs. Surface-Bound Thiols on Nano Crystals" *ACS Nano* **2014,** 8, 10205-10213.

10. Turo, M. J.; Shen, X.; Brandon, N. K.; Castillo, S.; Fall, A. M.; Pantelides, S. T.; Macdonald, J. E. "Dual-Mode Crystal-Bound and X-Type Passivation of Quantum Dots" *ChemComm.* **2016,** 52, 12214-12217.

11. Talapin, D. V.; Lee, J. S.; Kovalenko, M. V.; Shevchenko, E. V. "Prospects of Colloidal Nanocrystals for Electronic and Optoelectronic Applications" *Chem. Rev.* **2010,** 110, 389-458.

12. Donega, C. D. "Synthesis and Properties of Colloidal Heteronanocrystals" *Chem. Soc. Rev.* **2011,** 40, 1512-1546.

13. Scholes, G. D.; Rumbles, G. "Excitons in Nanoscale Systems" *Nat. Mater.* **2006,** 5, 683-696.

14. Brus, L. E. "Electron Electron and Electron-Hole Interactions in Small Semiconductor Crystallites - the Size Dependence of the Lowest Excited Electronic State" *J. Chem. Phys.* **1984,** 80, 4403-4409.

15. Medintz, I. L.; Uyeda, H. T.; Goldman, E. R.; Mattoussi, H. "Quantum Dot Bioconjugates for Imaging, Labelling and Sensing" *Nat Mater* **2005,** 4, 435-446.

16. van Embden, J.; Chesman, A. S. R.; Jasieniak, J. J. "The Heat-up Synthesis of Colloidal Nanocrystals" *Chem. Mater.* **2015,** 27, 2246-2285.

17. Park, J.; Joo, J.; Kwon, S. G.; Jang, Y.; Hyeon, T. "Synthesis of Monodisperse Spherical Nanocrystals" *Angew. Chem. Int. Edit.* **2007,** 46, 4630-4660.

18. Yin, Y.; Alivisatos, A. P. "Colloidal Nanocrystal Synthesis and the Organic-Inorganic Interface" *Nature* **2005,** 437, 664-670.

19. Choi, S. H.; An, K.; Kim, E. G.; Yu, J. H.; Kim, J. H.; Hyeon, T. "Simple and Generalized Synthesis of Semiconducting Metal Sulfide Nanocrystals" *Adv. Funct. Mater.* **2009,** 19, 1645-1649.

20. Sigman, M. B.; Ghezelbash, A.; Hanrath, T.; Saunders, A. E.; Lee, F.; Korgel, B. A. "Solventless Synthesis of Monodisperse Cu_2S Nanorods, Nanodisks, and Nanoplatelets" *J. Am. Chem. Soc.* **2003,** 125, 16050-16057.

21. Chen, O.; Zhao, J.; Chauhan, V. P.; Cui, J.; Wong, C.; Harris, D. K.; Wei, H.; Han, H. S.; Fukumura, D.; Jain, R. K., *et al.* "Compact High-Quality CdSe-CdS Core-Shell Nanocrystals with Narrow Emission Linewidths and Suppressed Blinking" *Nat. Mater.* **2013,** 12, 445-451.

22. Jun, S.; Jang, E. "Bright and Stable Alloy Core/Multishell Quantum Dots" *Angew. Chem. Int. Edit.* **2013,** 52, 679-682.

23. Jun, S.; Jang, E. J.; Chung, Y. S. "Alkyl Thiols as a Sulfur Precursor for the Preparation of Monodisperse Metal Sulfide Nanostructures" *Nanotechnology* **2006,** 17, 4806-4810.

24. Li, L. A.; Pandey, A.; Werder, D. J.; Khanal, B. P.; Pietryga, J. M.; Klimov, V. I. "Efficient Synthesis of Highly Luminescent Copper Indium Sulfide-Based Core/Shell Nanocrystals with Surprisingly Long-Lived Emission" *J. Am. Chem. Soc.* **2011,** 133, 1176-1179.

25. Polte, J. "Fundamental Growth Principles of Colloidal Metal Nanoparticles - a New Perspective" *CrystEngComm*. **2015,** 17, 6809-6830.

26. La Mer, V. K.; Dinegar, R. H. "Theory, Production, and Mechanism of Formation of Monodispersed Hydrosols" *J. Am. Chem. Soc*. **1950,** 72, 4847-4854.

27. Hendricks, M. P.; Campos, M. P.; Cleveland, G. T.; Jen-La Plante, I.; Owen, J. S. "A Tunable Library of Substituted Thiourea Precursors to Metal Sulfide Nanocrystals" *Science* **2015,** 348, 1226-1230.

28. Guo, Y. J.; Alvarado, S. R.; Barclay, J. D.; Vela, J. "Shape-Programmed Nanofabrication: Understanding the Reactivity of Dichalcogenide Precursors" *ACS Nano* **2013,** 7, 3616-3626.

29. Kuzuya, T.; Yamamuro, S.; Hihara, T.; Sumiyama, K. "Water-Free Solution Synthesis of Monodisperse Cu_2S Nanocrystals" *Chem. Lett*. **2004,** 33, 352-353.

30. Owen, J. "The Coordination Chemistry of Nanocrystal Surfaces" *Science* **2015,** 347, 615-616.

31. Knowles, K. E.; Frederick, M. T.; Tice, D. B.; Morris-Cohen, A. J.; Weiss, E. A. "Colloidal Quantum Dots: Think Outside the (Particle-in-a-)Box" *J. Phys. Chem. Lett*. **2012,** 3, 18-26.

32. Anderson, N. C. H., M. P.; Choi, J.J.; Owen, J.S. "Ligand Exchange and the Stoichiometry of Metal Chalcogenide Nanocrystals: Spectroscopic Observation of Facile Metal-Carboxylate Displacement and Binding" *J. Am. Chem. Soc*. **2013,** 135, 18536-18548.

33. Owen, J. S.; Park, J.; Trudeau, P. E.; Alivisatos, A. P. "Reaction Chemistry and Ligand Exchange at Cadmium-Selenide Nanocrystal Surfaces" *J. Am. Chem. Soc*. **2008,** 130, 12279-12281.

34. Green, M. L. H. "A New Approach to the Formal Classification of Covalent Compounds of the Elements" *J. Organomet. Chem*. **1995,** 500, 127-148.

35. De Roo, J.; Justo, Y.; De Keukeleere, K.; Van den Broeck, F.; Martins, J. C.; Van Driessche, I.; Hens, Z. "Carboxylic-Acid-Passivated Metal Oxide Nanocrystals: Ligand Exchange Characteristics of a New Binding Motif" *Angew. Chem. Int. Edit*. **2015,** 54, 6488-6491.

36. Hens, Z.; Martins, J. C. "A Solution Nmr Toolbox for Characterizing the Surface Chemistry of Colloidal Nanocrystals" *Chem. Mater*. **2013,** 25, 1211-1221.

37. Morris-Cohen, A. J.; Malicki, M.; Peterson, M. D.; Slavin, J. W. J.; Weiss, E. A. "Chemical, Structural, and Quantitative Analysis of the Ligand Shells of Colloidal Quantum Dots" *Chem. Mater.* **2013,** 25, 1155-1165.

38. *Encyclopedia of Materials Charaterization: Surface, Interfaces, Thin Films*. 1992.

39. Chen, X. B.; Li, C.; Gratzel, M.; Kostecki, R.; Mao, S. S. "Nanomaterials for Renewable Energy Production and Storage" *Chem. Soc. Rev.* **2012,** 41, 7909-7937.

40. Green, M. "The Nature of Quantum Dot Capping Ligands" *J. Mater. Chem.* **2010,** 20, 5797-5809.

41. Zhuang, Z. B.; Peng, Q.; Zhang, B.; Li, Y. D. "Controllable Synthesis of Cu_2S Nanocrystals and Their Assembly into a Superlattice" *J. Am. Chem. Soc.* **2008,** 130, 10482-10483.

42. Kruszynska, M.; Borchert, H.; Bachmatiuk, A.; Rummeli, M. H.; Buchner, B.; Parisi, J.; Kolny-Olesiak, J. "Size and Shape Control of Colloidal Copper(I) Sulfide Nanorods" *ACS Nano* **2012,** 6, 5889-5896.

43. Kruszynska, M.; Borchert, H.; Parisi, J.; Kolny-Olesiak, J. "Synthesis and Shape Control of $CuInS_2$ Nanoparticles" *J. Am. Chem. Soc.* **2010,** 132, 15976-15986.

44. Xie, R. G.; Rutherford, M.; Peng, X. G. "Formation of High-Quality I-III-VI Semiconductor Nanocrystals by Tuning Relative Reactivity of Cationic Precursors" *J. Am. Chem. Soc.* **2009,** 131, 5691-5697.

45. Wang, Y. H. A.; Zhang, X. Y.; Bao, N. Z.; Lin, B. P.; Gupta, A. "Synthesis of Shape-Controlled Monodisperse Wurtzite $CuIn_XGa_{1-X}S_2$ Semiconductor Nanocrystals with Tunable Band Gap" *J. Am. Chem. Soc.* **2011,** 133, 11072-11075.

46. Singh, A.; Geaney, H.; Laffir, F.; Ryan, K. M. "Colloidal Synthesis of Wurtzite Cu_2ZnSnS_4 Nanorods and Their Perpendicular Assembly" *J. Am. Chem. Soc.* **2012,** 134, 2910-2913.

47. Han, W.; Yi, L. X.; Zhao, N.; Tang, A. W.; Gao, M. Y.; Tang, Z. Y. "Synthesis and Shape-Tailoring of Copper Sulfide/Indium Sulfide-Based Nanocrystals" *J. Am. Chem. Soc.* **2008,** 130, 13152-13161.

48. Bae, W. K.; Padilha, L. A.; Park, Y. S.; McDaniel, H.; Robel, I.; Pietryga, J. M.; Klimov, V. I. "Controlled Alloying of the Core-Shell Interface in CdSe/CdS Quantum Dots for Suppression of Auger Recombination" *ACS Nano* **2013,** 7, 3411-3419.

49. Bryks, W.; Wette, M.; Velez, N.; Hsu, S.-W.; Tao, A. R. "Supramolecular Precursors for the Synthesis of Anisotropic Cu_2S Nanocrystals" *J. Am. Chem. Soc.* **2014,** 136, 6175-6178.

50. Vinokurov, K.; Macdonald, J. E.; Banin, U. "Structures and Mechanisms in the Growth of Hybrid Ru-Cu_2S Nanoparticles: From Cages to Nanonets" *Chem. Mater.* **2012,** 24, 1822-1827.

51. Luther, J. M.; Law, M.; Song, Q.; Perkins, C. L.; Beard, M. C.; Nozik, A. J. "Structural, Optical and Electrical Properties of Self-Assembled Films of PbSe Nanocrystals Treated with 1,2-Ethanedithiol" *ACS Nano* **2008,** 2, 271-280.

52. Kim, Y.; Park, K. Y.; Jang, D. M.; Song, Y. M.; Kim, H. S.; Cho, Y. J.; Myung, Y.; Park, J. "Synthesis of Au-Cu_2S Core-Shell Nanocrystals and Their Photocatalytic and Electrocatalytic Activity" *J. Phys. Chem. C* **2010,** 114, 22141-22146.

53. Fritzinger, B.; Capek, R. K.; Lambert, K.; Martins, J. C.; Hens, Z. "Utilizing Self-Exchange to Address the Binding of Carboxylic Acid Ligands to Cdse Quantum Dots" *J. Am. Chem. Soc.* **2010,** 132, 10195-10201.

54. Moreels, I.; Martins, J. C.; Hens, Z. "Ligand Adsorption/Desorption on Sterically Stabilized Inp Colloidal Nanocrystals: Observation and Thermodynamic Analysis" *ChemPhysChem.* **2006,** 7, 1028-1031.

55. Gomes, R.; Hassinen, A.; Szczygiel, A.; Zhao, Q. A.; Vantomme, A.; Martins, J. C.; Hens, Z. "Binding of Phosphonic Acids to CdSe Quantum Dots: A Solution Nmr Study" *J. Phys. Chem. Lett.* **2011,** 2, 145-152

.

56. Nørby, P.; Johnsen, S.; Iversen, B. B. "In Situ X-Ray Diffraction Study of the Formation, Growth, and Phase Transition of Colloidal $Cu_{2-X}S$ Nanocrystals" *ACA Nano* **2014,** 8, 4295-4303.

57. Aldana, J.; Wang, Y. A.; Peng, X. G. "Photochemical Instability of Cdse Nanocrystals Coated by Hydrophilic Thiols" *J. Am. Chem. Soc.* **2001,** 123, 8844-8850.

58. Li, X.-B. L., Zhi-Jun; Gao, Yu-Ji, Meng, Qing-Yuan; Yu, Shan; Weiss, Richard G.; Tung, Chen-Ho; Wu, Li-Zhu. "Mechanistic Insights into the Interface-Directed Transformation of Thiols into Disulfides and Molecular Hydrogen by Visible-Light Irradiation of Quantum Dots" *Angew. Chem. Int. Edit.* **2014,** 53, 2085-2089.

59. Xie, Y.; Riedinger, A.; Prato, M.; Casu, A.; Genovese, A.; Guardia, P.; Sottini, S.; Sangregorio, C.; Miszta, K.; Ghosh, S., *et al.* "Copper Sulfide Nanocrystals with Tunable Composition by Reduction of Covellite Nanocrystals with Cu+ Ions" *J. Am. Chem. Soc.* **2013,** 135, 17630-17637.

60. Li, H. B.; Brescia, R.; Povia, M.; Prato, M.; Bertoni, G.; Manna, L.; Moreels, I. "Synthesis of Uniform Disk-Shaped Copper Telluride Nanocrystals and Cation Exchange to Cadmium Telluride Quantum Disks with Stable Red Emission" *J. Am. Chem. Soc.* **2013,** 135, 12270-12278.

61. Lai, Y. H.; Yeh, C. T.; Cheng, S. H.; Liao, P.; Hung, W. H. "Adsorption and Thermal Decomposition of Alkanethiols on Cu(110)" *J. Phys. Chem. B* **2002,** 106, 5438-5446.

62. Berkowitz, J. M. J. R. "Equilibrium Composition of Sulfur Vapor" *J. Chem. Phys.* **1963,** 39, 275-283.

63. de Petris, G.; Cartoni, A.; Rosi, M.; Troiani, A. "The HSSS Radical and the $HSSS^-$ Anion" *J. Phys. Chem. A* **2008,** 112, 8471-8477.

64. Bryks, W.; Lupi, E.; Ngo, C.; Tao, A. R. "Digenite Nanosheets Synthesized by Thermolysis of Layered Copper-Alkanethiolate Frameworks" *J. Am. Chem. Soc.* **2016,** 138, 13717-13725.

65. Byrne, C.; Sallas, F.; Rai, D. K.; Ogier, J.; Darcy, R. "Poly-6-Cationic Amphiphilic Cyclodextrins Designed for Gene Delivery" *Org. Biomol. Chem.* **2009,** 7, 3763-3771.

66. Zhao, Y. X.; Pan, H. C.; Lou, Y. B.; Qiu, X. F.; Zhu, J. J.; Burda, C. "Plasmonic $Cu_{2-X}S$ Nanocrystals: Optical and Structural Properties of Copper-Deficient Copper(I) Sulfides" *J. Am. Chem. Soc.* **2009,** 131, 4253-4261.

67. Luther, J. M.; Jain, P. K.; Ewers, T.; Alivisatos, A. P. "Localized Surface Plasmon Resonances Arising from Free Carriers in Doped Quantum Dots" *Nat. Mater.* **2011,** 10, 361-366.

68. Macdonald, J. E.; Bar Sadan, M.; Houben, L.; Popov, I.; Banin, U. "Hybrid Nanoscale Inorganic Cages" *Nat. Mater.* **2010,** 9, 810-815.

69. Wen, X. G.; Zhang, W. X.; Yang, S. H. "Solution Phase Synthesis of Cu(Oh)(2) Nanoribbons by Coordination Self-Assembly Using Cu_2S Nanowires as Precursors" *Nano Lett* **2002,** 2, 1397-1401.

70. Wang, W. Z.; Zhou, Q.; Fei, X. M.; He, Y. B.; Zhang, P. C.; Zhang, G. L.; Peng, L.; Xie, W. J. "Synthesis of CuO Nano- and Micro-Structures and Their Raman Spectroscopic Studies" *CrystEngComm* **2010,** 12, 2232-2237.

71. Zhao, Y. X.; Burda, C. "Development of Plasmonic Semiconductor Nanomaterials with Copper Chalcogenides for a Future with Sustainable Energy Materials" *Energ. Environ. Sci.* **2012,** 5, 5564-5576.

72. Niezgoda, J. S.; Harrison, M. A.; McBride, J. R.; Rosenthal, S. J. "Novel Synthesis of Chalcopyrite $Cu_xIn_yS_2$ Quantum Dots with Tunable Localized Surface Plasmon Resonances" *Chem. Mater.* **2012,** 24, 3294-3297.

73. Bai, B.; Kou, D. X.; Zhou, W. H.; Zhou, Z. J.; Wu, S. X. "Application of Quaternary Cu2znsns4 Quantum Dot-Sensitized Solar Cells Based on the Hydrolysis Approach" *Green Chem*. **2015,** 17, 4377-4382.

74. Tang, A. W.; Qu, S. C.; Li, K.; Hou, Y. B.; Teng, F.; Cao, J.; Wang, Y. S.; Wang, Z. G. "One-Pot Synthesis and Self-Assembly of Colloidal Copper(I) Sulfide Nanocrystals" *Nanotechnology* **2010,** 21.

75. Jun, S. A.; Jang, E. J.; Seong, J. C. Method for Manufacturing Metal Sulfiide Nanocrystals Using Thiol Compound as Sulfur Precursor. 2008.

76. Jadzinsky, P. D.; Calero, G.; Ackerson, C. J.; Bushnell, D. A.; Kornberg, R. D. "Structure of a Thiol Monolayer-Protected Gold Nanoparticle at 1.1 Angstrom Resolution" *Science* **2007,** 318, 430-433.

77. Mott, D.; Yin, J.; Engelhard, M.; Loukrakpam, R.; Chang, P.; Miller, G.; Bae, I. T.; Das, N. C.; Wang, C. M.; Luo, J., *et al*. "From Ultrafine Thiolate-Capped Copper Nanoclusters toward Copper Sulfide Nanodiscs: A Thermally Activated Evolution Route" *Chem. Mater*. **2010,** 22, 261-271.

78. Corthey, G.; Rubert, A. A.; Picone, A. L.; Casillas, G.; Giovanetti, L. J.; Ramallo-Lopez, J. M.; Zelaya, E.; Benitez, G. A.; Requejo, F. G.; Jose-Yacaman, M., *et al*. "New Insights into the Chemistry of Thiolate-Protected Palladium Nanoparticles" *J. Phys. Chem. C* **2012,** 116, 9830-9837.

79. Calderon, M. F.; Zelaya, E.; Benitez, G. A.; Schilardi, P. L.; Creus, A. H.; Orive, A. G.; Salvarezza, R. C.; Ibanez, F. J. "New Findings for the Composition and Structure of Ni Nanoparticles Protected with Organomercaptan Molecules" *Langmuir* **2013,** 29, 4670-4678.

80. Sperling, R. A.; Parak, W. J. "Surface Modification, Functionalization and Bioconjugation of Colloidal Inorganic Nanoparticles" *Philos. Trans. Roy. Soc. A* **2010,** 368, 1333-1383.

81. Scher, E. C.; Manna, L.; Alivisatos, A. P. "Shape Control and Applications of Nanocrystals" *Philos. Trans. Roy Soc A* **2003,** 361, 241-255.

82. Anderson, N. C.; Owen, J. S. "Soluble, Chloride-Terminated Cdse Nanocrystals: Ligand Exchange Monitored by H-1 and P-31 NMR Spectroscopy" *Chem. Mater*. **2013,** 25, 69-76.

83. Ip, A. H.; Thon, S. M.; Hoogland, S.; Voznyy, O.; Zhitomirsky, D.; Debnath, R.; Levina, L.; Rollny, L. R.; Carey, G. H.; Fischer, A., *et al*. "Hybrid Passivated Colloidal Quantum Dot Solids" *Nat. Nanotechnol*. **2012,** 7, 577-582.

84. Zherebetskyy, D.; Scheele, M.; Zhang, Y. J.; Bronstein, N.; Thompson, C.; Britt, D.; Salmeron, M.; Alivisatos, P.; Wang, L. W. "Hydroxylation of the Surface of Pbs Nanocrystals Passivated with Oleic Acid" *Science* **2014,** 344, 1380-1384.

85. Herron, N.; Calabrese, J. C.; Farneth, W. E.; Wang, Y. "Crystal-Structure and Optical-Properties of $Cd_{32}S_{14}(SC_6H_5)_{36}.DMF_4$, a Cluster with a 15-Angstrom CdS Core" *Science* **1993,** 259, 1426-1428.

86. Chen, O.; Chen, X.; Yang, Y. A.; Lynch, J.; Wu, H. M.; Zhuang, J. Q.; Cao, Y. C. "Synthesis of Metal-Selenide Nanocrystals Using Selenium Dioxide as the Selenium Precursor" *Angew. Chem. Int. Edit.* **2008,** 47, 8638-8641

.

87. Dethlefsen, J. R.; Dossing, A. "Preparation of a ZnS Shell on CdSe Quantum Dots Using a Single-Molecular ZnS Precursor" *Nano Lett.* **2011,** 11, 1964-1969.

88. Dhas, N. A.; Zaban, A.; Gedanken, A. "Surface Synthesis of Zinc Sulfide Nanoparticles on Silica Microspheres: Sonochemical Preparation, Characterization, and Optical Properties" *Chem. Mater.* **1999,** 11, 806-813.

89. Nag, A.; Kovalenko, M. V.; Lee, J. S.; Liu, W. Y.; Spokoyny, B.; Talapin, D. V. "Metal-Free Inorganic Ligands for Colloidal Nanocrystals: S^{2-}, HS^-, Se^{2-}, HSe^-, Te^{2-}, HTe^-, TeS_3^{2-}, OH^-, and NH_2^- as Surface Ligands" *J. Am. Chem. Soc.* **2011,** 133, 10612-10620.

90. Alivisatos, A. P. "Semiconductor Clusters, Nanocrystals, and Quantum Dots" *Science* **1996,** 271, 933-937.

91. Frederick, M. T.; Weiss, E. A. "Relaxation of Exciton Confinement in Cdse Quantum Dots by Modification with a Conjugated Dithiocarbamate Ligand" *ACS Nano* **2010,** 4, 3195-3200.

92. Hamad, S.; Cristol, S.; Callow, C. R. A. "Surface Structures and Crystal Morphology of ZnS: Computational Study" *J. Phys. Chem. B* **2002,** 106, 11002-11008.

93. Reiss, P.; Protiere, M.; Li, L. "Core/Shell Semiconductor Nanocrystals" *Small* **2009,** 5, 154-168.

94. Wei, S. H.; Zunger, A. "Calculated Natural Band Offsets of All II-Vi and III-V Semiconductors: Chemical Trends and the Role of Cation D Orbitals" *Appl. Phys. Lett.* **1998,** 72, 2011-2013.

95. Han, Z. J.; Qiu, F.; Eisenberg, R.; Holland, P. L.; Krauss, T. D. "Robust Photogeneration of H-2 in Water Using Semiconductor Nanocrystals and a Nickel Catalyst" *Science* **2012,** 338, 1321-1324.

96. Costi, R.; Saunders, A. E.; Elmalem, E.; Salant, A.; Banin, U. "Visible Light-Induced Charge Retention and Photocatalysis with Hybrid CdSe-Au Nanodumbbells" *Nano Lett*. **2008,** 8, 637-641.

97. Yu, W. W.; Qu, L. H.; Guo, W. Z.; Peng, X. G. "Experimental Determination of the Extinction Coefficient of CdTe, CdSe, and CdS Nanocrystals" *Chem. Mater*. **2003,** 15, 2854-2860.

98. Chen, D. A.; Zhao, F.; Qi, H.; Rutherford, M.; Peng, X. G. "Bright and Stable Purple/Blue Emitting CdS/ZnS Core/Shell Nanocrystals Grown by Thermal Cycling Using a Single-Source Precursor" *Chem. Mater*. **2010,** 22, 1437-1444.

99. Brouwer, A. M. "Standards for Photoluminescence Quantum Yield Measurements in Solution (IUPAC Technical Report)" *Pure Appl. Chem*. **2011,** 83, 2213-2228.

100. Perdew, J. P.; Burke, K.; Ernzerhof, M. "Generalized Gradient Approximation Made Simple" *Phys. Rev. Lett*. **1996,** 77, 3865-3868.

101. Kresse, G.; Joubert, D. "From Ultrasoft Pseudopotentials to the Projector Augmented-Wave Method" *Phys. Rev. B* **1999,** 59, 1758-1775.

102. Kresse, G.; Furthmuller, J. "Efficient Iterative Schemes for *Ab Initio* Total-Energy Calculations Using a Plane-Wave Basis Set" *Phys. Rev. B* **1996,** 54, 11169-11186.

103. Tan, R.; Shen, Y.; Roberts, S. K.; Gee, M. Y.; Blom, D. A.; Greytak, A. B. "Reducing Competition by Coordinating Solvent Promotes Morphological Control in Alternating Layer Growth of CdSe/CdS Core/Shell Quantum Dots" *Chem Mater* **2015,** 27, 7468-7480.

104. Yan, B.; Jeong, Y.; Mercante, L. A.; Tonga, G. Y.; Kim, C.; Zhu, Z. J.; Vachet, R. W.; Rotello, V. M. "Characterization of Surface Ligands on Functionalized Magnetic Nanoparticles Using Laser Desorption/Ionization Mass Spectrometry (LDI-MS)" *Nanoscale* **2013,** 5, 5063-5066.

105. Zhou, H. Y.; Li, X.; Lemoff, A.; Zhang, B.; Yan, B. "Structural Confirmation and Quantification of Individual Ligands from the Surface of Multi-Functionalized Gold Nanoparticles" *Analyst* **2010,** 135, 1210-1213.

106. Katari, J. E. B.; Colvin, V. L.; Alivisatos, A. P. "X-Ray Photoelectron-Spectroscopy of CdSe Nanocrystals with Applications to Studies of the Nanocrystal Surface" *J. Phys. Chem*. **1994,** 98, 4109-4117.

107. Piyeteau, L.; Ong, T. C.; Rossini, A. J.; Emsley, L.; Coperet, C.; Kovalenko, M. V. "Structure of Colloidal Quantum Dots from Dynamic Nuclear Polarization Surface Enhanced NMR Spectroscopy" *J. Am. Chem. Soc*. **2015,** 137, 13964-13971.

108. Protesescu, L.; Nachtegaal, M.; Voznyy, O.; Borovinskaya, O.; Rossini, A. J.; Emsley, L.; Coperet, C.; Gunther, D.; Sargent, E. H.; Kovalenko, M. V. "Atomistic Description of Thiostannate-Capped Cdse Nanocrystals: Retention of Four-Coordinate SnS_4 Motif and Preservation of Cd-Rich Stoichiometry" *J. Am. Chem. Soc.* **2015,** 137, 1862-1874.

109. Gary, D. C.; Flowers, S. E.; Kaminsky, W.; Petrone, A.; Li, X. S.; Cossairt, B. M. "Single-Crystal and Electronic Structure of a 1.3 nm Indium Phosphide Nanocluster" *J. Am. Chem. Soc.* **2016,** 138, 1510-1513.

110. Aruguete, D. M.; Marcus, M. A.; Li, L. S.; Williamson, A.; Fakra, S.; Gygi, F.; Galli, G. A.; Alivisatos, A. P. "Surface Structure of CdSe Nanorods Revealed by Combined X-Ray Absorption Fine Structure Measurements and Ab Initio Calculations" *J. Phys. Chem. C* **2007,** 111, 75-79.

111. Lee, J. R. I.; Whitley, H. D.; Meulenberg, R. W.; Wolcott, A.; Zhang, J. Z.; Prendergast, D.; Lovingood, D. D.; Strouse, G. F.; Ogitsu, T.; Schwegler, E., *et al.* "Ligand-Mediated Modification of the Electronic Structure of CdSe Quantum Dots" *Nano Lett.* **2012,** 12, 2763-2767.

112. Newton, M. A.; Dent, A. J.; Evans, J. "Bringing Time Resolution to Exafs: Recent Developments and Application to Chemical Systems" *Chem. Soc. Rev.* **2002,** 31, 83-95.

113. Knauf, R. R.; Lennox, J. C.; Dempsey, J. L. "Quantifying Ligand Exchange Reactions at CdSe Nanocrystal Surfaces" *Chem. Mater.* **2016,** 28, 4762-4770.

114. Srivastava, G. P. "Theory of Semiconductor Surface Reconstruction" *Rep. Prog. Phys.* **1997,** 60, 561-613.

115. Voznyy, O. "Mobile Surface Traps in CdSe Nanocrystals with Carboxylic Acid Ligands" *J. Phys. Chem. C* **2011,** 115, 15927-15932.

116. Zhou, Y.; Wang, F. D.; Buhro, W. E. "Large Exciton Energy Shifts by Reversible Surface Exchange in 2D II-VI Nanocrystals" *J. Am. Chem. Soc.* **2015,** 137, 15198-15208.

117. Shen, Y.; Tan, R.; Gee, M. Y.; Greytak, A. B. "Quantum Yield Regeneration: Influence of Neutral Ligand Binding on Photophysical Properties in Colloidal Core/Shell Quantum Dots" *ACS Nano* **2015,** 9, 3345-3359.

118. Gong, K.; Kelley, D. F. "Lattice Strain Limit for Uniform Shell Deposition in Zincblende Cdse/Cds Quantum Dots" *J. Phys. Chem. Lett.* **2015,** 6, 1559-1562.

119. Mangel, S.; Houben, L.; Bar Sadan, M. "The Effect of Atomic Disorder at the Core-Shell Interface on Stacking Fault Formation in Hybrid Nanoparticles" *Nanoscale* **2016,** 8, 17568-17572.

120. Orfield, N. J.; McBride, J. R.; Keene, J. D.; Davis, L. M.; Rosenthal, S. J. "Correlation of Atomic Structure an Photoluminescence of the Same Quantum Dot: Pinpointing Surface and Internal Defects That Inhibit Photoluminescence" *ACS Nano* **2015,** 9, 831-839.

121. Giannozzi, P.; Baroni, S.; Bonini, N.; Calandra, M.; Car, R.; Cavazzoni, C.; Ceresoli, D.; Chiarotti, G. L.; Cococcioni, M.; Dabo, I., *et al*. "Quantum Espresso: A Modular and Open-Source Software Project for Quantum Simulations of Materials" *J. Phys.-Condens. Mat.* **2009,** 21.

122. Prendergast, D.; Galli, G. "X-Ray Absorption Spectra of Water from First Principles Calculations" *Phys. Rev. Lett.* **2006,** 96.

123. von Oertzen, G. U.; Jones, R. T.; Gerson, A. R. "Electronic and Optical Properties of Fe, Zn and Pb Sulfides" *Phys. Chem. Miner.* **2005,** 32, 255-268.

124. Gabrelian, B. V.; Lavrentyev, A. A.; Nikiforov, I. Y. "XANES and Unoccupied Dos of Sulfides and Selenides of Zn and Cd" *Phys. Status Solidi. B* **1999,** 215, 1041-1047.

125. Buck, M. R.; Bondi, J. F.; Schaak, R. E. "A Total-Synthesis Framework for the Construction of High-Order Colloidal Hybrid Nanoparticles" *Nat. Chem.* **2012,** 4, 37-44.

126. Cho, K. S.; Talapin, D. V.; Gaschler, W.; Murray, C. B. "Designing PbSe Nanowires and Nanorings through Oriented Attachment of Nanoparticles" *J. Am. Chem. Soc.* **2005,** 127, 7140-7147.

127. Costi, R.; Saunders, A. E.; Banin, U. "Colloidal Hybrid Nanostructures: A New Type of Functional Materials" *Angew. Chem. Int. Edit.* **2010,** 49, 4878-4897.

128. Amirav, L.; Alivisatos, A. P. "Photocatalytic Hydrogen Production with Tunable Nanorod Heterostructures" *J. Phys. Chem. Lett.* **2010,** 1, 1051-1054.

129. Liu, G. M.; Schulmeyer, T.; Brotz, J.; Klein, A.; Jaegermann, W. "Interface Properties and Band Alignment of Cu_2S/CdS Thin Film Solar Cells" *Thin Solid Films* **2003,** 431, 477-482.

130. Yamada, Y.; Miyahigashi, T.; Kotani, H.; Ohkubo, K.; Fukuzumi, S. "Photocatalytic Hydrogen Evolution under Highly Basic Conditions by Using Ru Nanoparticles and 2-Phenyl-4-(1-Naphthyl)Quinolinium Ion" *J. Am. Chem. Soc.* **2011,** 133, 16136-16145.

131. Penn, R. L.; Banfield, J. F. "Imperfect Oriented Attachment: Dislocation Generation in Defect-Free Nanocrystals" *Science* **1998,** 281, 969-971.

132. Cozzoli, P. D.; Pellegrino, T.; Manna, L. "Synthesis, Properties and Perspectives of Hybrid Nanocrystal Structures" *Chem. Soc. Rev.* **2006,** 35, 1195-1208.

133. O'Sullivan, C.; Gunning, R. D.; Sanyal, A.; Barrett, C. A.; Geaney, H.; Laffir, F. R.; Ahmed, S.; Ryan, K. M. "Spontaneous Room Temperature Elongation of CdS and Ag_2S Nanorods Via Oriented Attachment" *J. Am. Chem. Soc.* **2009,** 131, 12250-12257.

134. Evans, D. A.; Carter, P. H.; Dinsmore, C. J.; Barrow, J. C.; Katz, J. L.; Kung, D. W. "Mild Nitrosation and Hydrolysis of Polyfunctional Amides" *Tetrahedron Lett.* **1997,** 38, 4535-4538.

135. De Trizio, L.; Manna, L. "Forging Colloidal Nanostructures Via Cation Exchange Reactions" *Chem. Rev.* **2016,** 116, 10852-10887.

136. Luther, J. M.; Zheng, H. M.; Sadtler, B.; Alivisatos, A. P. "Synthesis of PbS Nanorods and Other Ionic Nanocrystals of Complex Morphology by Sequential Cation Exchange Reactions" *J. Am. Chem. Soc.* **2009,** 131, 16851-16857.

137. Willis, A. L.; Turro, N. J.; O'Brien, S. "Spectroscopic Characterization of the Surface of Iron Oxide Nanocrystals" *Chem Mater* **2005,** 17, 5970-5975.

138. Ornelas, C.; Mery, D.; Cloutet, E.; Aranzaes, J. R.; Astruc, D. "Cross Olefin Metathesis for the Selective Functionalization, Ferrocenylation, and Solubilization in Water of Olefin-Terminated Dendrimers, Polymers, and Gold Nanoparticles and for a Divergent Dendrimer Construction" *J. Am. Chem. Soc.* **2008,** 130, 1495-1506

.

139. Tavasoli, E.; Guo, Y. J.; Kunal, P.; Grajeda, J.; Gerber, A.; Vela, J. "Surface Doping Quantum Dots with Chemically Active Native Ligands: Controlling Valence without Ligand Exchange" *Chem. Mater.* **2012,** 24, 4231-4241.

140. De Roo, J.; De Keukeleere, K.; Hens, Z.; Van Driessche, I. "From Ligands to Binding Motifs and Beyond; the Enhanced Versatility of Nanocrystal Surfaces" *Dalton Trans.* **2016,** 45, 13277-13283.

141. Liu, L. P.; Zhuang, Z. B.; Xie, T.; Wang, Y. G.; Li, J.; Peng, Q.; Li, Y. D. "Shape Control of CdSe Nanocrystals with Zinc Blende Structure" *J Am Chem Soc* **2009,** 131, 16423-16429.

142. Carey, G. H.; Abdelhady, A. L.; Ning, Z. J.; Thon, S. M.; Bakr, O. M.; Sargent, E. H. "Colloidal Quantum Dot Solar Cells" *Chem. Rev.* **2015,** 115, 12732-12763.

143. Meinardi, F.; McDaniel, H.; Carulli, F.; Colombo, A.; Velizhanin, K. A.; Makarov, N. S.; Simonutti, R.; Klimov, V. I.; Brovelli, S. "Highly Efficient Large-Area Colourless Luminescent Solar Concentrators Using Heavy-Metal-Free Colloidal Quantum Dots" *Nat. Nanotechnol.* **2015,** 10, 878-885.

144. Evans, H. T. "Crystal Structure of Low Chalcocite" *Nature-Phys. Sci.* **1971,** 232, 69.

Michael Turo

michael.turo@vanderbilt.edu

7330 Stevenson Center
Nashville, TN 37235

Education:

Graduate School: Vanderbilt University-PhD Chemistry, expected graduation Fall 2016
Undergraduate: Villanova University- B.S. Chemistry 2011

Awards/Certificates:

Certificate for Technology Entrepreneurship and Commercialization, Vanderbilt University 2016
2014 Department of Energy Office of Science Graduate Student Research (SCGSR) Award
Mitchum E. Warren Fellowship, Vanderbilt Department of Chemistry Spring 2013
2011 Delap-Holcomb Scholarship, Gamma Sigma Epsilon Chemistry Honors Society
2010 Undergraduate Award for Inorganic Chemistry, American Chemical Society Division of Inorganic Chemistry

Research Experience:

Lawrence Berkeley National Lab, the Molecular Foundry, Graduate Student Affiliate-February 2015 to December 2015, Collaborator: Dr. David Prendergast, Area of research: computational chemistry, surface chemistry
Vanderbilt University, Graduate Research Assistant- January 2012- present Advisor: Dr. Janet Macdonald, Area of research: nanochemistry, inorganic chemistry, materials chemistry, surface chemistry
SI Group, Research Intern- June 2010 to August 2010, Advisor: Dr. John Lorenc, Areas of research: synthetic organic chemistry, polymer chemistry
Villanova University, Undergraduate Research Assistant- June 2008 to May 2011 Advisor: Dr. Joseph Bausch, Areas of research: physical organic chemistry, synthetic organic chemistry, computational chemistry.
Additional Research Rotations at Vanderbilt, Dr. Michael Stone and Dr. Charles Lukehart.

Publications:

Robinson, Evan H, *Turo, Michael J.;* Macdonald, Janet E. "Controlled Surface Chemistry for the Directed Attachment of Copper(I) Sulfide Nanocrystals." *In prep*.
Turo, Michael J.; Shen, Xiao; Brandon, Nazharie K.; Castillo, Stephanie; Fall, Amadou M.; Pantelides, Sokrates T.; Macdonald, Janet E. "Dual Mode Crystal-Bound and X-type Passivation of Quantum Dots." **ChemComm**, 2016. 54, 12214-12217.
Turo, Michael J.; Macdonald, Janet E. "Crystal-Bound vs. Surface-Bound Thiols on Nanoparticles" **ACS Nano**, 2014, 8, 10, 10205-10213
Kowal, Ewa; Wickramaratne, Susith; Kotapati, Srikanth; *Turo, Michael*; Tretyakova, Natalia; Stone, Michael. "Major Groove Orientation of the (2S)-N6-(2-hydroxy-3-buten-1-yl)-2'-Deoxyadenosine DNA Adduct Induced by 1,2-Epoxy-3-butene." **Chemical Research in Toxicology**, 2014, 27, 10, 1675-1686

Presentations:

Poster Presentation, VINSE Nanoday, Fall 2015: Dual Mode Crystal-Bound and Surface-Bound Passivation of Quantum Dots
Poster Presentation, Gordon Research Conference-Colloidal Semiconductor Nanocrystals, Summer 2016: Dual Mode Crystal-Bound and Surface-Bound Passivation of Quantum Dots
Invited Speaker, Vanderbilt Chemistry Forum, Spring 2016: All Atoms Matter: Understanding Ligand Coordination on the Surfaces of Quantum Dots.
Poster Presentation, VINSE Nanoday, Fall 2015: Thiols in Nanocrystal Synthesis: Capping Ligands That Are More Than Skin Deep
Poster Presentation, Molecular Foundry User Meeting, Summer 2015: Development of Structural Models to Probe the Ligand Coordination on the surface of CdSe@ZnS
Oral Presentation, Spring 2015 ACS National Meeting, Spring 2015: Thiols in Nanocrystal Synthesis: Capping Ligands That Are More Than Skin Deep

Poster Presentation, VINSE Nanoday, Fall 2014: Thiols as Ligands and Sulfur Sources: Capping Ligands That Are More Than Skin Deep
Oral Presentation, 2014 SERMACS, Fall 2014: Thiols as Ligands and Sulfur Sources: Capping Ligands That Are More Than Skin Deep
Oral Presentation, VINSE Summer Lecture Series, Summer 2014: Thiols as Ligands and Sulfur Sources: Capping Ligands That Are More Than Skin Deep
Poster Presentation, Gordon Research Conference-Colloidal Semiconductor Nanocrystals, Summer 2014: Thiols as Ligands and Sulfur Sources: Capping Ligands That Are More Than Skin Deep
Poster Presentation, Oliver G. Ludwig Alumni Symposium Villanova University, Spring 2014: Thiols as Ligands and Sulfur Sources: Capping Ligands That Are More Than Skin Deep
Oral Presentation, 2013 SERMACS, Fall 2013: Crystal-Bound vs. Surface-Bound Thiols on Semiconductor Nanoparticle Surfaces: Achieving Water Solubility and Charge Transfer Properties
Poster Presentation, VINSE Nanoday, Fall 2013: Crystal-Bound vs. Surface-Bound Thiols on Semiconductor Nanoparticles (*Third Prize*)
Oral Presentation, Vanderbilt Chemistry Department Third Year Seminar, Fall 2013: Crystal-Bound vs. Surface-Bound Thiols on Semiconductor Nanoparticle Surfaces: Achieving Water Solubility and Charge Transfer Properties
Oral Presentation, VINSE Summer Lecture Series, Summer 2013: Novel Ligand to Exploit Crystal-Bound Ligands in Nanoparticle Synthesis
Poster Presentation, 2013 TN-SCORE Annual Meeting, Summer 2013: Rational Ligand Design for Nanoparticle Synthesis
Invited Speaker, Villanova University Chemistry Department Seminar, February 12, 2013: Progress Towards Hybrid Nanoparticles for Photocatalysis.
Poster Presentation, 2012 SERMACS, Fall 2012: New ligands for the synthesis of water soluble mixed copper sulfide nanoparticles
Poster Presentation, 2012 VINSE Nanoday, Fall 2012: New ligands for the synthesis of water soluble copper (I) sulfide nanoparticles
Poster Presentation, 2012 TN-SCORE Annual Meeting, Summer 2012: New ligands for the synthesis of water soluble copper (I) sulfide nanoparticles (*winner of the poster competition*)
Poster Presentation, Vanderbilt Institute for Chemical Biology Symposium, Fall 2011: Structural determination of N^6-(2-hydroxy-3-buten-1-yl)-2'-deoxyadenosine adduct induced by 3,4-epoxy-1-butene.
Invited Speaker, Villanova University Chemistry Department Seminar, February 15, 2011: Experiences in Industry
Poster Presentation, Villanova University Undergraduate Research Poster Session, Fall 2008: Synthesis and Analysis of Phenol Undecanoic Acid, Synthesis of 2,2'-Di-t-butylbiphenol, and Acetone Recovery From Isophorone Synthesis.
Poster Presentation, Villanova University Undergraduate Research Poster Session, Fall 2008: The Further Study of Octamethylbiphenylene Reduction With Lithium and Progress Toward the Synthesis of Dodecamethylbinaphthylene
Poster Presentation, Villanova University Undergraduate Research Poster Session, Fall 2008: A Computational Study of Dilithiobiphenylene and the Effect of Methyl Groups on the Ring-Opening to 2,2'-Dilithiobiphenyl.

Grants/Proposals:
Molecular Foundry User Proposal: XAS and First Principles studies of the Binding of Thiols to Quantum Dots-Spring 2015-Spring 2016, extended to Spring 2017
Department of Energy Office of Basic Science Graduate Student Research (SCGSR) Award: XAS and *ab initio* study on interfacial charge transfer in CdSe@ZnS nanocrystals with crystal-bound capping ligands-Winter 2014-Winter 2015
Grassroots outreach grant from the Materials Research Society: Materials Outreach for Rural Education (MORE)- $8633.00 Spring 2013-Spring 2014

Teaching Experience:
Vanderbilt University- Chemistry Teaching Assistant: organic chemistry lab Fall 2011, Spring 2012, Summer 2012, Summer 2016, Fall 2016 inorganic chemistry class, Fall 2012, demonstration for general chemistry class, Fall 2012, Fall 2016.

Villanova University-Chemistry Teaching Assistant: organic chemistry lab Fall 2009 and Fall 2010, general chemistry for nurses lab Spring 2010, Spring 2011
Villanova University-Chemistry tutor for learning support services August 2008 to May 2011

Leadership Experience:
Lab Safety Officer Macdonald Lab Vanderbilt University Spring 2012-Spring 2015
Co-Founder MORE: Materials Outreach for Rural Education, Fall 2013
Safety Auditor Vanderbilt Chemistry Department, Spring 2013, Fall, 2013, Spring 2014, Fall 2014
Chemistry Graduate Student Association committee member, Vanderbilt University 2013-2015
Moderator 2014 SERMACS oral section on Nanochemistry II

Undergraduate Students Mentored:
Samantha Monk-Summer 2012 REU student Austin Peay State University
Laura Mast-Spring 2013-Summer 2014 student Vanderbilt University

Professional Associations:
American Chemical Society
Materials Research Society